

POLITECNICO DI TORINO

DEPARTMENT OF APPLIED SCIENCE AND TECHNOLOGY

Master of Science in Physics of Complex Systems

Final Dissertation



**Politecnico
di Torino**

**Anomalous metallic phases induced via ionic gate-driven
intercalation of hydrogen and hydrogen-rich ions**

Supervisor

Prof. Renato Gonnelli

Co-Supervisor

Dr. Erik Piatti

Candidate

Jessica Montagna Bozzone

ACADEMIC YEAR 2021/2022

Abstract

The recent discovery of high-pressure, near-room-temperature superconductivity has been a milestone in fundamental research, but due to the high pressures involved (more than 200 GPa) and its instability in ambient conditions, any practical applications are currently unfeasible. Consequently, one of the most significant challenges is discovering a new class of superconductors presenting ambient-pressure superconductivity and displaying a transition at high temperature even if not necessarily at near-room-temperature. Therefore, to assess the potential of hydrogen-rich compounds to host new high-temperature conventional superconductors at ambient pressure conditions, it is necessary to identify an alternative and cheap technique to investigate a wide range of materials.

Ion intercalation is a method used to alter the properties of materials by modifying their crystal and electronic structures and can be performed via the ionic gating technique. During this process, carried out at room temperature and in ambient atmosphere, the material under study constitutes the active channel of an electrochemical transistor and is thus separated from a gate counter-electrode by an electrolyte. When a gate voltage is applied across the electrodes, intense electrostatic fields are generated through the dense accumulation of the solvated ions in the electrolyte on the surface of the channel, forming the so-called electric double layer. It is worth noting that, depending on the gating conditions and the nature of the material, non-volatile charge doping of macroscopic bulk specimens is attainable via gate-driven intercalation of either the hydrogen or organic ions which derive from the electrolyte. Exploiting the ultra-high electric field generated by the polarized electrolyte, it is possible to drive the accumulated ions in and out of the crystal lattice once sufficiently large gate voltages are applied. Furthermore, if the gating process is carried out at ambient conditions, the application of a positive gate voltage in excess of the hydrolysis potential splits the water absorbed by the electrolyte into OH^- and H^+ ions. Then, the free H^+ ions can be driven into the crystal lattice. The main advantage of this technique is that, in the case of stable intercalation, the H^+ or hydrogen-rich organic ion insertion is non-volatile, allowing several post-gating measurements.

The original aim of this thesis project was to search for superconducting phases in several compounds via protonation, i.e. direct hydrogen intercalation, by means the ionic-

gating method under optimized gating conditions. Indeed, H^+ or hydrogen-rich organic ion intercalation was used to induce electron-doping and/or structure modifications, which are two possible ways to trigger the emergence of superconductivity.

Few selected materials were analyzed, including Palladium (Pd), Palladium-Copper Alloy (Pd-Cu Alloy) and Molybdenum Disulphide (MoS_2). The experiments in turn allowed us to affect the ground state of these materials and induce structural (Pd), charge-density-wave (MoS_2), and/or insulator-to-metal (MoS_2) phase transitions. Shortly summarizing the main results of this experimental work, in the case of Pd, the emergence of an anomaly in the temperature dependence of resistivity was highlighted, which in literature is associated with a structural transition in the occupancy of hydrogen interstitial sites. Hydrogen concentration, found from the comparison with literature, was approximately equal to the atomic ratio $H/Pd=0.74$. In contrast, the resistivity of the as-received commercial $Pd_{0.6}Cu_{0.4}$ samples proved to be almost insensitive to the hydrogen levels obtained. X-ray diffraction (XRD) measurements showed that these exhibited the incorrect phase (face-centered cubic crystal structure) for the development of superconductivity upon hydrogen intercalation. Further improvements were realized via annealing processes to obtain the proper crystalline phases, again characterized through XRD. We realized a mixed phase with a higher concentration of face-centered cubic phase, which acts as a hydrogen reservoir for the body-centered cubic phase. The resistivity measurements performed after protonation on this sample presented an anomaly in the temperature dependence of the resistivity, which was confirmed by susceptibility measurements. Concerning the MoS_2 , temperature-dependent resistivity measurements showed the emergence of an anomalous metallic phase induced by the gate-driven intercalation of hydrogen-rich ions.

*There is always a wonderful destination
for all those who know how to wait.
Beautiful things have a slow pace.*

*To my Mum and Dad
To my little Sister*

Acknowledgements

I would like to thank my supervisors Prof. Renato Gonnelli and Dr. Erik Piatti for their professional support and guidance. A special thank goes also to Prof. Dario Daghero.

I would also like to express my sincere gratitude to everyone who gave me something good along this journey.

Contents

List of Figures	8
List of Tables	15
Nomenclature	17
1 Introduction	1
1.1 Motivations	1
1.2 State of the art	2
1.3 Thesis Structure	5
2 Ionic Gating and Ion Intercalation Techniques	7
2.1 Ionic Gating Technique	7
2.2 Ionic-Gating-induced Ion Intercalation	11
2.3 Ionic-Gating-Induced Protonation	13
3 Gate-Driven Protonation and Intercalation: The Experimental Approach	19
3.1 Fabrication of the experimental setup	19
3.2 Materials and methods	22
3.2.1 Characterization techniques: a general introduction	22
3.2.1.1 Electric-Field-Driven Ion Intercalation	23
3.2.1.2 Electrolyte	24
3.2.1.3 Resistivity Measurements	25
3.2.2 Data Acquisition and Analysis tools	27
4 Palladium and Palladium-Copper Alloy	29
4.1 General description of Palladium	29
4.1.1 Results and discussion	32
4.1.1.1 Electric-Field-Driven Ion Intercalation	32
4.1.1.2 Resistivity measurements	34
4.2 General description of Palladium-Copper Alloy	47
4.2.1 Results and discussion	52
4.2.1.1 Electric-Field-Driven Ion Intercalation	52
4.2.1.2 Resistivity measurements	54

4.2.1.3	X-ray diffraction	58
4.2.1.4	Results and discussion	60
4.2.1.5	Magnetic susceptibility	69
4.2.1.6	Results and discussion	74
5	Molybdenum Disulphide	77
5.1	General description of Transition metal dichalcogenides	77
5.2	General description of Molybdenum Disulphide	81
5.3	Results and discussion	84
5.3.1	Electric-Field-Driven Ion Intercalation	84
5.3.2	Temperature-dependent resistivity measurements	88
6	Other Techniques	97
6.1	Vibrational spectroscopy	97
6.1.1	Raman spectroscopy	97
6.1.2	Infrared Spectroscopy	99
6.1.3	Material and methods	100
6.2	Scanning microscopy techniques	102
6.2.1	Atomic Force Microscopy	102
6.2.2	Nano-Infrared Microscopy	104
6.2.2.1	Materials and methods	104
6.2.3	Kelvin-Probe Force Microscopy	105
6.2.3.1	Materials and methods	106
6.3	Results and discussion	108
6.3.1	Raman spectroscopy	108
6.3.2	Fourier-transform infrared (FT-IR) spectroscopy	110
6.3.3	Nano-Infrared Microscopy	113
6.3.4	Kelvin-Probe Force Microscopy	115
7	Conclusions and Future Perspectives	121
	Bibliography	124

List of Figures

1.2.1	Periodic table of the elemental hydrides [9]	2
1.2.2	Maximum superconducting T_c achieved in different hydrogen-based or hydrogen-doped compounds [1].	3
2.1.1	Sketch of MIS stack (panel a) and conventional FET (panel b). In (b) positive (+) and negative (-) charges are accumulated on a gate electrode and a semiconductor channel, respectively, by applying a gate voltage V_G [22]. . .	8
2.1.2	Interface between the ionic liquid and semiconductor of a typical EDL-FET. From [28].	9
2.1.3	A comparison of gating efficiency in terms of maximum reached carrier density among IL gating, polymer electrolyte gating, and a solid dielectric [22].	11
2.2.1	Schematic ion intercalation of Li^+ and Na^+ in a layered structure of MoS_2 . From [37].	12
2.3.1	Schematic diagrams of the transport and storage of (a) oxygen and (b) hydrogen ions with negative and positive external gating voltages in an ionic liquid gating device, respectively [35].	13
2.3.2	Reversible phase transformation of $\text{SrCoO}_{2.5}$ through the electric-field selectively controlled dual-ion (O^{2-} and H^+) switch. The red and blue arrows represent negative and positive voltages, respectively [35].	14
2.3.3	An illustration of the protonation setup adapted from [41]. Platinum electrodes are placed in a container filled with the ionic liquid. The gating voltage is set to be about 3.0 V. The ionic liquid is heated up to 350K by a hot plate. . .	15
2.3.4	The resistance of $\text{H}_y\text{-FeSe}_{0.93}\text{S}_{0.07}$ vs temperature. The arrow indicates the superconducting transition around 43.5 K. From [41].	16
2.3.5	(a) XRD patterns of FeSe single crystal (in black) and intercalated FeSe (in red); (b) Schematic crystal structure of $(\text{EMIM})_x\text{FeSe}$. Adapted from [47]. .	17

3.1.1 (a) Illustration of the experimental setup for ionic-gating-induced protonation, showing the Pt wires used for applying the gate voltage (V_G) and measuring the sample's four-wire resistivity as well as the reference voltage (V_{ref}). (b) The Helmholtz layer of cations and the counter-charge in the gated sample make up the EDL, which is shown schematically as a positive V_G . From [1]	20
3.1.2 Experimental setup building process: (1) realization of the sample holder; (2) etching process; (3) connection to a larger extension boarder; (4) final configuration.	21
3.2.1 Sketch of the circuit of the current-reversal method. Adapted from [50] . . .	23
3.2.2 (a) common electric-field-driven ion intercalation setup at room-temperature and (b) at higher temperature ($= 57^\circ\text{C}$). Panel (a) also shows the measuring instruments used during this part of the experiments.	24
3.2.3 Structural formulas 1-ethyl-3-methylimidazolium tetrafluoroborate ionic liquid.	25
3.2.4 Structural formulas of glycerol (left) and chloride choline (right). From [56].	26
3.2.5 (a) ST-403 pulse-tube cryocooler with a closeup on the cryochamber; (b) cryocooler sample holder with a magnification on the teflon cell holding the ionic liquid, the sample electrically contacted with the Ag paste (green rectangle in (c)) and the gate electrode (red rectangle (c)).	27
4.1.1 The face centered cubic (FCC) crystal structure with its two available interstitial sites: octahedral (b) and tetrahedral (c). Adapted from [62].	29
4.1.2 Pd-H system phase diagram. Adapted from [70].	30
4.1.3 Gate voltage (upper panel - solid blue line) and resistivity (lower panel - solid red line) measured <i>in situ</i> as a function of time during a gating process. . .	33
4.1.4 Gate voltage (upper panel - solid blue line) and resistivity (lower panel - solid red line) measured <i>in situ</i> as a function of time during a gating process. . .	34
4.1.5 Schematic variation of the electrical resistivity of a normal metal (solid blue line) and a superconductor (solid red line) with absolute temperature. At high temperatures, the electrical resistivity of a normal metal is the sum of a residual component ρ_r and a thermal component ρ_T . Adapted from [89].	35
4.1.6 <i>Ex situ</i> resistivity (ρ) measurements in function of the temperature (T) for representative samples of Pd after the electric-field-driven ion intercalation using the GT90 IL, in different gating conditions.	36
4.1.7 <i>In situ</i> resistivity (ρ) measurements in function of the temperature (T) for representative samples of Pd after the electric-field-driven ion intercalation using the GT90 eutectic mixture, in different gating conditions.	38

4.1.8	<i>Ex situ</i> resistivity measurements normalized at the value of the pure Pd at 4.2 K ($\rho/\rho(4.2K)$) in function of the temperature (T) for representative samples of Pd after the electric-field-driven ion intercalation using the GT90 eutectic mixture, in different gating conditions. The yellow background highlights the integration area under investigation.	39
4.1.9	<i>In situ</i> resistivity measurements normalized at the value of the pure Pd at 4.2 K ($\rho/\rho(4.2K)$) in function of the temperature (T) for representative samples of Pd after the electric-field-driven ion intercalation using the GT90 eutectic mixture, in different gating conditions. The yellow background highlights the integration area under investigation.	40
4.1.10	(a) and (b) represent the original graphs of the resistivity measurements normalized at the value of the pure Pd at 4.2 K from the literature [72]; (c) is our digital reconstruction of (a) and (b).	42
4.1.11	Solid red line indicates the first derivative of the resistivity normalized at 79 K (solid black line) in temperature for the different hydrogen concentration x extracted from [72]. The blue point indicates the onset temperature of the anomaly. 43	
4.1.12	Onset temperature of the anomaly in function of the $x = \text{H/Pd}$ concentration, extrapolated from [72].	44
4.1.13	Solid red line indicates the first derivative of the resistivity normalized at 79 K (solid black line) in temperature for the different gating conditions. . . .	45
4.1.14	Onset temperature of the anomaly in function of the $x = \text{H/Pd}$ concentration in our <i>in situ</i> samples.	46
4.2.1	(a) Transition Temperature (T_c) versus implanted H-dose of a $\text{H/Pd}_{0.55}\text{Cu}_{0.45} \sim 0.04$ alloy. (b) Maximum T_c -value vs Cu concentration in the the ternary hydride PdCuH_x . Adapted from [12]	49
4.2.2	Unit cell of the PdCu in the B2-phase. Gray (brown) spheres represent Pd (Cu) atoms. In the unit cell, the high symmetry intercalation sites of H are indicated with blue points. From [91]	49
4.2.3	Hydrogen permeability as a function of palladium wt% at 623 K and phase diagram of Pd-Cu alloys. From [92]	50
4.2.4	Elementary bcc lattice cell showing octahedral (red spheres) and tetrahedral (blue spheres) interstitial sites.	52
4.2.5	Gate voltage (upper panel - solid blue line) and resistivity (lower panel - solid red line) measured <i>in situ</i> as a function of time during a gating process. In this case the electric-field-driven ion intercalation was performed using the EMIM- BF_4 ionic liquid.	53
4.2.6	Gate voltage (upper panel - solid blue line) and resistivity (lower panel - solid red line) measured <i>in situ</i> as a function of time during a gating process. In this case the electric-field-driven ion intercalation was performed using the GT90 eutectic mixture.	54

4.2.7	<i>Ex situ</i> resistivity measurements normalized at the value of the respective resistivity at 300 K ($\rho/\rho(300K)$) in function of the temperature (T) for representative samples of the Pd _{0.6} Cu _{0.4} alloy before and after the electric-field-driven ion intercalation using the EMIM-BF ₄ IL, in different gating conditions. The inset reports the temperature values of $\rho(300K)$ for each analyzed sample. .	56
4.2.8	<i>Ex situ</i> resistivity measurements normalized at the value of the respective resistivity at 300 K ($\rho/\rho(300K)$) in function of the temperature (T) for representative samples of Pd _{0.6} Cu _{0.4} alloy after the electric-field-driven ion intercalation using the GT90 eutectic mixture, in different gating conditions. The inset reports the temperature values of $\rho(300K)$ for each analyzed sample. .	57
4.2.9	Reflection of a X-rays beam on the planes (hkl) of a crystal.	59
4.2.1	Schematic setup of the powder X-ray diffractometer. From [99].	60
4.2.1	Representative XRD patterns of the Pd-Cu in the pure state. Adapted from [102].	61
4.2.1	X-ray diffraction patterns of Pd _{0.6} Cu _{0.4} alloys at different annealing conditions. 62	
4.2.1	X-ray diffraction patterns as a function of the annealing time for Pd _{0.64} Cu _{0.36} alloys. Adapted from [103].	63
4.2.1	Resistivity measurements in function of the temperature for representative samples of Pd _{0.6} Cu _{0.4} alloy before and after the annealing processes, in different temperature and time conditions. The squared labels indicate the phases obtained via the annealing treatments.	64
4.2.1	Resistivity measurements in function of the temperature for the Pd _{0.6} Cu _{0.4} alloy after the annealing processes at 450°C for 36 hours (solid pink line) and for the same sample after the <i>in situ</i> electric-field-driven ion intercalation at +3.5 V for 1 hour (solid blue line).	65
4.2.1	XRD patterns of (a) B2 and (b) FCC/B2 mixed phased Pd _{0.6} Cu _{0.4} alloys in air. From [105].	66
4.2.1	Resistivity measurements in function of the temperature for the Pd _{0.6} Cu _{0.4} alloy after the annealing processes at 450°C for 8 hours and for the same sample after the electric-field-driven ion intercalation with GT90 eutectic mixture at +3.0 V.	67
4.2.1	Resistivity measurements in function of the temperature for the Pd _{0.6} Cu _{0.4} alloy normalized at the value of the resistivity at 300K of each sample ($\rho/\rho(300K)$) after the annealing processes at 450°C for 8 hours and for the same sample after the electric-field-driven ion intercalation with GT90 eutectic mixture at +3.0 V.	68
4.2.1	Real (solid blue line) and Imaginary (solid green line) parts of the AC susceptibility versus frequency. Adapted from [108].	70
4.2.2	Schematic drawing of the AC susceptometer. Adapted from [23].	72
4.2.2	Lock-in amplifier block diagram. From [110].	72

4.2.2	Real (blue dots) and imaginary (red dots) components of the susceptibility of PdCu alloy protonated with GT90 IL annealed in the mixed (FCC+B2) crystalline phase regime.	75
5.1.1	Representation of the repetition of the two main TMD coordinations. The small black and large red circles respectively represent the transition metal and chalcogen atoms. Adapted from [40].	78
5.1.2	Metal coordinations and stacking sequences of TMD structural unit cells. Adapted from [120].	79
5.1.3	Transition metals and chalcogen elements forming TMDs are highlighted in the periodic table. Adapted from [122].	79
5.1.4	Schematic representations of electronic band structures near the Fermi level for a solid with a direct bandgap (a) and a solid with an indirect bandgap (b). ϵ_F is the Fermi level having the Fermi wave vector k_F . From [123].	80
5.2.1	Calculated band structures of (a) bulk MoS ₂ , (b) quadrilayer MoS ₂ , (c) bilayer MoS ₂ , and (d) monolayer MoS ₂ . The solid arrows indicate the lowest-energy transitions. From [126].	82
5.2.2	Electronic band structure of gated 4-layer-MoS ₂ . The gray line represents the Fermi energy ϵ_F . The inset shows the first BZ of 2H-MoS ₂ where the Γ , K=K', and M high symmetry points are highlighted. Adapted from [128].	83
5.3.1	Gate voltage (upper panel - solid blue line) and resistivity (lower panel - solid red line) measured <i>in situ</i> as a function of time during a gating process.	85
5.3.2	Gate voltage (upper panel - solid blue line) and resistivity (lower panel - solid red line) measured <i>in situ</i> as a function of time during a gating process. Region 5 represents the trend during a release time of 4 minutes.	86
5.3.3	Gate voltage (upper panel - solid blue line) and resistivity (lower panel - solid red line) measured <i>in situ</i> as a function of time during a gating process. Region 5 represents the trend during a release time of 50 minutes.	87
5.3.4	Resistivity at 300 K measured <i>ex situ</i> as a function of the release time.	88
5.3.5	Temperature dependence of the resistivity in the semiconductor. Adapted from [135].	89
5.3.6	Temperature dependence of the resistivity ρ divided by its value at 300 K, before and after electric-field-driven ion intercalation, in semi-log scale.	91
5.3.7	Temperature dependence of the resistivity ρ divided by its value at 300 K, before and after electric-field-driven ion intercalation, in linear scale.	92
5.3.8	T dependence of $d\rho/dT$, before and after ion-intercalation, obtained by numerical derivation of the curves in Figure 5.3.7. Arrows highlight the values of T where $d\rho/dT$ shows a dip (T*). The curves are vertically offset for clarity.	93
5.3.9	T* (blue squares, left scale) and inverse residual resistivity ratio 1/RRR (red diamonds, right scale) as a function of the release time.	94

6.1.1 Energy-level diagram showing the states involved in Raman spectra. Adapted from [160].	98
6.1.2 Schematic of a Raman. From [162].	99
6.1.3 Schematic diagram showing the working principle of an dispersive IR spectroscoper. From [164].	99
6.1.4 Schematic block diagram showing the working principle of an FT-IR spectroscoper. From [165].	100
6.1.5 Micro-Raman spectrometer was used to collect Raman spectra	101
6.1.6 Nicolet 5700 spectrometer used to measure FT-IR spectra	102
6.2.1 Plot of forces as function of distance. From [170].	103
6.2.2 (a) schematic diagram of classical AFM-IR. A pulse tunable laser source illuminates a sample at an angle above the tip of AFM cantilever; (b) AFM-IR working principle. Adapted from [172, 174]	104
6.2.3 Anasys nanoIR3-s atomic force microscope.	105
6.2.4 Schematic diagram of AM-KPFM. From [182].	107
6.2.5 (a) Innova AFM; (b) a magnification of the metallic sample holder, containing samples attached using a specific electrically-conducting adhesive tape; (c) standard platinum-iridium-covered silicon tip approaching to the sample.	107
6.3.1 Raman spectra of MoS ₂ (solid blue line) and intercalated-MoS ₂ (solid red line) crystals.	108
6.3.2 Lorentzian fit of the A _{1g} mode for both pristine and intercalated MoS ₂ crystal.	109
6.3.3 FT-IR absorption spectra acquired in ATR mode between 3500 and 900 cm ⁻¹ . The peaks of the EMIM-BF ₄ spectrum are labelled.	110
6.3.4 Infrared nanospectroscopy of intercalated MoS ₂ . (a) AFM topography map. (b) Phase image of the same area of panel (a). Adapted from [118].	113
6.3.5 Infrared nanospectroscopy of intercalated MoS ₂ . Nano-IR absorption spectra acquired in correspondence of a droplet (solid blue line, point D) and of the MoS ₂ exposed surface (solid red line, point S). Adapted from [118].	114
6.3.6 IR absorption map of the same area acquired in correspondence of the EMIM-breathing mode at ~1572 cm ⁻¹ . Adapted from [118].	115
6.3.7 Kelvin-probe force microscopy of pristine MoS ₂ sample. (a) AFM topography map and (b) Surface potential map of pristine MoS ₂ . Adapted from [118].	115
6.3.8 Kelvin-probe force microscopy of EMIM-MoS ₂ sample. (a) AFM topography map and (b) Surface potential map of intercalated MoS ₂ . Adapted from [118].	116
6.3.9 Kelvin-probe force microscopy of pristine and EMIM-MoS ₂ sample. Surface potential histograms highlighting the shift (leftward solid black arrow) in the Fermi energy induced by the intercalation of EMIM ions. Adapted from [118].	117
6.3.10(a) Raman spectra at room and low temperatures; (b) enlargement of the Raman shift between 340 and 430 cm ⁻¹ . Adapted from [198].	118

6.3.1	Red circles indicate the crash points of the tip on the sample surface. Adapted from [198].	119
6.3.1	(a) Current-z distance curve (b) Topography map obtained with a tip gently touching the surface. Adapted from [198].	119

List of Tables

2.1	T_c of the materials before and after protonation [41].	16
3.1	Overview of the characterization techniques applied on each material.	22
4.1	Data acquired through the integration of the resistivity curves of the <i>ex situ</i> measurements of Figure 4.1.8 between 25 and 79 K.	41
4.2	Data acquired through the integration of the resistivity curves of the <i>in situ</i> measurements of Figure 4.1.9 between 25 and 79 K.	41
4.3	Data acquired through the integration of the resistivity curves of the graph extracted from the literature [72] between 25 and 79 K.	42
4.4	Effect of substitutional alloying of Pd on superconducting transition temperatures. Adapted from [9].	47
6.1	Overview of AFM modes operation. Adapted from [170, 171].	103

Nomenclature

A-SC	Ambient-temperature Superconductivity
AFM	Atomic Force Microscope
AM	Amplitude Modulated
ATR	Attenuate Total Reflection
BCC	Body-Centered Cubic
BCS	Bardeen–Cooper–Schrieffer
CB	Conduction Band
CDW	Charge Density Wave
CPD	Contact Potential Difference
D	Drain
EDL	Electric Double Layer
EDL-FET	Electric-Double-Layer Field-Effect Transistor
FCC	Face-Centered Cubic
FE	Field-Effect Transistor
FE	Field-Effect
FT-IR	Fourier Transform - IR
G	Gate
IL	Ionic Liquid
ILG	Ionic Liquid Gating

IR Infrared
KPFM Kelvin Probe Force Microscope
MIS Metal-Insulator-Semiconductor
NRT-SC Near-Room-Temperature Superconductivity
OC Open Circuit
SC Superconductivity
SPM Scanning Probe Microscope
STM Scanning Tunnelling Microscope
 T_c Critical Temperature
TMDs Transition Metal Dichalcogenides
TMDs Transition-Metal Dichalcogenides
VB Valence Band
XRD X-Ray Diffraction

Chapter 1

Introduction

1.1 Motivations

Designing materials with advanced features is one of the main goals of modern solid-state physics and chemistry. The recent discovery of high-pressure, near-room-temperature superconductivity (NRT-SC) has been a milestone in fundamental research, but due to the high pressures involved (more than 200 GPa) and its instability in ambient conditions, any practical applications are currently unfeasible.

Consequently, one of the most significant challenges is discovering a new class of technologically-relevant materials presenting ambient-pressure superconductivity and displaying a transition at high temperature even if not necessarily at near-room-temperature. Obtaining superconductivity at ambient conditions opens the road for a wide range of applications. That is due to the possibility of interacting with a single, coherent, macroscopic quantum mechanical state without the limitations related to cryogenics and pressurization. Therefore, to assess the potential of hydrogen-rich compounds to host new high-temperature conventional superconductors at ambient pressure conditions, it is necessary to identify an alternative and cheap technique to investigate a wide range of materials, overcoming the remaining obstacle to ambient temperature superconductivity (A-SC), namely the reduction of operating pressure [1].

Hence, this thesis work primarily focuses on a new experimental methodology for controlled synthesis and characterization of these materials. In particular, we performed protonation, i.e. direct hydrogen intercalation, through the ionic-gating method in optimized conditions to induce and search for superconducting phases in a few selected materials, including Palladium (Pd), Palladium-Copper Alloy (Pd-Cu Alloy) and Molybdenum Disulphide (MoS_2). The intercalation of H^+ or hydrogen-rich organic ions enables electron doping and/or structure modifications, reported in the literature as two possible ways to induce superconductivity.

1.2 State of the art

Elements with low atomic numbers should present superconductivity at high temperatures, based partly on conventional BCS (Bardeen–Cooper–Schrieffer) theory [2]. Nearly 90 years ago, Wigner and Huntington predicted that, at very high pressure, solid molecular hydrogen would dissociate into a metallic atomic phase, i.e. metallic hydrogen [3]. In 1997, Richardson and Ashcroft have theoretically predicted that hydrogen, once compressed into its dense metallic phase, would become superconducting with a transition temperature exceeding room temperature [4]. However, since the direct metallization of hydrogen requires pressures above 400 GPa, beyond the control of present experimental techniques, this transition is not easy to confirm. Inspired by the above-mentioned experimental results, first Lin and Dunn [5], then more recently, Shimizu and coworkers [6] conducted analyses on the lightest metal on the periodic table, i.e. lithium. This latter becomes superconductive at pressures higher than 30 GPa, lower than those observed for metallic hydrogen. Furthermore, the pressure-dependent transition temperature is about 20 K at 48 GPa. Superconductivity has also been investigated for the combination of light elements as exhaustively confirmed, e.g. in Magnesium diboride (MgB_2), which exhibits superconductivity at relatively high temperatures (around 40 K) [7]. All this confirms that elements with a low atomic number exhibit a high transition temperature [6]. Moreover, it suggests that metallic hydrogen is a superconductor with high transition temperatures both in monatomic and more complex structures where, in band-overlap states, protons retain their pairing [8].

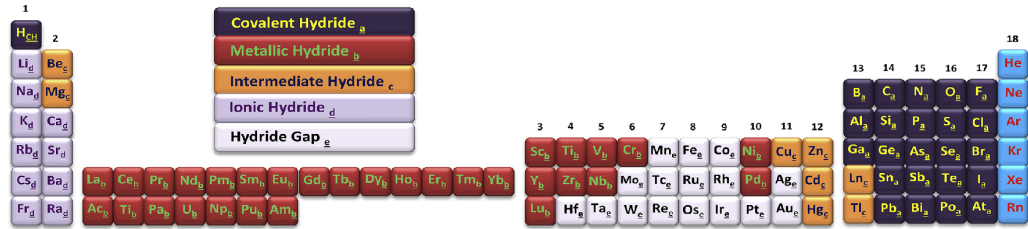


Figure 1.2.1: Periodic table of the elemental hydrides [9]

As shown in Figure 1.2.1, hydrogen can form compounds with most of the elements in the periodic table, giving rise to a wide range of binary hydrides. That gives us a rich spectrum of chemical and physical properties to choose from and modify [9].

In 1970, the first proof-of-concept was found in Thorium (Th). Indeed, through high-temperature exposure to hydrogen gas and the resulting formation of the compound Th_4H_{15} , the $T_c \simeq 1.4$ K of elemental Th had been boosted to 8.2 K [10]. Two years later (1972), the induction of superconductivity in Pd was demonstrated. This material showed critical temperatures up to $T_c = 9.4$ K via low-temperature hydrogen (H) implantation. A higher transition temperature, T_c

= 11 K, was reached by the low-temperature deuterium (D) implantation [11]. As done in Pd, low-temperature H implantation was used in $\text{Pd}_{1-x}\text{M}_x$ alloys (with $\text{M} = \text{Cu}, \text{Ag}, \text{and Au}$, respectively), providing higher critical temperatures $T_c = 16.6, 15.6, 13.6$ K. The same technique was applied to other alloys of Nb, Pd, Pd-Mo and Rh, often obtaining a remarkable increase in T_c . Some of these results are summarized in Figure 1.2.2 [12]. Regardless, after 1986 the interest of the scientific community became entirely absorbed by high- T_c cuprates. Thus, the research on metal hydrides was temporarily abandoned.

It is only in the mid 2010's that a new interest for metal hydrides arose. Originally, hydrides with a moderate or relatively low hydrogen content have been considered potential superconductors. Hence, the idea of investigating hydrides with a high hydrogen content was born [8]. One of the most important results has been obtained in recent years, when, thanks to a synergistic work between theory and experiments, several superhydrides were found, such as SH_3 at megabar pressure and LaH_{10} , that have superconductivity at high temperatures, respectively at 203 K and 260 K [1, 13, 14].

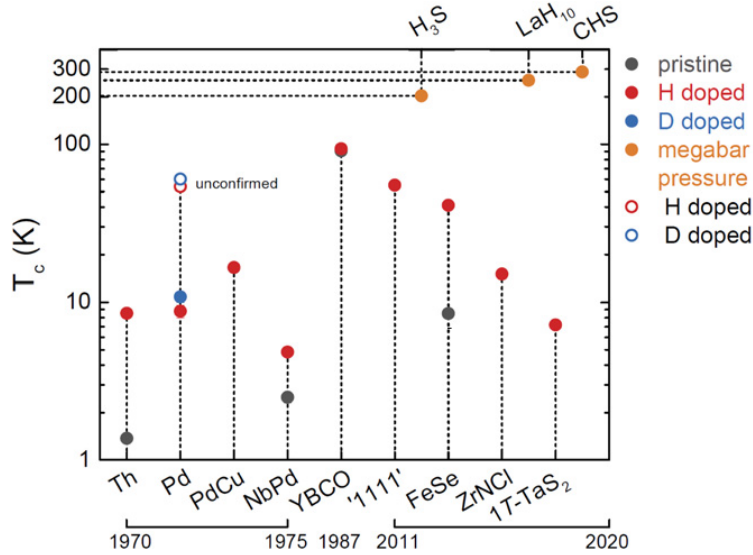


Figure 1.2.2: Maximum superconducting T_c achieved in different hydrogen-based or hydrogen-doped compounds [1].

Superhydrides are compounds that contain an abnormally large amount of hydrogen, forming highly-symmetrical hydrogenic sublattices kept connected by covalent metal bonds, which are necessary to increase T_c . They are generally known to be stable under high pressure, so they may resemble the metallic hydrogen but can be made under lower pressures. Therefore, they may be superconductors. In particular, they are considered to be phonon-mediated (conventional) superconductors broadly described by the Migdal-Eliashberg theory [15]. There

are anomalies, such as the role of anharmonicity, non-adiabatic corrections to the electron-phonon interaction, and the Coulomb interaction, that need to be fixed for a quantitative theory of superconductivity [15, 16]. So, superhydrides are important prototypes for studying metallic hydrogen and understanding the critical factors behind high- T_c superconductivity [17]. However, as mentioned earlier, although the discovery of superhydrides is of fundamental importance, it is impractical due to the very high pressures involved. The hypothesis is that the same factors that induce high- T_c superconductivity in superhydrides could also be found in other systems that require lower stabilisation pressures, such as hydrogen-rich compounds obtained through hydrogen absorption in different classes of material, including simple metals and alloys, layered iron-based compounds, 2D transition metal dichalcogenides (TMDs), and graphite intercalated compounds (GICs). So far, this field has been little explored, but combining techniques such as computational methods for *ab-initio* material design and data science could lead to the discovery of new materials and potential new applications [1].

The study of hydrogen absorption in crystalline structures and the consequent creation of new chemical bonds are interesting for several reasons. First, it generally induces an expansion of the lattice, which can be regarded as a symmetric effect of compression by hydrostatic pressure. This enables an alternative way of tuning the superconducting pairing, which depends closely on the alteration of the crystal lattice, electronic structure and phonon spectrum. Accordingly, hydrogen loading should improve critical superconducting properties such as critical temperature (T_c), critical current density (j_c) and critical magnetic field (H_c) of known superconductors [9].

There are various techniques for loading hydrogen into materials and measuring its absorption. One of the typical problems is that the hydrogenated state can be unstable as soon as the thermodynamic source used to perform the hydrogenation is removed. One can therefore understand how important it is to be able to perform resistivity and magnetic susceptibility measurements *in situ*. The main experimental techniques used for hydrogen loading are essentially:

- ***absorption from the gas phase***, including the Sieverts and Gravimetric techniques. The former can be applied accurately up to gaseous pressures of kbar over a wide temperature range and is compatible with *in situ* transport measurements; the latter, on the other hand, is generally more accurate but is much less capable of being applied for high hydrogen pressures;
- ***electrochemical loading of H*** at room temperature (but also at different ones) allows higher doping levels to be achieved than absorption from the gas phase. However, this technique has poor stoichiometric control;
- ***ion implantation*** achieves out-of-equilibrium doping profiles but requires stabilisation processes and damages the sample.

Furthermore, it should be specified that not only H^+ but also ions of organic nature can be intercalated within the materials, as detected in 2018 by Shi et al..

As described in [18], they synthesized an organic-ion-[cetyltrimethyl ammonium (CTA⁺)]-intercalated FeSe-based superconductor ((CTA)_{0.3}FeSe), having a high T_c (45 K) and high crystallinity.

The massive revival of superconductors based on the intake of hydrogen or hydrogen-rich organic ions leads us to ask whether there are alternative routes to low-cost, fast and environmentally stable hydrogen-based superconductors. A new protonation technique, already successfully used in some layered materials, can address this challenge based on an ionic-gating-like setup [1][9].

1.3 Thesis Structure

In particular, this work is organized in the following chapters:

Chapter 1: This chapter is intended to briefly introduce the main motivations that led us to develop this experimental project.

Chapter 2: This chapter provides an overview of ionic gating and ion intercalation and protonation techniques. Here, we aim to highlight the main features of these techniques through a careful study of the state of the art.

Chapter 3: Here, we describe the experimental set-up that was implemented to conduct the main experimental part of the project. Then, we outline how we performed the gate-driven ion intercalation and the post-gating resistivity measurements as function of the temperature. Finally, we summarize the computational tools we use to analyse the amount of data acquired.

Chapter 4: This chapter is devoted to the analysis of two interesting materials: Pd and the Pd-Cu Alloy. Starting from their chemical description, we proceed discussing the electrical characterization of the materials either during the protonation or post-gating. Then, a comprehensive data analysis was performed to extract parameters useful to analyse the electrical behaviour of the samples under investigation after the protonation and to quantify (for Pd) the amount of hydrogen which enters into the materials. We also analysed the crystalline structure of PdCu-alloy and its susceptibility. To conclude, we present the most important results obtained and compare them with the literature.

Chapter 5 and 6: This chapter addresses the study of MoS₂. We start from the usual electrical characterization and then we focus on further analysis, such as vibrational spectroscopies (Raman, Fourier-Transform Infrared), Nano-Infrared Microscopy and morphological characterization using Atomic Force Microscopy and Kelvin-Probe Force Microscopy. To conclude we provide the most important results, showing that the organic ion-intercalated molybdenum disulphide crystals exhibit an anomalous metallic phase.

Chapter 7: This chapter presents a summary of the main conclusions and considerations of the results obtained. These studies could pave the way for further research, which would take into account the use of other conditions to induce the superconductive phase or other materials to expand the class of protonated materials.

Chapter 2

Ionic Gating and Ion Intercalation Techniques

Ion intercalation is a method used to alter the properties of materials by modifying their crystal and electronic structures and can be performed via the ionic gating technique. This chapter provides an overview of ionic gating and ion intercalation technique of hydrogen (in this case, the technique is known as protonation) or hydrogen-rich organic ions. We aim to highlight the main features of these techniques through a careful study of the state of the art.

2.1 Ionic Gating Technique

Ionic gating is a well-known technique for studying and controlling electrical charge transport and the electronic ground state in various materials. This is because of its capability to induce significant modulations of the surface charge density through the electric-double-layer field-effect transistor (EDL-FET) architecture [19]. In the following, the basic operating principles of the EDL-FET architecture are introduced.

The electric field effect (FE), one of the most important physical mechanisms for the semiconductor devices, permits the modulation of the surface conduction properties of a wide variety of different materials by means of a transverse electric field applied through a gate electrode on the surface [20, 21]. Applying a bias to the metal-insulator-semiconductor (MIS) structure leads to a change in the concentration of the carriers present in the semiconductor layer, which in turn implies a change in the semiconductor's electrical conductivity. The latter can be expressed as $\sigma = qn\mu$, where q , n and μ represent the elementary charge, the charge density and the mobility, respectively. The resistivity of the semiconductor increases (or, equivalently, the conductivity decreases) when the free-carrier concentration is significantly reduced because of the semiconductor depletion obtained by applying a proper gate bias. Instead, when the semiconductor is biased into inversion (accumulation), thanks to the application of a proper gate voltage, a strongly conducting channel of the opposite (same) carrier type to that of the

bulk semiconductor material is formed at the interface between the semiconductor and the insulator[20]. Thus, the FE can be used as a gating mechanism. Varying the applied gate bias, one alters the current-carrying properties of the layer, making the underlying semiconductor either highly conducting or resistive. In the first case, a current can flow through the layer, and then a conducting channel is opened at the semiconductor-insulator interface. Whereas only a tiny, typically negligible, reverse leakage current can flow in the second case. Consequently, no conducting channel exists at the semiconductor-insulator interface. Therefore, through the FE, a conducting channel at the surface of the semiconductor can be opened and closed. Hence, the MIS structure can be used as a gate to control the current flow between two reservoirs of charge, which are connected to an external circuit by ohmic contacts. This latter represents the working principle at the base of a field-effect transistor (FET), sketched in Figure 2.1.1 [20].

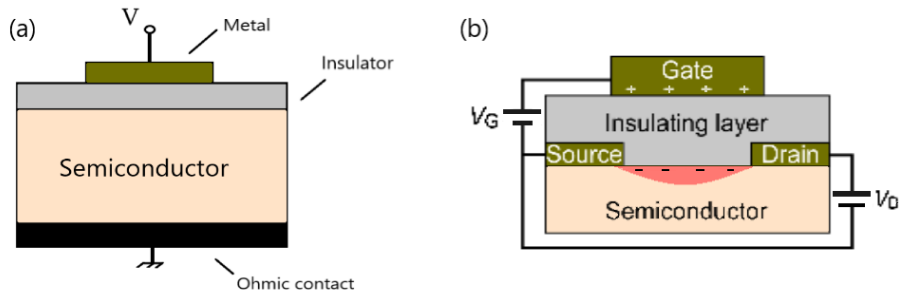


Figure 2.1.1: Sketch of MIS stack (panel a) and conventional FET (panel b). In (b) positive (+) and negative (-) charges are accumulated on a gate electrode and a semiconductor channel, respectively, by applying a gate voltage V_G [22].

When the insulating layer is an oxide, we obtain the so-called MOSFET configuration.

In addition to semiconductor electronic device applications such as the previously mentioned FETs, the FE technique is used for a broad variety of purposes. In conventional FE gating techniques using a solid gate dielectric, e.g. SiO_2 , the maximum density of the induced surface charge is relatively small, i.e. of the order of $\sim 10^{13} \text{ cm}^{-2}$. This latter is far from the expected one to induce electronic phase changes in most materials. In order to overcome these limits, a different way of doping the material, based on an electrochemical concept to control the material properties with an electric field, was necessary. In particular, the idea was to substitute the gate oxide with an electrolyte [23].

An electrochemical transistor exploits the MISFET structure by replacing the solid insulating dielectric with an electrolyte. By applying a gate voltage between the gate electrode and the active channel of the transistor, solvated ions in the elec-

trolyte move towards both electrodes according to their charge polarity. Intense electrostatic fields are generated through the dense accumulation of the solvated ions in the electrolyte on the surface of the channel, forming the EDL, which was originally conceptualized by von Helmholtz in 1853.

When two conducting phases (in our case, the material and the electrolyte or the gate and the electrolyte) combine in an interface, we have the formation of an EDL. Typically, one of the phases acquires an excess of surface charge, positive or negative, which is balanced by a countercharged phase, of same magnitude and opposite sign. Ions in the first layer are adsorbed onto the surface thanks to chemical interactions while ions into the second layer are attracted to the surface through coulombian forces[24]. In the case of highly concentrated electrolytes, such as ionic liquids, the thickness of EDL is of the order of a nanometer as reported in Figure 2.1.2. It is worth noting that, since the voltage drop occurs mostly within the EDL, the electric field produced is extremely large, > 10 MV/cm [25, 22]. Owing to this extremely high electric field, EDL gating, depending on the density of states of the sample and the electrochemical stability window of the electrolyte itself, has the unique capability to push the charge density accumulation up to 10^{14} - 10^{15} cm $^{-2}$, well beyond the limitations of any solid gate dielectric [26]. This device is known as an EDL-FET [25, 27], as sketched in Figure 2.1.2.

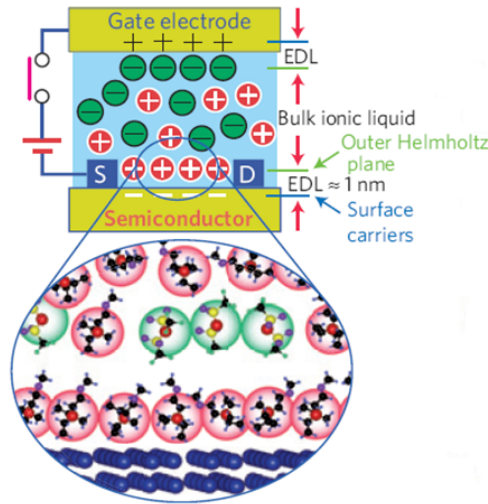


Figure 2.1.2: Interface between the ionic liquid and semiconductor of a typical EDL-FET. From [28].

By improving the properties of electrolytes, charge accumulation in EDL-FETs can be further enhanced [22]. Different electrolytes, such as aqueous, organic, gel and polymer electrolytes, can be used. However, ionic liquids (ILs) are highly promising as a dielectric gate material for FETs and FET-based devices, as shown pictorially in Figure 2.1.3.

Ionic liquids, literally “liquid salts”, are molten, organic salts or eutectic mix-

tures of an organic salt and an inorganic salt that have a melting point or glass-transition temperatures below 100 °C [29, 30, 31]. These liquids are constituted by organic and/or inorganic ions containing more than one cation or anion. Their highly non-isotropic nature results from their strong electrostatic and dispersive interactions at various length scales. They have key advantages such as high thermal and chemical stability, non-volatility, non-toxicity, the existence in a fluid state over a wide temperature range, and more. Moreover, they can be exposed to a high potential difference without suffering redox reactions due to their large electrochemical windows. Consequently, interest in room-temperature ILs, known in the literature as "green solvents" as they are used as a suitable replacement for volatile organic solvents, has increased enormously over the past decade [31]. This is because one of the crucial parameters in the choice of gate dielectrics is the specific capacitance, which in turn decides the number of carriers that can be induced in the semiconductor channels of FETs at a specific gate voltage. The accumulated charge Q in a parallel-plate capacitor is given by the product of the capacitance C and the applied voltage V , i.e.

$$Q = CV \tag{2.1}$$

Thus, a high C translates into a high charge density. More specifically, C is given by

$$C = \frac{\epsilon_o \epsilon_r A}{d} \tag{2.2}$$

where ϵ_o and ϵ_r are the vacuum and the relative permittivities, respectively, A is area of the plates and d is the distance between the two plates. Even though the ϵ_r values of ionic liquids range approximately between 1 and 10, as determined using dielectric spectroscopy in different cases of study ([32, 33]), ionic liquids can exhibit a high capacitance in excess of $10 \mu\text{Fcm}^{-2}$ due to the formation of EDLs on the semiconductor surfaces (Figure 2.1.2). These properties allow also the observation of the high operating speeds of ion-liquid EDL-FETs, of the order of up to MHz [31].

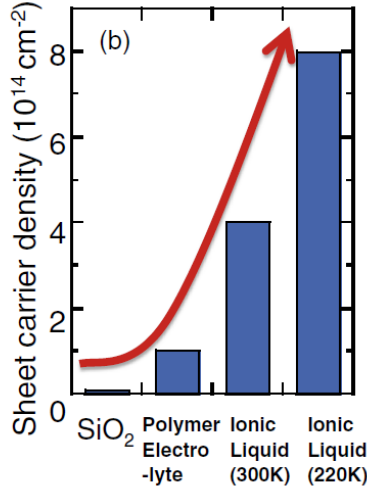


Figure 2.1.3: A comparison of gating efficiency in terms of maximum reached carrier density among IL gating, polymer electrolyte gating, and a solid dielectric [22].

Hence, using the potential of ionic gating, mainly within the electrostatic limit, i.e. by accumulating ions only on the surface of the material and exploiting the ultrahigh electric field originating in the EDL [22], it is possible to control the transport properties of a broad spectrum of materials, including metal chalcogenides, 2D materials and even metals. In particular, good results emerged via electric-field controllable ionic liquid gating (ILG). As summarized in [23], ILG has enabled improvements in the critical temperature of certain superconductors, inducing metallic behaviour in insulators, or even superconducting phases in certain compounds like SrTiO₃ [25], ZrNCl [28] and KTaO₃ [34]. These results are achieved not only through consolidated electrostatic doping but also by inducing phase transformation with ion transfer via its intrinsic electrochemical effect [35], i.e. by intercalating ions between Van der Waals-bonded layers to control the entire properties of the bulk [36], as discussed in more details in the next sections.

2.2 Ionic-Gating-induced Ion Intercalation

The properties of layered materials can be altered through ion intercalation, i.e. the controlled insertion of ions in the crystal lattice of the host materials. When ions penetrate the interlayer spaces, they can form chemical bonds with the atoms of the hosting materials [37], altering its properties. The positioning of ions between the layered unit cells decreases the coupling among them, increasing the space in between, as we can observe in the representative Figure 2.2.1. As a consequence, there is a direct impact on several material's properties. From an electronic point of view, we have charge doping and the possible insertion of electronic states of the chosen ions into the band structure of the host material. We

can also obtain crystalline structure modifications.

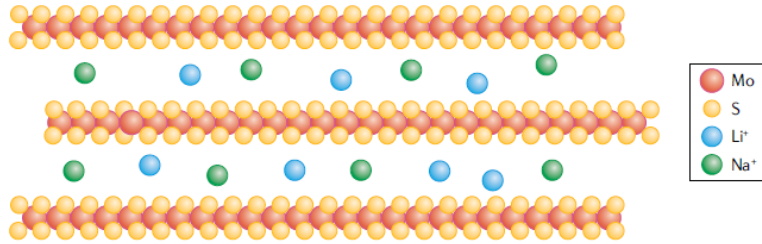


Figure 2.2.1: Schematic ion intercalation of Li^+ and Na^+ in a layered structure of MoS_2 . From [37].

It is well known that ion intercalation can be carried out through element doping methods and ion-beam implantation. However, these techniques have some drawbacks; e.g., the former can lead to the formation of dopant clusters, while the latter is limited to surface layers [38]. Therefore, considering the potentialities outlined in the previous section, the ILG technique is used as an alternative, relatively simple and more effective than the conventional approaches to induce ion intercalation.

Over the past decade, ion intercalation studies have mainly focused on layered materials, such as transition metal dichalcogenides (TMDs) deeply described in Chapter 5, and on the resulting modulation of their bulk carrier density. We can find in the literature several study cases based on ion intercalation, mainly performed using alkali ions.

For example, Yu et al. [39] described the gate-controlled Lithium (Li^+)-intercalation into layered crystals of 1T-TaS₂. Since this material presents a naturally high charge concentration, a higher doping level is necessary to tune the electronic properties of 1T-TaS₂. For that purpose, ion intercalation was revealed more effective than the conventional techniques (e.g. FE, electrostatic ILG). Moreover, at low temperatures, the ionic gating induces multiple phase transitions from Mott-insulator to metal in 1T-TaS₂ thin-flake samples. Also Klemm reported in his review [40] that several TMDs (2H-MoS₂, 2H-TaS₂, 1T-TaS₂, 4H(b)-TaS₂, 2H-ZrS₂, and 2H-ZrSe₂) were made into layered superconductors through ion intercalation with alkali ions. The final compounds are configured as very air-sensitive and rather 3D in their properties.

More recently, in 2017 Lu and co-workers [35] gave much emphasis mainly to the evolution of single ionic species, such as Li^+ , Potassium, Hydrogen and Oxygen ions (K^+ , H^+ , O^{2-} , respectively), without delving into the effects of various ionic species on the same ion-gated material. However, as can be deduced from ion-gating experiments conducted on the layered semiconductor MoS₂ employing Li^+ and K^+ as dopant ions [36], the choice of ion species and size in ion-gated devices can profoundly alter the properties of the host material. Indeed, field-driven

intercalation using different electrolytes within the same material and device architecture has led to different phase diagrams for the intercalated state. More specifically, MoS₂ undergoes an insulator-to-metal-to-superconductor phase transition when intercalated with Li⁺. In contrast, in the case of the K⁺, which is bigger in size than Li⁺, its dimensions make gate-driven intercalation of MoS₂ lattice difficult, introducing distortions and defects into its entire volume. Thus, a typical behaviour close to a metal-to-insulator transition is observed at high doping levels [36].

2.3 Ionic-Gating-Induced Protonation

When ion intercalation is performed through the insertion of H⁺, this process is more properly called protonation or hydrogenation.

If the gating process is carried out at ambient conditions, for negative gates, the internal electric field can drive the negatively-charged O²⁻ ions into the films to control the oxygen vacancies, as sketched in Figure 2.3.1a. Whereas, the application of a positive gate voltage in excess of the hydrolysis potential (at least 1.23 V) splits the water absorbed by the electrolyte into OH⁻ and H⁺ ions, as shown in Figure 2.3.1b. Then, the free H⁺ ions can be driven into the crystal lattice. The reversed gating can induce the extraction of the corresponding ions for both cases. Water electrolysis was claimed as one of the most promising origins for O²⁻ and H⁺ ions.

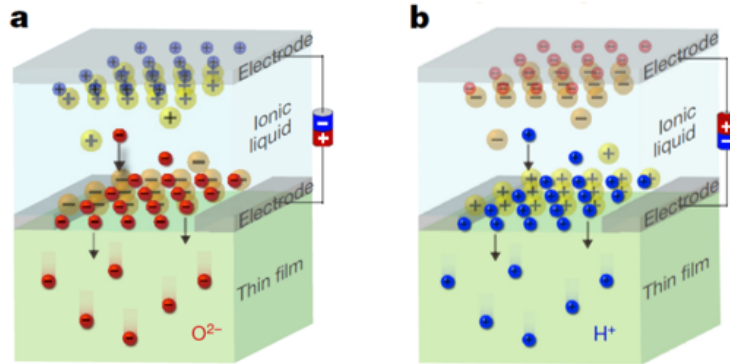


Figure 2.3.1: Schematic diagrams of the transport and storage of (a) oxygen and (b) hydrogen ions with negative and positive external gating voltages in an ionic liquid gating device, respectively [35].

X-Ray Diffraction (XRD) analyses are used to provide evidence of possible structural transitions between different phases, as suggested in [35]. Thanks to this technique, it is possible to observe shifts in the diffraction peaks attributed to the increase of the interlayer spacing induced by ion intercalation [37]. Lu et al. demonstrated that the ILG-induced phase transformations occur with several

ionic liquids, which have sufficient residual water to achieve the phase transformation, proving the generic nature of the ILG-induced phase transformations [35]. XRD measurements both *in situ*, during ILG, and *ex situ* are necessary to confirm the non-volatility of the transformation. Indeed, one of the main advantages of ionic-gating-induced protonation is that, when stable intercalation is obtained, the H^+ or hydrogen-rich organic ions insertion is non-volatile, allowing several post-gating measurements[41].

ILG experiments on transition metal oxides have successfully proven the reversible tuning of the concentration of both oxygen vacancies and hydrogen ions. For example, a careful study [35] has shown how through electric field control it is possible to achieve a reversible and not volatile tri-state phase transformation among $SrCoO_{2.5}$, $SrCoO_3$, and a previously unknown phase, $SrCoO_{2.5}H$. Working with the electric field control means exploiting the ultra-high electric field generated by the polarized electrolyte to drive the ions accumulated in the EDL in and out of the crystal lattice once sufficiently large gate voltages are applied. Figure 2.3.2 provides an illustration of these three different stoichiometrically-stable crystal structures, based on first principle calculations, in which both hydrogen and oxygen ions are mobile.

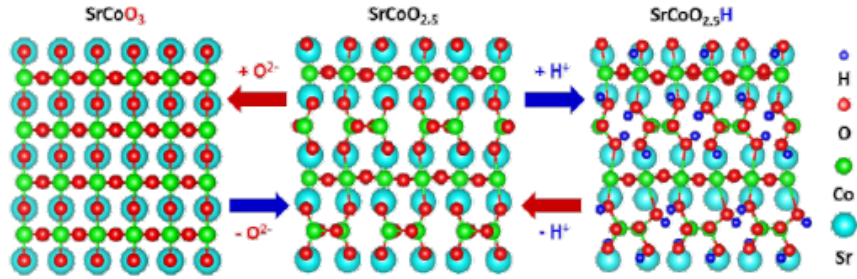


Figure 2.3.2: Reversible phase transformation of $SrCoO_{2.5}$ through the electric-field selectively controlled dual-ion (O^{2-} and H^+) switch. The red and blue arrows represent negative and positive voltages, respectively [35].

In addition, as reported in the case of the strontium cobalt oxyhydride, the electric-field-controlled phase transformation can also be accompanied by the modulation of optical and magnetic properties [35]. Furthermore, since charge transfer changes the carrier density, electric transport measurements allow us to analyse essential intercalation aspects: this is one of the main focal points that we have developed in the experimental part of this project.

This approach has also been regarded as a powerful tool in the study of high T_c superconductors, in particular, to address the emergence of superconductivity from an insulating parent compound. For example, $La_{2-x}Ce_xCuO_4$ (LCCO), an electron-doped high- T_c cuprate, undergoes a superconductor-insulator transition upon protonation induced via ILG. Moreover, it was highlighted that applying negative voltages can reverse the protonation process and also recovers supercon-

ductivity in samples deteriorated by moisture in the ambient [42].

In 2018 Cui and collaborators [43] applied this method to iron (Fe)-based superconductors. Accumulation of H^+ in bulk crystals induces superconductivity in the parent compounds, such as the $FeSe_{1-x}S_x$ and the $BaFe_2As_2$ structures, and increases the superconducting transition temperature through an electron doping effect. A year later, as reported in [41], under optimised protonation conditions, i.e. with a protonation temperature of 350 K, which improve proton diffusion efficiency in the crystal, and with a gating period of 12 days, in which water is nearly completely electrolyzed, with the ILG method (shown in Figure 2.3.3) it was possible to enhance the superconducting volume ratio and the doping homogeneity.

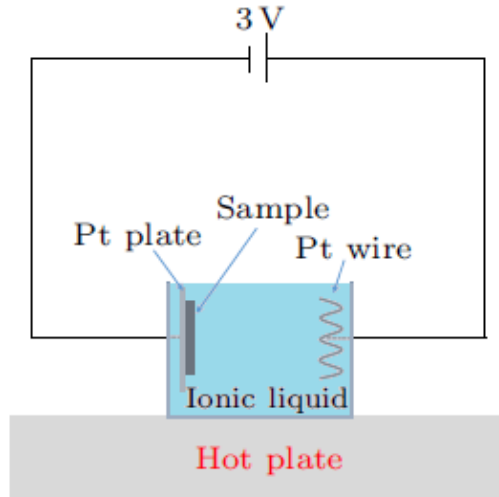


Figure 2.3.3: An illustration of the protonation setup adapted from [41]. Platinum electrodes are placed in a container filled with the ionic liquid. The gating voltage is set to be about 3.0 V. The ionic liquid is heated up to 350K by a hot plate.

More in detail, in $FeSe_{0.93}S_{0.07}$, under optimised gating conditions, a single high- T_c phase, around 43.5 K, was reached [41]. Superconductivity was determined not only through magnetization measurements but also via transport measurements. Figure 2.3.4 shows the resistance behaviour as a function temperature, $R(T)$, of the protonated $FeSe_{0.93}S_{0.07}$ single crystal. Furthermore, the existence of protons in the lattice was proved by means the proton nuclear magnetic resonance (NMR), which allowed the authors to probe directly the presence of hydrogen.

More recently (in 2022), Meng et al.[44, 45] also analysed protonated FeSe. They found discrete SC phases in H_x -FeSe single crystals, either during protonation or deprotonation stages, with a maximum T_c of 44 K. The crystalline structure of H_x -FeSe resulted unaffected by the protonation process. That demonstrated that the discrete SC phases are intrinsic and strictly related to the carrier con-

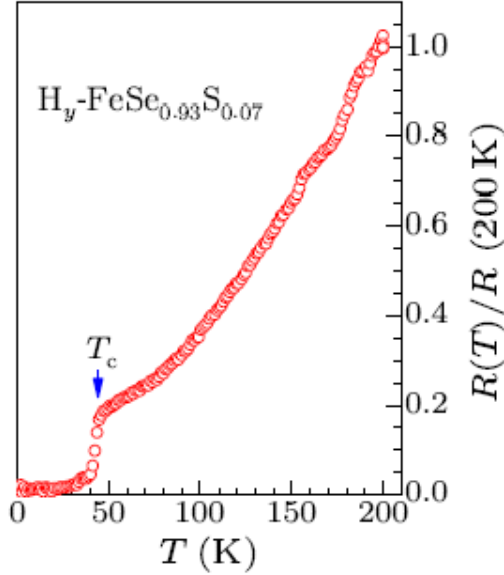


Figure 2.3.4: The resistance of $H_y\text{-FeSe}_{0.93}\text{S}_{0.07}$ vs temperature. The arrow indicates the superconducting transition around 43.5 K. From [41].

centration; that is, the FeSe interlayer distance is not decisive in reaching high- T_c superconductivity. These SC phases have been justified by a Lifshitz transition, namely a sudden change in the Fermi surface topology [44]. The same authors also highlighted in a following paper that the relatively low T_c and small critical current density (J_c) of FeSe limited many of its technological applications [45]. They demonstrated that the intercalation of H^+ into FeSe enhanced both these key factors. In particular, the maximum T_c reached was confirmed at 44 K, with a bulk SC property, while the J_c value was $1.3 \times 10^6 \text{ A cm}^{-2}$, two orders of magnitude higher than the one detected in the pristine sample [45].

Optimised protonation has been successfully applied to various layered compounds, including insulating ZrNCl, 1T-TaS₂ and Bi₂Se₃. Briefly summarizing, superconducting transitions with $T_c \sim 15 \text{ K}$ for ZrNCl, $\sim 7.2 \text{ K}$ for 1T-TaS₂, and $\sim 3.8 \text{ K}$ for Bi₂Se₃ are induced after protonation. Table 2.1 presents all the of different T_c compounds previously mentioned, before and after protonation under the current optimized conditions [41].

Compound	FeSe	FeSe _{0.93} S _{0.07}	ZrNCl	1T-TaS ₂	Bi ₂ Se ₃
$T_{c,\text{before}}$	9 K	8 K	0	0	0
$T_{c,\text{after}}$	41 K	43.5 K	15 K	7.2 K	3.8 K

Table 2.1: T_c of the materials before and after protonation [41].

In addition to several studies on alkali metals coinserted with inorganic or organic molecules into FeSe, various new superconductors were also found simply by intercalating organic composites. For example, tetrabutylammonium (TBA⁺) and cetyl-trimethylammonium (CTA⁺) have been successfully intercalated into FeSe by electrochemical intercalation as shown in [18] and [46], respectively. More in detail, the (CTA)_{0.3}FeSe presents a high T_c about 45 K and a higher crystallinity whereas the (TBA)_{0.3}FeSe shows T_c of 50 K at ambient pressure. This is a result of both the electron doping of the FeSe plane and the minimal interaction of the FeSe with organic ions, which minimises the production of impurity phases and disorder in the FeSe plane. Moreover, always in the same gating conditions of the FeSe_{0.93}S_{0.07}, it is possible to observe an increase in T_c, starting from 8.5 K to above 41 K, not only by conventional methods but also by ionic-liquid/solid gating, as thoroughly reported in [43] and references therein. A rapid drop of susceptibility χ at 41 K indicates the onset of superconductivity. However, it is unclear what is the exact superconducting phase. Recently, Wang et al. [47] established from XRD studies (panel a in Figure 2.3.5) that the relevant phase is not H_y-FeSe but rather another organic-ion-intercalated FeSe, i.e. (EMIM)_xFeSe (panel b in Figure 2.3.5). These novel FeSe-based superconductors T_c is 44.4 K, as shown by temperature-dependent magnetic susceptibility and resistivity measurements. Nevertheless, these samples turned out not to be very stable in the atmosphere, and after a few days, they will degrade back to the pristine FeSe with a T_c of about 8 K. Shortly comparing the results obtained between the protonated FeSe and the organic-ions-intercalated one, we have that the group with the organic-intercalated FeSe [47] uses higher gate voltages (+4 V) than the group with the hydrogen-intercalated FeSe (+3 V) [44, 45]. The difference between the two phases obtained is that the organic-intercalated FeSe presents a crystalline cell swollen due to the dimension of the cations, compared to the hydrogen-intercalated FeSe.

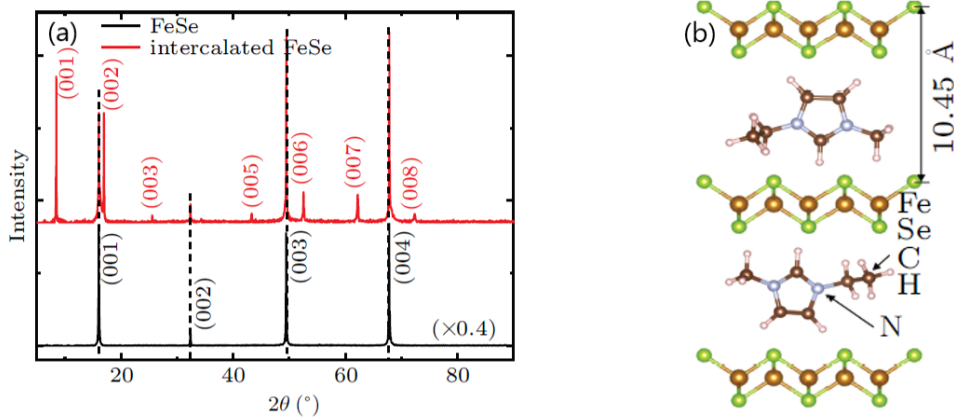


Figure 2.3.5: (a) XRD patterns of FeSe single crystal (in black) and intercalated FeSe (in red); (b) Schematic crystal structure of (EMIM)_xFeSe. Adapted from [47].

Concerning the intercalation of organic ions, Zhang et al. [48] engineered organic-inorganic hybrid crystals starting from MoTe_2 and WTe_2 , using an ionic liquid $[\text{C}_n\text{MIm}]^+ [\text{TFSI}]^-$ (1-Alkyl-3-Methylimidazolium-Bis (TriFluoroMethylSulfonyl) Imide) with $n=1,2,3,\dots$. Specifically, the ions generated are large organic cations, sensitively increasing the interlayer spacing of the host materials. They observed a global enhancement of the critical temperatures. In particular, they got a $T_c = 7$ K for intercalated MoTe_2 (starting from $T_c=0.25$ K for the pristine material) and $T_c=2.3$ K for the intercalated WTe_2 (2.8 times the value of T_c for the monolayer material). This boost can be ascribed to the introduction of additional phonon modes.

These findings showcase how promising it may be to investigate the effects of gate-driven H^+ or hydrogen-rich organic ion intercalation in other materials.

Chapter 3

Gate-Driven Protonation and Intercalation: The Experimental Approach

In this chapter we discuss the experimental details of the protonation technique by describing the experimental set-up that was implemented to conduct the main experimental part of the project. Finally, we briefly mention the data analysis tools we used to analyse the data acquired.

3.1 Fabrication of the experimental setup

This section describes the experimental setup used for material characterization, which is adapted from the one typically employed in ionic gating experiments, previously mentioned in section 2.3. In its simplest version, this technique requires only a low DC gate potential ($V_G \sim 3$ V), water naturally absorbed by hygroscopic ionic liquids and a temperature of around 300 K [1]. In this thesis project, protonation was realised using a home-built setup to allow *in situ* measurements of the sample gate current and voltage as well as its resistance in real time. A conceptual example of the setup is shown in Figure 3.1.1a. In particular, by placing a reference electrode in the electrolyte, it was possible to measure the gate voltage V_G , the reference voltage V_{ref} , the gate current I_G and temperature simultaneously during the gating phase. In addition, the placement of appropriate contacts on the sample surface also permitted *in situ* measurement of its four-wire resistivity. A similar configuration was made to be mounted in a cryostat, allowing both *ex situ* (post-gating) and direct *in situ* measurements at low temperature.

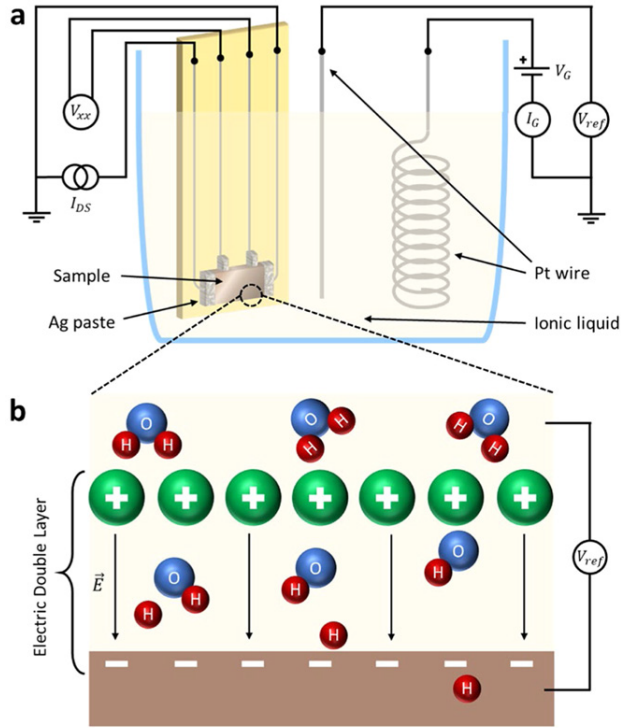


Figure 3.1.1: (a) Illustration of the experimental setup for ionic-gating-induced protonation, showing the Pt wires used for applying the gate voltage (V_G) and measuring the sample's four-wire resistivity as well as the reference voltage (V_{ref}). (b) The Helmholtz layer of cations and the counter-charge in the gated sample make up the EDL, which is shown schematically as a positive V_G . From [1]

The fabrication process of the setup used in the experimental part of this thesis was carried out as described below and shown in Figure 3.1.2.

Starting with a sheet of coppered FR4 vetronite (standard thicknesses: coppered layer $35\mu\text{m}$, insulating layer (vetronite) 1.5 mm), a sample holder of dimensions $1.0\text{ cm} \times 1.5\text{ cm}$ was constructed. Next, an area of approximately 1.0 cm^2 copper (Cu) (1) was manually removed. Then, in the remaining approximately 0.5 cm^2 of conductive material, the conductive tracks to accommodate the voltage and current contacts were traced using an etch-resistant ink marker (2) and patterned via wet etching using a ferric chloride (FeCl_3) bath. A larger-extension board ($3.0\text{ cm} \times 1.5\text{ cm}$) was produced following the same steps. The two parts (sample holder and extension board) were connected through five soft enameled copper wires with a diameter of around $500\mu\text{m}$ and a length of approximately 4 cm (3). The wires were soldered to the board pads with standard tin (Sn) solder after removing the surface oxide via wet etching in phosphoric acid (H_3PO_4).

After wet-etching these cables and cleaning the conductive parts of the two boards with phosphoric acid (H_3PO_4), they were soldered through a tin (Sn) wire on the extended board and via both Sn and indium (In) wires on the sample holder.

Subsequently, five similar cables, but with a larger diameter and length (1 mm and 10 cm, respectively) were soldered on the opposite side of the extended board in order to be connected directly with the terminals of the measuring instruments used in the next phase of material characterisation (4). A Pt wire was then soldered in one of the external bonding pads of the sample holder to act as the reference electrode.

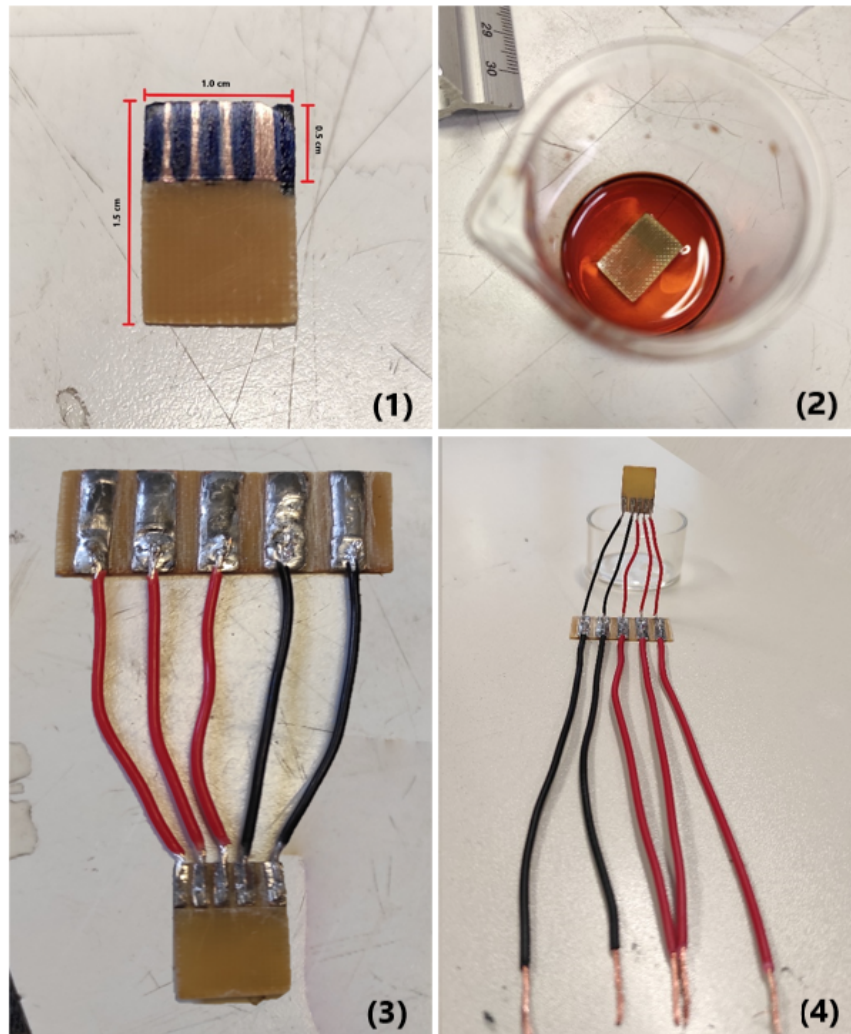


Figure 3.1.2: Experimental setup building process: (1) realization of the sample holder; (2) etching process; (3) connection to a larger extension boarder; (4) final configuration.

Once a sample holder was completed, a typical sample used in the protonation experiments was mounted as follows: the sample, after being carefully selected, was electrically contacted using gold wires (17 μm of thickness) through drop-casted spots of silver conductive (Ag) paste (RS Components). The whole device is then immersed in a Duran crucible filled with an electrolyte (Figure 3.1.1a).

Specifically, experiments were performed using two different electrolytes: 1-ethyl-3-methylimidazolium tetrafluoroborate ionic liquid (EMIM-BF₄; Merck KGaA) and GT90 (non commercial deep eutectic solvent (DEP), composed of a mixture of glycerol and choline chloride, synthesized by collaborators at the University Of Pisa). The gate (G) electrode was made from a coiled Pt wire (Figure 3.1.1a); then, the gate voltage V_G between the Pt electrode and the crystal was applied using a B2961 power source (Keysight Technologies) at near-room temperature and in an ambient atmosphere.

During the experimental phase, several weaknesses in the setup emerged, for which improvements were designed and implemented. Firstly, the original Ag paste was replaced with the Silver Conductive Epoxy (H2OE EPO-TEK) [49] and/or PELCO® High Performance Silver Paste [49]. The decision to use these pastes, rather than the original one, was dictated by the instabilities developed during prolonged protonation times caused by oxidative phenomena in contact with the ionic liquid. That resulted in contact instabilities or even their complete degradation. In addition, to increase the wear and abrasion resistance of the sample holder, a replacement setup with glass instead of vetronite was realised.

3.2 Materials and methods

In the following subsections, the characterisation techniques performed on the selected material samples and the data analysis tools used to process and present the data in the following chapters are briefly presented.

3.2.1 Characterization techniques: a general introduction

Three selected materials were analyzed, including Palladium (Pd), Palladium-Copper Alloy Pd_{0.6}Cu_{0.4}) (Chapter 4) and Molybdenum Disulphide (MoS₂) (Chapter 5). Table 3.1 shows schematically the types of characterisation that were performed for each material and that are introduced in the following subsections.

	Pd	Pd_{0.6}Cu_{0.4}	MoS₂
Electric-Field-Driven Ion Intercalation	X	X	X
Resistivity Measurements	X	X	X
Vibrational Spectroscopies Raman and Fourier-transform infrared spectroscopies			X
Nano-Infrared Microscopy			X
Kelvin-Probe Force Microscopy			X
X-Ray Diffraction		X	
AC Susceptibility		X	

Table 3.1: Overview of the characterization techniques applied on each material.

3.2.1.1 Electric-Field-Driven Ion Intercalation

According to the setup described in the previous section, the resistivity was monitored *in situ* using the standard 4-wire method throughout the process. In general, this phase of the experiment was conducted at room temperature ($T_{room} \sim 295$ K) and in ambient atmosphere; however, in a few cases, with the PdCu, we performed the measurements by pre-heating, via a digital stirring hotplate (Corning), the device immersed in the ionic liquid up to a temperature of 57° C. Specifically, the most significant outputs were the resistivity values before and after immersion of the device in the ionic liquid and its trend after the application and attainment of a suitable gate voltage. Using a Keithley 220 current generator, a constant current I_{DS} , selected according to the material under investigation in the range between 100 nA and 1 mA, was supplied to flow between the D and S contacts. A HP 3457 multimeter was used to measure the longitudinal voltage drop V_{xx} between the voltage contacts, and it was then possible to determine the resistivity ρ which is given by

$$\rho = V_{xx} I_{DS}^{-1} t w l_c^{-1} \quad (3.1)$$

where t and w are the sample thickness and width, and l_c indicates the channel length between the inner voltage contacts. Furthermore, we employed the current-reversal method to remove the common-mode offsets. In electrical measurements, the reversal technique is used to get a genuine value of a physical quantity of interest without unwelcome signal offset, removing some of the most significant sources of systematic error.

Here, we used the current-reversal method to reduce the thermoelectric voltages (or thermoelectric EMFs). These latter develop when different circuit parts are at different temperatures and when dissimilar materials conductors are combined [50, 51, 52]. It is necessary to perform two measurements with opposite polarity currents to compensate for thermoelectric voltages, as presented in Figure 3.2.1.

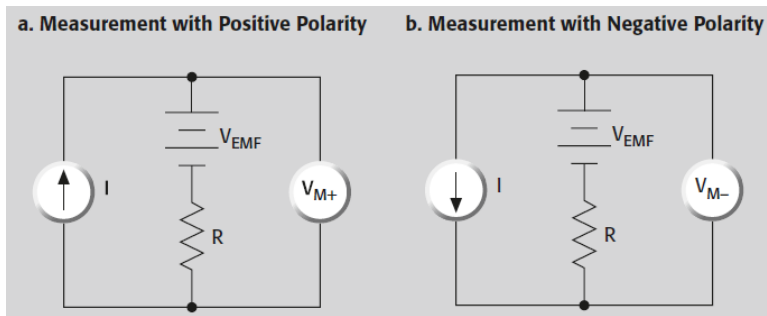


Figure 3.2.1: Sketch of the circuit of the current-reversal method. Adapted from [50]

In particular, the measured voltages in the two current sign configurations are:

$$V_{M+} = V_{EMF} + IR \quad (3.2)$$

$$V_{M-} = V_{EMF} - IR \quad (3.3)$$

So, combining these two measurements, Thermoelectric voltages cancel:

$$V_M = \frac{V_{M+} - V_{M-}}{2} = \frac{(V_{EMF} + IR) - (V_{EMF} - IR)}{2} = IR \quad (3.4)$$

Consequently, the resistance is simply given by:

$$R = \frac{V_M}{I} \quad (3.5)$$

which is completely independent of V_{EMF} [50].

Getting back to the electric-field-driven ion intercalation procedure discussion, we realized open circuit conditions by physically disconnecting the gate electrode from the power generator. In Figure 3.2.2 are reported two scenarios of the electric-field-driven ion intercalation setup either at T_{room} (panel a) or at higher temperature (panel b).

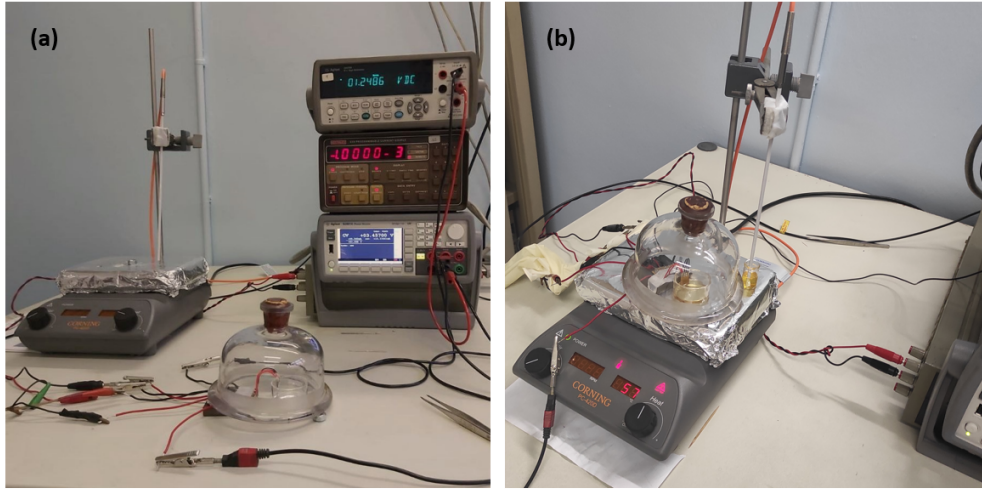


Figure 3.2.2: (a) common electric-field-driven ion intercalation setup at room-temperature and (b) at higher temperature (= 57°C). Panel (a) also shows the measuring instruments used during this part of the experiments.

After removing the intercalated samples from the cell and carefully cleaning them with acetone and ethanol to eliminate ionic-liquid residues, *ex situ* characterizations were carried out.

3.2.1.2 Electrolyte

To perform the field-driven ion intercalation experiments, we used two different electrolytes, namely the 1-ethyl-3-methylimidazolium tetrafluoroborate ionic liq-

uid (EMIM-BF₄) and the deep eutectic solvent (DES) GT90.

Specifically:

- **EMIM-BF₄** is considered the prototype for ionic liquids at room temperature and is widely used as an electrolyte in electrochemical studies. It consists of the EMIM⁺ organic cation and the BF₄⁻ anion, as shown in Figure 3.2.3. It is an organic ionic liquid with several advantageous characteristics, including a low melting point (~ 15°C), a high boiling point (above 350°C), a low viscosity, a high ion density and conductivity, and finally a high electrochemical stability window (up to 4.3 V) [53, 54].

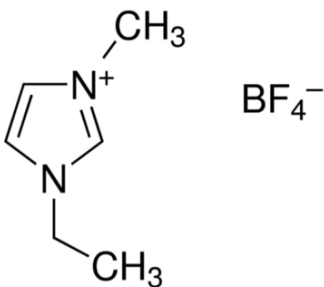


Figure 3.2.3: Structural formulas 1-ethyl-3-methylimidazolium tetrafluoroborate ionic liquid.

- **GT90** is a non-commercial DES supplied by our collaborators from the electrochemistry group at the Department of Pharmacy of the University of Pisa. DESs are classified as electrolytes, which can considerably reduce the melting points compared to their individual components. Their reduced melting points and physico-chemical characteristics are believed to be the result of complex hydrogen bondings [55]. The hypothesis behind the choice of GT90 is implicit in its composition, whose components are schematised in the Figure 3.2.4. Indeed, when a sufficiently large voltage is applied, glycerol turns out to be a source of H⁺ from the hydroxyl groups (-OH) [56]. In contrast, choline chloride, in addition to being able to release H⁺ from its -OH group, is the primary source of ions (N⁺ and Cl⁻) that impart conductive capacity to the electrolyte [56].

3.2.1.3 Resistivity Measurements

We used the ST-403 pulse-tube cryocooler (Cryomech), shown in panel a of Figure 3.2.5, with a base temperature of about 2.8 K for the measurements of resistivity as a function of temperature. The resistivity was calculated using the same procedure previously described for T_{room} resistivity, with the exception that I_{DS} was provided by a B2912 source-measure unit from Keysight Technologies, and V_{xx} was measured using a 34420 nanovoltmeter. Only the information gathered during the slower, quasi-static warming to T_{room} was taken into account for each

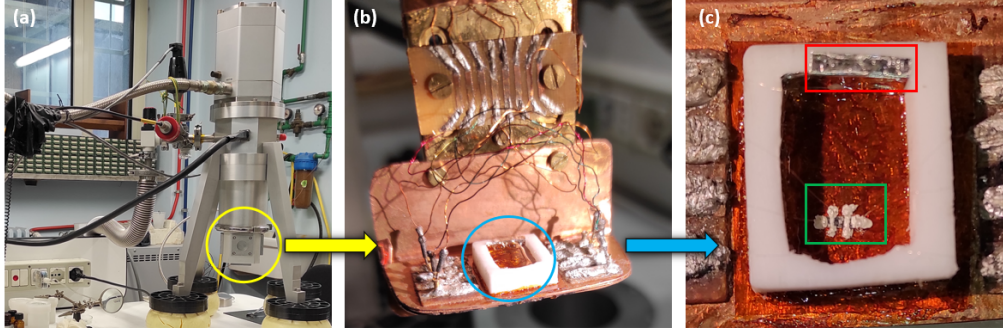


Figure 3.2.5: (a) ST-403 pulse-tube cryocooler with a closeup on the cryochamber; (b) cryocooler sample holder with a magnification on the teflon cell holding the ionic liquid, the sample electrically contacted with the Ag paste (green rectangle in (c)) and the gate electrode (red rectangle (c)).

Furthermore, after we performed the field-driven ion intercalation at the laboratories of the Politecnico di Torino, we sent selected samples to the Quantum Matter Physics department of the University of Geneva. There, they performed further characterizations of temperature-dependent Raman spectroscopy and low-temperature scanning tunnelling microscopy. The results are introduced in Chapter 5, devoted to our studies of the MoS_2 samples.

3.2.2 Data Acquisition and Analysis tools

The instrumentation for the electrical transport measurements and field effect experiments is remotely controllable. Data were collected through LabVIEW software and subsequently managed and represented through Origin software, or via MATLAB. LabVIEW is a software produced by the National Instrument Corporation, designed for system design and the development of automated test, measurement and control applications with quick access to hardware and results [57]. Origin is an analysis and graphics software produced by OriginLab Corporation [58]. MATLAB is a proprietary multi-paradigm programming language and numeric computing environment developed by MathWorks [59].

The software integrated into the spectroscopy and microscopy instruments were also used. In addition, the analysis of the acquired maps was performed using the Gwyddion software developed and distributed by the Czech Metrology Institute [60].

Chapter 4

Palladium and Palladium-Copper Alloy

4.1 General description of Palladium

Palladium (Pd) is a transition metal in the Xth group of the periodic table and it represents one of the most important members of the platinum metal group; more precisely, it has the lowest melting point (~ 1828 K) and is the least dense (~ 12.0 g/cm³) of the group [61]. Pd presents a face centered cubic (FCC) crystal structure, as shown in Figure 4.1.1; therefore, it has two kinds of potentially available interstitial sites that repeat throughout the lattice: octahedral and tetrahedral [62]. Pd can be found as a free metal or alloyed and it is mostly used in membrane separation systems [63]. Other interesting applications are in jewelry, medical, aerospace and electrical contacts [64, 65].

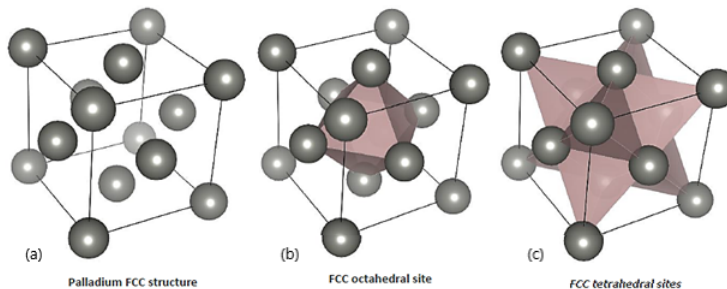


Figure 4.1.1: The face centered cubic (FCC) crystal structure with its two available interstitial sites: octahedral (b) and tetrahedral (c). Adapted from [62].

Moreover, one of the best-known metal hydrides is palladium hydride, reported the first time by Graham in 1866 [66]. Indeed, Pd can reversibly absorb large amounts of hydrogen (H) from H₂ gas at less than 1 atm pressure at room temperature, up to H/Pd = 1 [67].

The phase diagram for the system Pd-H is reported in Figure 4.1.2 and it consists of the α and β phases, in both of which the H occupies, randomly, the interstitial octahedral sites of the FCC Pd lattice, as confirmed by neutron diffraction studies [68]. Lattice parameters of both α and β phases are greater than that of the pristine Pd. The α phase is the low-concentration phase of the system, while the high-concentration one is β . A mixed ($\alpha + \beta$) phase region is present in between [69].

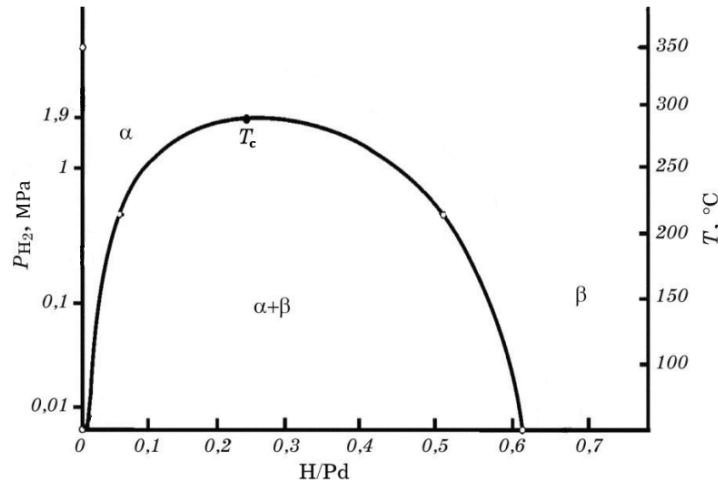


Figure 4.1.2: Pd-H system phase diagram. Adapted from [70].

At near room temperature, the maximum concentration of the H atoms in the α phase is approximately $x = 0.02$, whereas the single β phase exists for higher concentrations ($x > 0.60$) [69, 68]. This latter has a larger lattice and therefore the phase transition involves a crystal expansion with a consequent increase in volume. The two-phase region in Figure 4.1.2 delimited by the coexistence curve approaches the critical point near $T_c = 290$ °C and for a hydrogen concentration of 0.29. Above this critical point, α and β are not distinguishable coherently with the applicability of the lattice gas model for the Pd-H system [69].

As reported for the first time in 1957 by Nace and Aston [71] the Pd-H system shows an anomalous behaviour in term of specific heat around 50 K. These anomalies are also found in resistivity, internal friction and Hall coefficient measurements [72, 73]. Throughout the years, several hypotheses have been suggested to justify the presence of these anomalies. Neutron diffraction studies suggest a partial migration of the hydrogen atoms from their octahedral interstitial sites to the tetrahedral positions of the FCC palladium crystal structure in the low temperature region [72, 73]. Also, a possibility of a structural transition of the martensitic type [73], i.e. a diffusionless transformation without any interchange in the position of neighbouring atoms [74], was considered.

However, thanks to scattering experiments on the β - phase of the Pd-H system in

the temperature range of 5 - 300 K performed in 1975 it was possible to establish that the hydrogen atoms always resides in the octahedral interstitial sites in the palladium lattice [69, 75]. In addition, also the second possibility was discarded according to X-ray diffraction measurement. Indeed, no distortion has been observed [73, 76]. Nevertheless, the possibility of occupation of the tetrahedral interstitial sites in the palladium lattice and the way to define "occupation" are still open questions [62, 77].

In 1972, according to magnetic susceptibility measurements, it was possible to observe that the α - phase presents a quite large temperature-dependent susceptibility, similar to that of pure palladium, while the susceptibility of the β - phase is slightly diamagnetic and almost independent of temperature [78]. In the same year, superconductivity for the Pd-H system at near $x = 0.9$ and critical temperature around 5 K was discovered [79]. It was observed that the transition temperature, T_c , strongly increases with increasing concentration of hydrogen. These results have been confirmed and enhanced by Stritzker and Buckel, who obtained a T_c near 9 K with a concentration x around the unity [11]. So, despite the decrease in the electronic density of states at Fermi energy by a factor of 6 when x ranges between 0 and 0.9, the extinction of Pd paramagnetism was the crucial prerequisite for superconductivity in Pd [80, 81]. In 1980, it was empirically demonstrated that the T_c increases with increasing hydrogen concentration, according to the following relationship [82]:

$$T_c = 150.8(x - x_0)^{2.244} \quad (4.1)$$

where x_0 is equal to 0.715 for PdH $_x$.

Therefore, it is necessary to have a high concentration of hydrogen to trigger the superconductivity. Moreover, particular attention is necessary to avoid the rapid desorption of hydrogen from palladium. For these purposes, the ion intercalation technique is very successful [83].

As it is deducible from the previous paragraphs, most of the literature concerning the Pd-H system is antecedent to 1980. It was not until the early 2000s that there was a renewed interest in the possibility of high temperature superconducting phases in Pd hydride, in addition to the well-known low temperature superconducting phase ($0 \leq T_c \leq 9$ and $0.73 \leq x \leq 1$) [79]. Indeed, Tripodi et al. [9, 84, 85] claimed to have observed superconductivity in electrolytically loaded PdH $_x$ with T_c in the range of 51 and 295 K, managing to maintain the H/Pd ratios above 1 at room temperature and pressure. They tried to limit the hydrogen migration from the sample using a nanometric Pd-Hg amalgam.

The work of Lipson et al. [9, 86, 87, 88] provides a second hint that PdH $_x$ exhibits high- T_c superconductivity. They explained the unusual diamagnetic contribution observed in the magnetic susceptibility measurements through the filamentary superconductivity phenomenon. In particular, that develops in presence of a high

density of hydrogen that results trapped in dislocation nuclei. Referring to the phase diagram, this manifests after passage across the biphasic area that spans the miscibility gap between the α and β phases.

However, most of these results are highly debated and have not been confirmed until now. The gradual loss of hydrogen could be the cause of the decrease in T_c after storage. This observation therefore gives us a hint of how to proceed in order to try and achieve higher T_c [9, 83].

Therefore, one of the purposes of our measurements was to verify if the anomalies presented above were also present with the electric-field-driven ion intercalation we have exploited at ambient pressure and room temperature, and thus in less critical conditions. Finally, we tried to verify if a sign of superconductivity arose at high temperature.

4.1.1 Results and discussion

4.1.1.1 Electric-Field-Driven Ion Intercalation

Palladium samples (typical size approx. 2 mm \times 0.5 mm \times 25 μ m) were obtained by cutting a commercial Pd foil (Merck). As mentioned in 3.2.1.1, we employed an ionic gating setup shown in Figure 3.1.1 to intercalate hydrogen ions into Palladium samples and induce electron doping.

Figure 4.1.3 and Figure 4.1.4 show the resistivity ρ of two representative Pd samples during the gating process at room temperature. These measurements allow us to control the H loading in our samples. The measurements were performed *in situ* using the standard four-wire method. We applied a constant current I_{DS} ranging from 0.1 to 1 mA, flowing between the drain (D) and source (S) contacts. Moreover, using the longitudinal voltage drop V_{xx} between the inner voltage contacts acquired by a multimeter, the resistivity was then deduced from the Eq. 3.1, where t and w are the sample thickness and width, and l_c (approximately 0.68 mm) is the distance between the inner voltage contacts. In particular, Figure 4.1.3 presents the measurements executed by applying a V_G up to 3 V, while Figure 4.1.4 shows a gating ramp up to 3.5 V. Comparing the two resistivity graphs, it is possible to notice a similar behaviour.

As shown in Figure 4.1.3, at $V_G = 0$ (region 1), a finite ρ of 14 $\mu\Omega$ cm is measured due to the electron-phonon scattering, as we are going to demonstrate with temperature-dependent resistivity measurements. Increasing V_G (region 2) from 0 to 3 V, at first ρ increases up to 18 $\mu\Omega$ cm and then remains mostly constant, oscillating from 16 to 20 $\mu\Omega$ cm. After the gating ramp (region 3), we kept fixed V_G at 3 V for more than 20 minutes, and we observed that the resistivity showed an increasing behaviour reaching 26 $\mu\Omega$ cm. The difference between the value reached at the end of the measurement ($\rho \sim 26$ $\mu\Omega$ cm) and the one at the beginning of region 2 (~ 14 $\mu\Omega$ cm) is about 12 $\mu\Omega$ cm. In a relative sense,

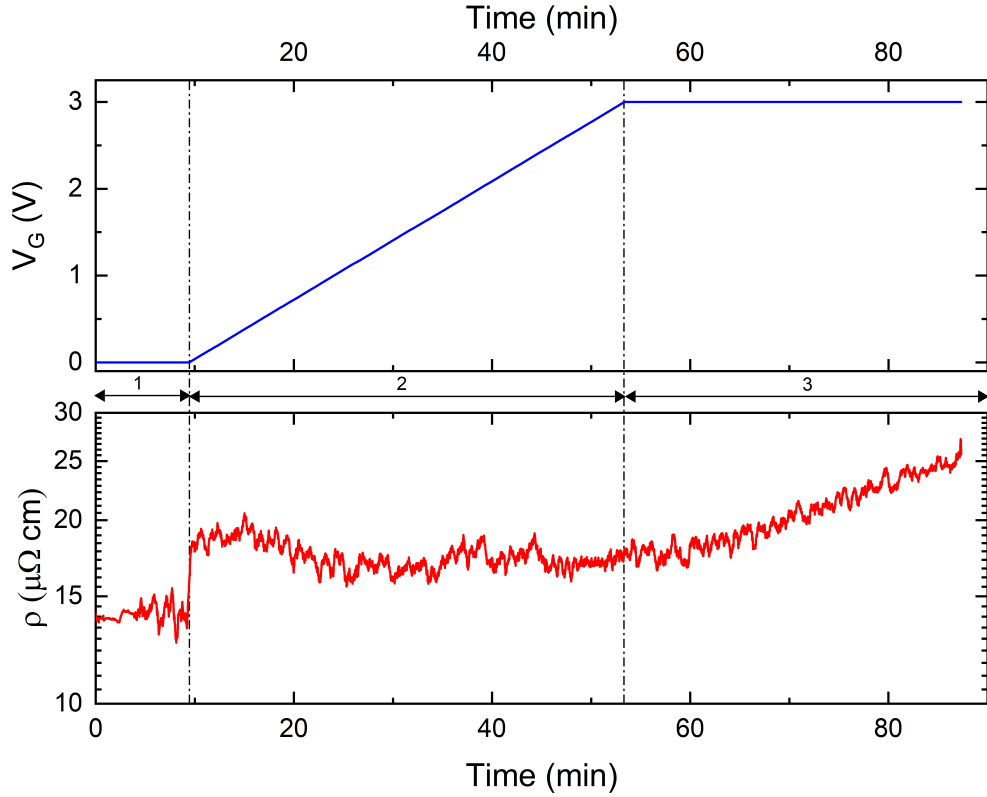


Figure 4.1.3: Gate voltage (upper panel - solid blue line) and resistivity (lower panel - solid red line) measured *in situ* as a function of time during a gating process.

this is an increase of about 85%. However, if considered in absolute terms, the variation is modest and observed in a relatively short time (~ 85 minutes). In addition, the overall trend of the curve suggests that saturation is not reached in these measurement conditions, and it is possible to implant more ions into the material's lattice.

For these reasons, we performed a second measurement (Figure 4.1.4). As before, at $V_G = 0$ (region 1), a finite ρ of $20 \mu\Omega \text{ cm}$ is measured. Then, we proceeded to increase V_G from 0 up to 3.5 V. Here (region 2) ρ remains substantially unchanged as long as $V_G < 2.75$ V. In the V_G range between 2.75 and 3.5 V, it is possible to observe a rapid increase reaching the value of $29 \mu\Omega \text{ cm}$. After the gating ramp (region 3), we kept fixed overnight V_G at 3.5 V. In this region, we observed that the resistivity shows an increasing behaviour reaching $34.8 \mu\Omega \text{ cm}$. However, the resistivity saturates approximately in 30 min (region 3) to $\rho \sim 31.8 \mu\Omega \text{ cm}$ and shows no further changes.

Notably, this saturation of resistivity at ambient temperature for overnight gat-

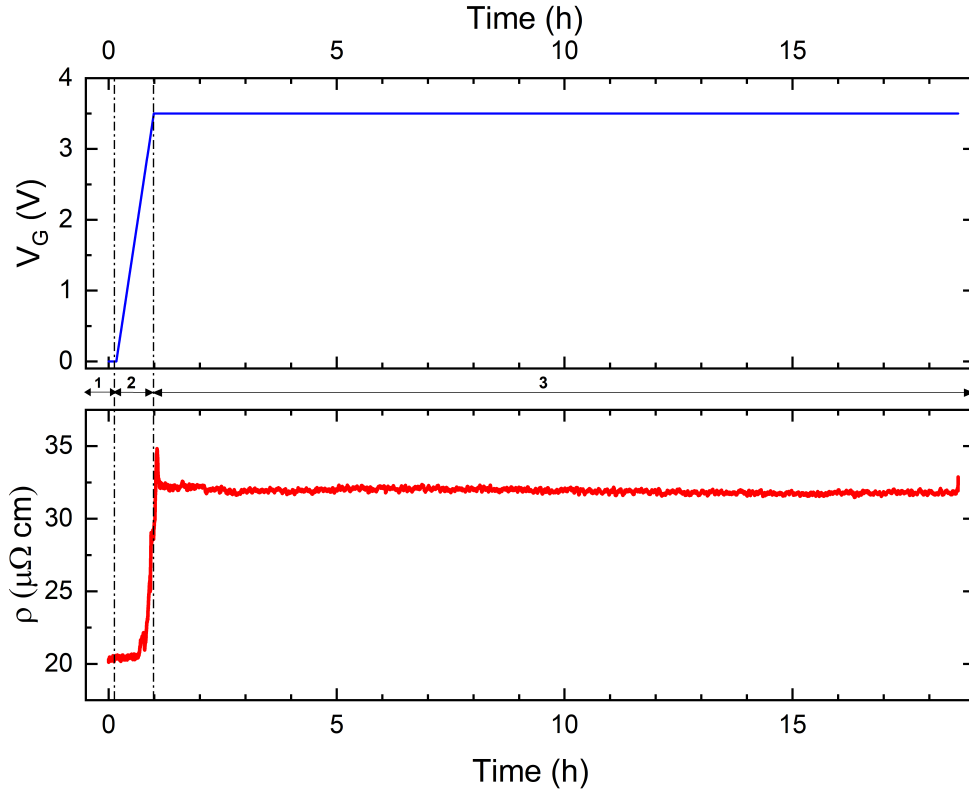


Figure 4.1.4: Gate voltage (upper panel - solid blue line) and resistivity (lower panel - solid red line) measured *in situ* as a function of time during a gating process.

ing suggests that most of the H dopants are driven into the sample in less than one hour, and further increasing the gating time does not alter the stoichiometry considerably. The process of electric-field-driven ion intercalation justifies this behaviour. Indeed, when a gate voltage is applied, the resistivity rapidly increases. Due to the intense electric field, H^+ ions are introduced into the lattice. Most likely, the intercalation process starts with a high concentration on the sample surface. As time passes, the diffusion process would likely start to dominate, and the dopants would penetrate the bulk region of the material. This way, after a reasonably long time (in Figure 4.1.4 approximately 30 min), the material's electrical properties reach saturation. This condition results from diffusive processes that determine a more stoichiometrically homogeneous composition.

4.1.1.2 Resistivity measurements

The electrical resistivity of a pure metal, such as Palladium, is approximately equal to the sum of a thermal resistivity (ρ_T) and a residual resistivity component (ρ_r), as described by the Matthiessen's rule:

$$\rho_{tot}(T) = \rho_T(T) + \rho_r \quad (4.2)$$

More specifically, ρ_T depends on the vibrations of the positive ionic nuclei around their equilibrium positions in the metal's crystal lattice. As the temperature increases, the vibration frequency of the nuclei increases and the phonons cause the conduction electrons to scatter, decreasing the mean free paths and relaxation times between collisions. Thus, an increase in temperature results in an increase in the electrical resistivity of pure metals. In contrast, the residual component is usually smaller than the previous one and depends on the presence of structural imperfections (dislocations, grain boundaries and impurity atoms) that cause elastic electron scattering. ρ_r is independent of temperature and typically is only significant at low temperatures, as shown in Figure 4.1.5 with the solid blue line. For most metals, at temperatures above about 75 K, electrical resistivity varies almost linearly with temperature [89].

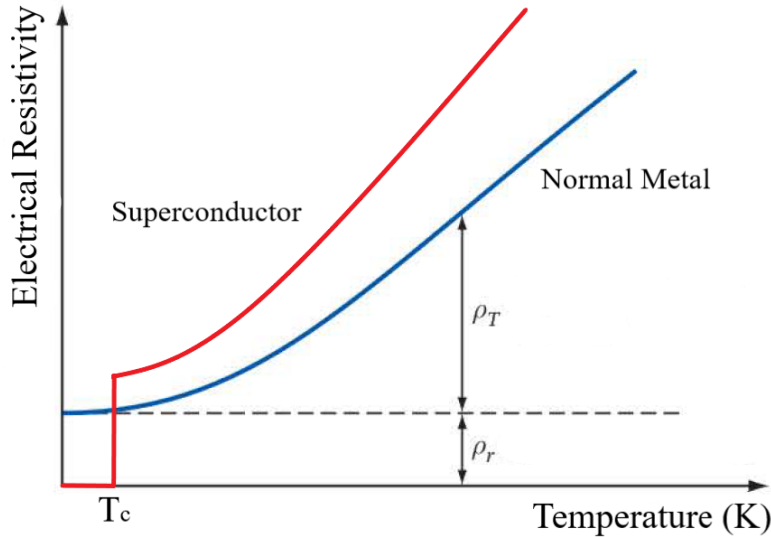


Figure 4.1.5: Schematic variation of the electrical resistivity of a normal metal (solid blue line) and a superconductor (solid red line) with absolute temperature. At high temperatures, the electrical resistivity of a normal metal is the sum of a residual component ρ_r and a thermal component ρ_T . Adapted from [89].

In contrast, the solid red line in Figure 4.1.5 shows the behaviour of a superconducting material. Here, as the temperature falls below a critical temperature (T_C) the material undergoes a phase transition. Under this temperature value, the resistivity drops abruptly to zero, determining that a DC electric current can circulate inside the material without any dissipation of energy [90].

In the following paragraphs, we report the results of our measurements of electric transport properties as a function of temperature T both in *ex situ* and *in situ*.

Figure 4.1.6 shows the T-dependence of ρ of different Pd samples protonated in different conditions.

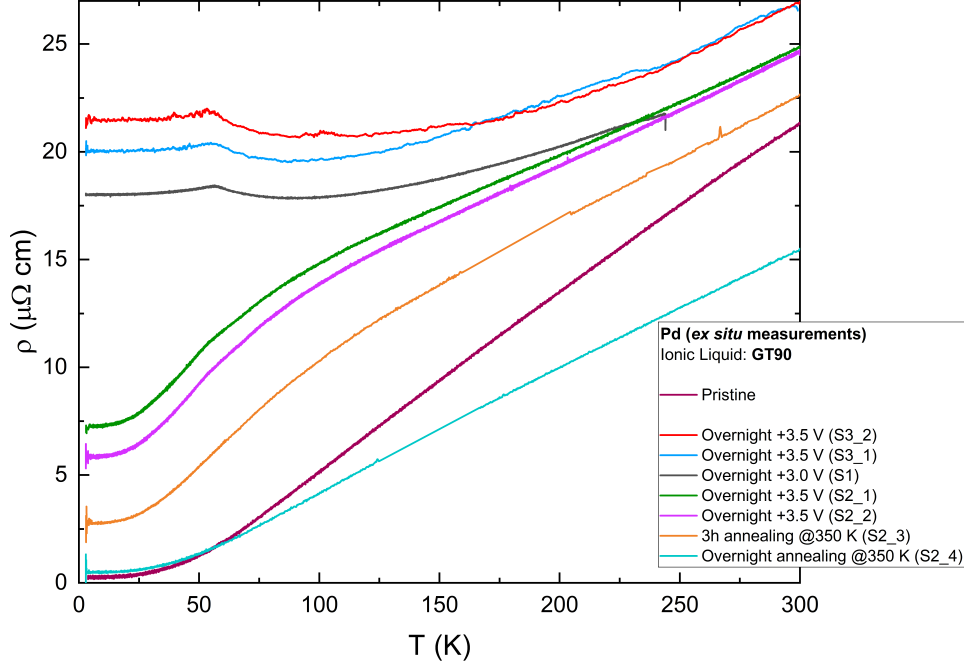


Figure 4.1.6: *Ex situ* resistivity (ρ) measurements in function of the temperature (T) for representative samples of Pd after the electric-field-driven ion intercalation using the GT90 IL, in different gating conditions.

Starting the description from the pristine material (solid dark purple line), the trend is substantially equivalent to the one shown in Figure 4.1.5 with a very small ρ_r due to the low defectiveness of the sample.

Sample 1 (S1) was protonated overnight at 3.0 V. It shows a behaviour coherent with the hydrogen intercalation. In fact, ranging from ~ 2.9 to 56 K, it is possible to observe a higher resistivity value (around $18 \mu\Omega \text{ cm}$) mostly constant in this range. That is in accordance with the presence of the hydrogen ions that act as impurities inside the lattice, contributing to an increase of ρ_r . The inflexion at about 60 K confirms the anomaly observed in literature [72].

Sample 3 (S3) curves show the same behaviour. Unlike S1, we performed the electric-field-driven ion intercalation by applying a higher V_G equal to 3.5 V overnight (Figure 4.1.4). Therefore, S3 shows a ρ_r which is higher than the one presented by S1, demonstrating that higher voltages, namely higher electric fields, can implant more hydrogen ions. We heated S3 the first time (solid blue line, S3_1); then, we cooled down the sample to 2.9 K and performed a second warm-up to 300 K (solid red line, S3_2). One can observe that the two curves share

the same trend with a slight difference at low temperatures ($T < 175$ K). That probably depends on the metal dislocation recombinations due to the cooling and the reheating processes that alter the intrinsic component of the resistivity. For $T > 175$ K, the thermal resistivity component is more relevant than the residual one, and the curves assume almost the same behaviour.

Sample 2 (S2) was ion intercalated in the same conditions of S3 ($V_G = 3.5$ V overnight). Like S3, we carried out two cycles of cooling down - heating up, as shown in S2_1 and S2_2 (solid green and purple lines, respectively). Here, the T-dependence is quite monotonic; therefore, we can deduce that the ρ_r component is lower than for S1 and S3. The anomaly, observed in the form of a hump between 25 and 75 K in S1 and S3, does not appear for S2. Indeed, we executed these measurements after the protonated sample was held under the infrared lamp for about 1 hour to cure the silver glue contacts. We can observe that S2 presents an intrinsic resistivity component lower than S3. We can explain this difference via the "unintentional" annealing at about 350-360°C for about 1 hour during the curing process. This treatment produced a partial de-intercalation of H^+ ions fully compatible with the more intense de-intercalation operated later, through an annealing process, on the same sample S2 that originated S2₃.

We observed, also in this case, a slight difference between S2_1 and S2_2. To verify whether this effect is due to the recombination phenomena inside the material or the loss of hydrogen due to the heating process, we decided to anneal the material at 350 K in a two-step procedure: 3 hours (solid orange line, S2_3) and overnight (solid turquoise line, S2_4). S2_3 shows the same trend of S2_1 and S2_2 but with an additional decrease of the residual resistivity component (vertical shift). Increasing the annealing time (S2_4) the residual component tends to be comparable to the pristine one, meaning that a massive amount of hydrogen ions has left the lattice. After 60 K, the curve appears monotonic and linear, with a lower growth rate than the pristine one. It is associated with the thermal resistivity component ρ_T , that for pure metal is given by

$$\rho_T = \rho_{273K}(1 + \alpha_T \times T) \quad (4.3)$$

where ρ_{273K} is different for each sample due to the different stoichiometry in the Pd-H system.

The previous analysis was performed *ex situ*, i.e. after extracting the intercalated Pd samples from the cell and rinsing them using acetone and ethanol to remove ionic-liquid residues. In order to avoid eventual hydrogen ions loss from the lattice due to their volatility during these phases, we decided to characterize the electrical transport properties directly *in situ*, namely inside the cryocooler. These results are presented in Figure 4.1.7.

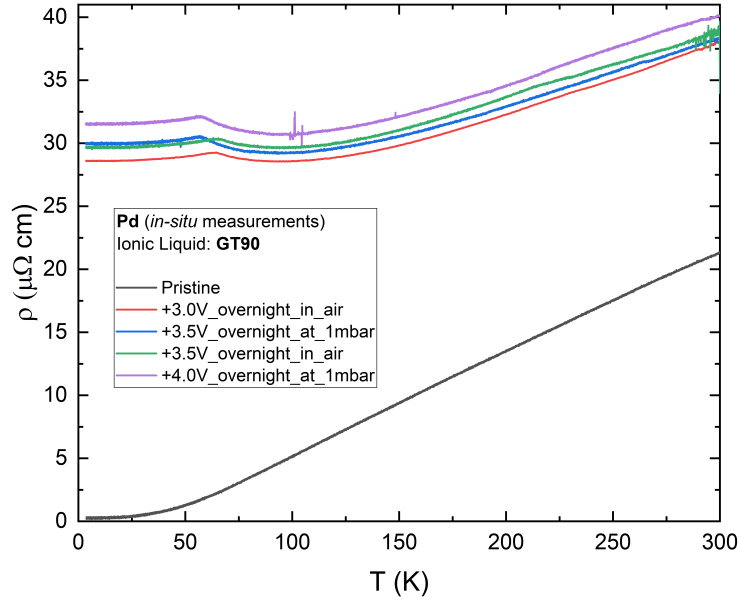


Figure 4.1.7: *In situ* resistivity (ρ) measurements in function of the temperature (T) for representative samples of Pd after the electric-field-driven ion intercalation using the GT90 eutectic mixture, in different gating conditions.

Here, it is worth noting that the resistivity curves in the low-temperature regime at different protonation conditions present a higher residual resistivity component if compared with the *ex situ* analysis (Figure 4.1.6). Indeed, the resistivity values at low temperatures (below 79 K) shift upwards. Thus, we obtained a better control of hydrogen concentration. The overall trend is similar to the one already described for *ex situ* measurements at high doping. Studying the areas under the region of the curves associated with the anomalies allows us to get more detailed information about the difference in hydrogen concentration. Firstly, we normalized the resistivity curves to the values of the pristine sample resistivity at 4.2 K, both in the *ex situ* and *in situ* characterization. These normalized curves are shown in Figure 4.1.8 and Figure 4.1.9, respectively.

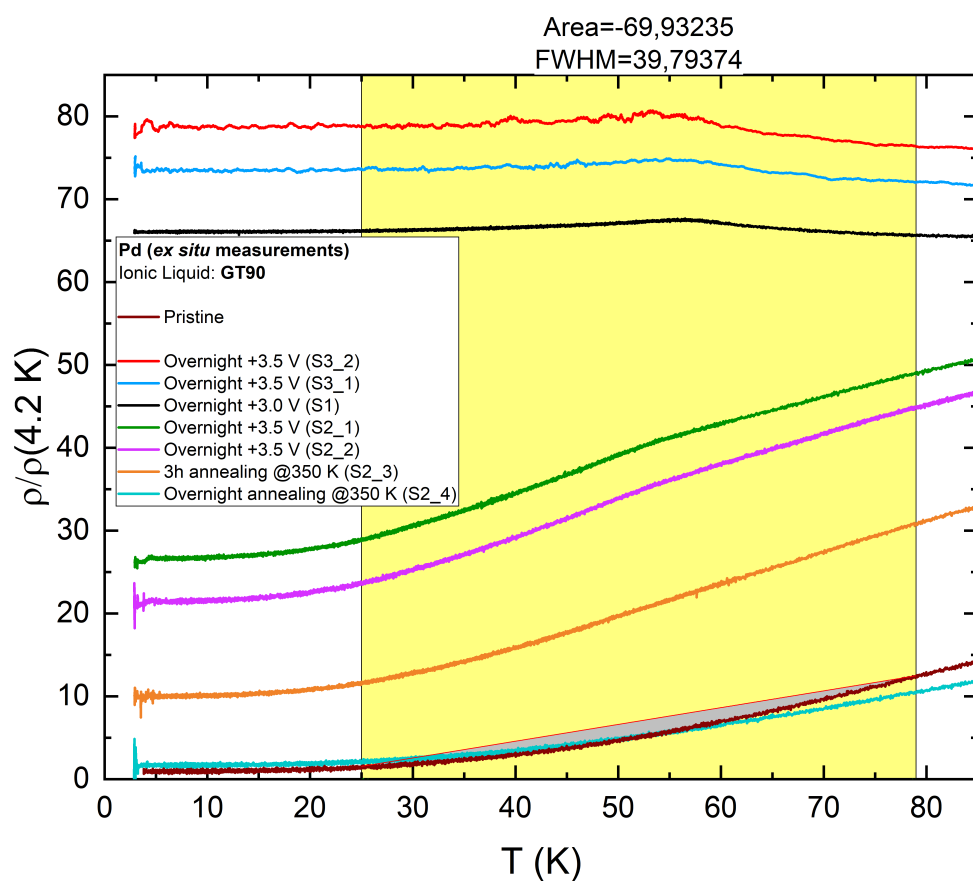


Figure 4.1.8: *Ex situ* resistivity measurements normalized at the value of the pure Pd at 4.2 K ($\rho/\rho(4.2K)$) in function of the temperature (T) for representative samples of Pd after the electric-field-driven ion intercalation using the GT90 eutectic mixture, in different gating conditions. The yellow background highlights the integration area under investigation.

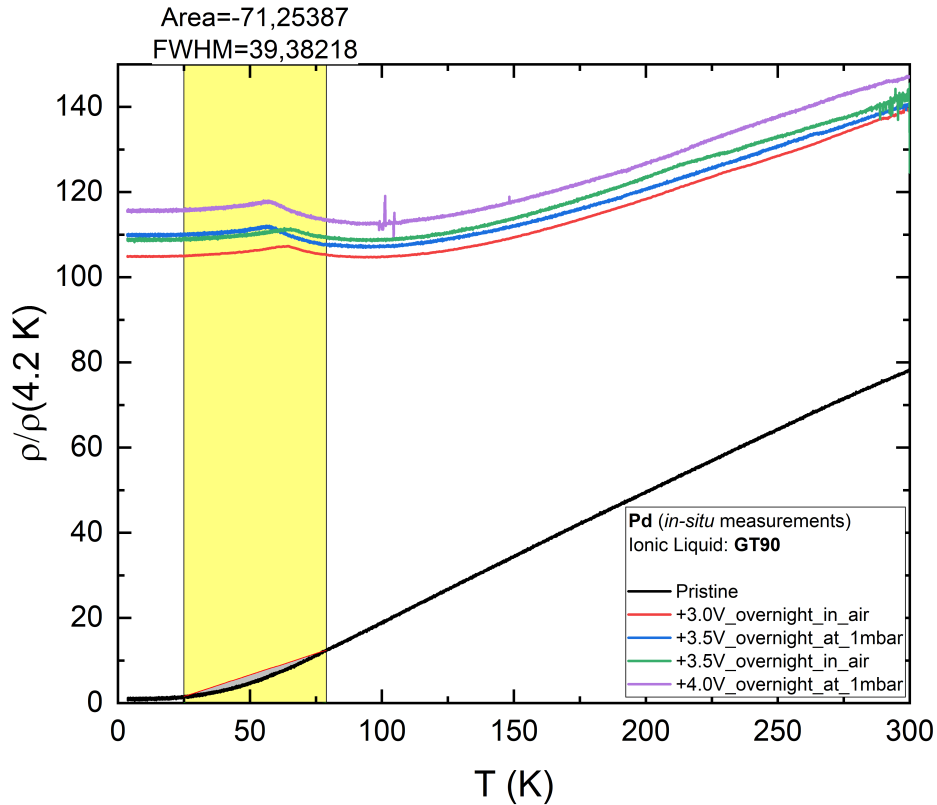


Figure 4.1.9: *In situ* resistivity measurements normalized at the value of the pure Pd at 4.2 K ($\rho/\rho(4.2K)$) in function of the temperature (T) for representative samples of Pd after the electric-field-driven ion intercalation using the GT90 eutectic mixture, in different gating conditions. The yellow background highlights the integration area under investigation.

Exploiting the integration tool of "Origin" software, we calculated the areas subtended by the portion of the curves indicated by the yellow region with respect to the area under the straight line joining the extremes of the curves in the same region (illustrated in figures Figure 4.1.8 and Figure 4.1.9, respectively) and several other parameters, such as the X and Y coordinates associated with the maximum humps, as reported in Tables 4.1 and 4.2, respectively. In these tables, some area values are negative. That depends on the concavity of the curves in the considered temperature range of integration, namely between 25 and 79 K.

Dataset Identifier	Beginning X	Ending X	Max Height	X at YMax	Mathematical Area	Area Above Baseline	Area Below Baseline
$\rho/\rho(4.2\text{ K})$							
Pristine	25	79	-2,22184	53,19195	-71,25387	1,86749E-4	71,25406
Overnight +3.0 V (S1)	25	79	1,78288	56,5082	35,63231	35,69529	0,06298
Overnight +3.5 V (S2_1)	25	79	1,43205	53,6237	23,5834	25,64627	2,06287
Overnight +3.5 V (S2_2)	25	79	0,96537	59,0025	9,84173	14,43199	4,59026
3h annealing @350 K (S2_3)	25	79	-1,46605	42,153	-32,35014	0,51454	32,86468
Overnight annealing @350 K (S2_4)	25	79	-1,5089	50,9472	-42,00572	0,0589	42,06462
Overnight +3.5 V (S3_1)	25	79	2,12846	54,921	42,78925	42,97621	0,18696
Overnight +3.5 V (S3_2)	25	79	3,18796	53,3654	60,74537	60,80066	0,05529

Table 4.1: Data acquired through the integration of the resistivity curves of the *ex situ* measurements of Figure 4.1.8 between 25 and 79 K.

Dataset Identifier	Beginning X	Ending X	Max Height	X at YMax	Mathematical Area	Area Above Baseline	Area Below Baseline
$\rho/\rho(4.2\text{ K})$							
Pristine	25	79	-2,22184	53,19195	-71,25387	1,86749E-4	71,25406
+3.0V_overnight_in_air	25	79	2,11451	64,583	47,96743	47,96743	0
+3.5V_overnight_at_1mbar	25	79	3,45472	57,3981	71,15531	71,2579	0,10259
+3.5V_overnight_in_air	25	79	2,23156	63,0312	41,39889	41,63542	0,23653
+4.0V_overnight_at_1mbar	25	79	3,49111	55,1422	73,36863	73,64293	0,2743

Table 4.2: Data acquired through the integration of the resistivity curves of the *in situ* measurements of Figure 4.1.9 between 25 and 79 K.

From these comparisons, it emerges that the absolute values of the areas are generally lower for the *ex situ* measurements than for the *in situ* ones, confirming that a hydrogen ions loss occurs during the phases of cleaning and mounting into the cryocooler.

In order to evaluate the accuracy of the electric-field-driven ion intercalation, we compared our *in situ* characterization results with the work of Skoskiewicz and Baranowski [72]. To insert hydrogen into the Pd lattice, they put a metallic palladium foil (30 μm of thickness) in gaseous hydrogen of about 10000 atm at room temperature. After cooling the temperature to about $-30\text{ }^\circ\text{C}$ (243 K) and reducing the hydrogen pressure, they extracted the sample from the equipment. They measured the electrical resistance of such samples between 4.2 and 80 K, gradually lowering the amount of hydrogen in samples. Therefore, they evaluated the amounts of desorbed gas via mass-spectrometry analysis. They obtained results reported in the Figure 4.1.10 in panels (a) and (b). We digitalized these curves with the "Origin" software getting the curves plotted in panel (c) of the same figure.

Also in this case, to validate this hypothesis, we evaluated the areas under the curves between 25 and 79 K. The obtained parameters are collected in the following Table 4.3.

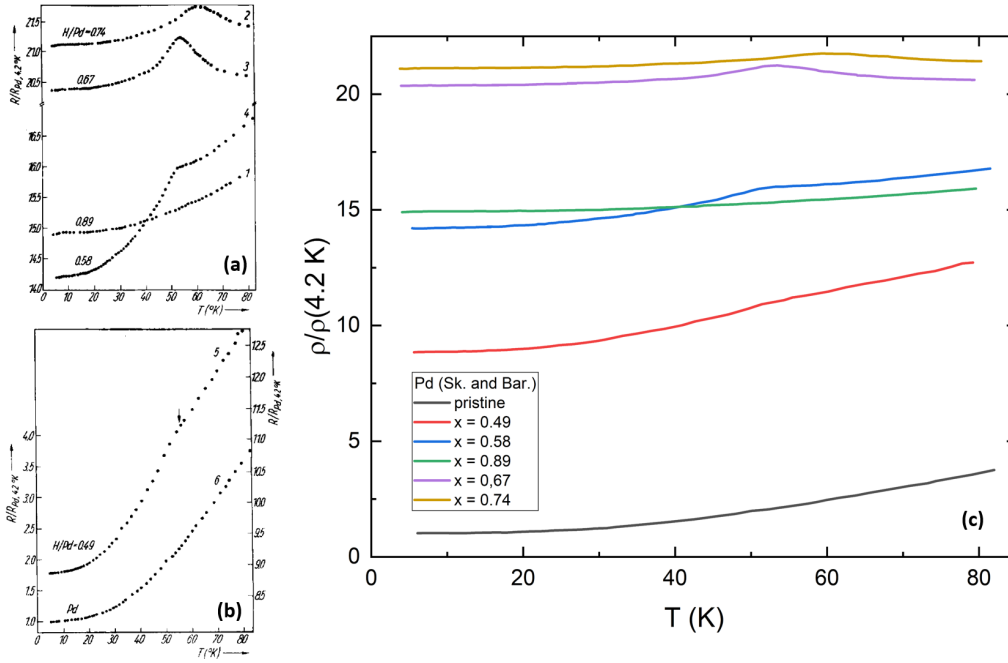


Figure 4.1.10: (a) and (b) represent the original graphs of the resistivity measurements normalized at the value of the pure Pd at 4.2 K from the literature [72]; (c) is our digital reconstruction of (a) and (b).

Dataset Identifier	Beginning X	Ending X	Max Height	X at YMax	Mathematical Area	Area Above Baseline	Area Below Baseline	
$\rho/\rho(4.2 \text{ K})$								
pristine		25	79	-0,31056	47,95124	-10,96044	0	10,96044
x = 0.49	0,49	25	79	-0,19464	38,58124	-3,22784	0,32217	3,55002
x = 0.58	0,58	25	79	0,37408	53,19077	5,32405	5,87938	0,55533
x = 0.67	0,67	25	79	0,70497	53,48585	13,37061	13,37061	0
x = 0.74	0,74	25	79	0,42083	59,26461	8,79644	8,81649	0,02005
x = 0.89	0,89	25	79	-0,14272	42,83818	-4,9795	0	4,9795

Table 4.3: Data acquired through the integration of the resistivity curves of the graph extracted from the literature [72] between 25 and 79 K.

We compared our resistivities, normalized against that of pure material at 4.2 K, with the ones presented in literature [72] normalized in the same conditions. In particular, considering the most resistive cases at low temperatures, Skoskiewicz et al. [72] get a resistivity growth from pure Pd to PdH_x of about 21 times, while we obtain a growth of about 80 (in *ex situ* measurements) and 110 (in *in situ* case), obtaining a difference factor of 4-5. Also, the trend of the pristine appears slightly different: this is probably due to the slight differences in composition between the two materials or to the impurities and defects' presence that affects ρ_r . This mismatch suggests that comparing the anomalies appearing in the range 25-79 K in terms of area or maximum height is not appropriate, and therefore a different comparative approach is necessary. In particular, we computed the first derivatives of resistivity normalized at 79 K in temperature ($\frac{d\rho}{dT}$) of all the curves, both ours (Figure 4.1.13) (*in situ*, considering the higher content of

H) and the ones extracted from the literature (Figure 4.1.11). The minimum of the first derivative gives evidence of the beginning of the anomaly. In this way, we can extract the onset temperature of the anomaly (if present). Plotting these values in function of the relative concentrations, we can eventually deduce a trend.

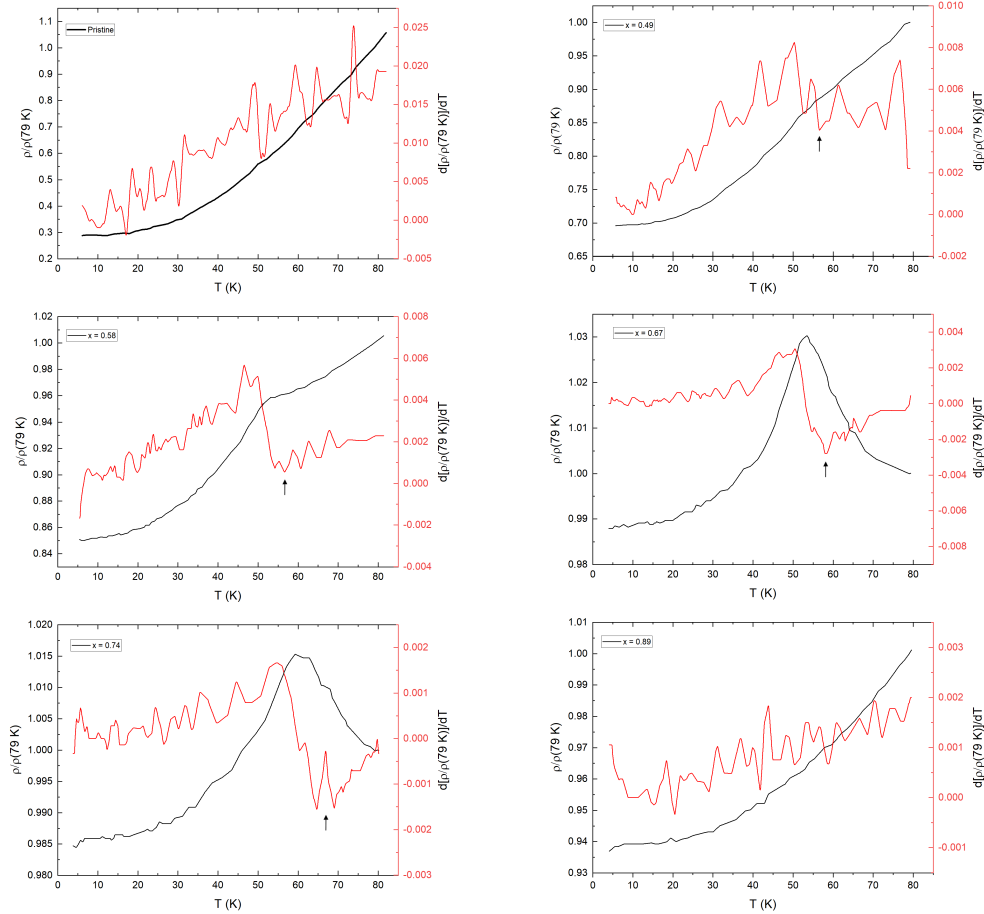


Figure 4.1.11: Solid red line indicates the first derivative of the resistivity normalized at 79 K (solid black line) in temperature for the different hydrogen concentration x extracted from [72]. The blue point indicates the onset temperature of the anomaly.

Starting from literature results, it is worth noticing that the curve with $x = 0.89$ and the pristine one do not present any anomaly and their first derivatives in temperature remain monotonic along all the considered domains. For the other concentration values, an onset point is present (black arrows in Figure 4.1.11). Considering these data, we plotted the onset temperatures of the anomalies, as reported in Figure 4.1.12. Here, a growing overall trend with respect to the $x = \text{H}/\text{Pd}$ concentration is present.

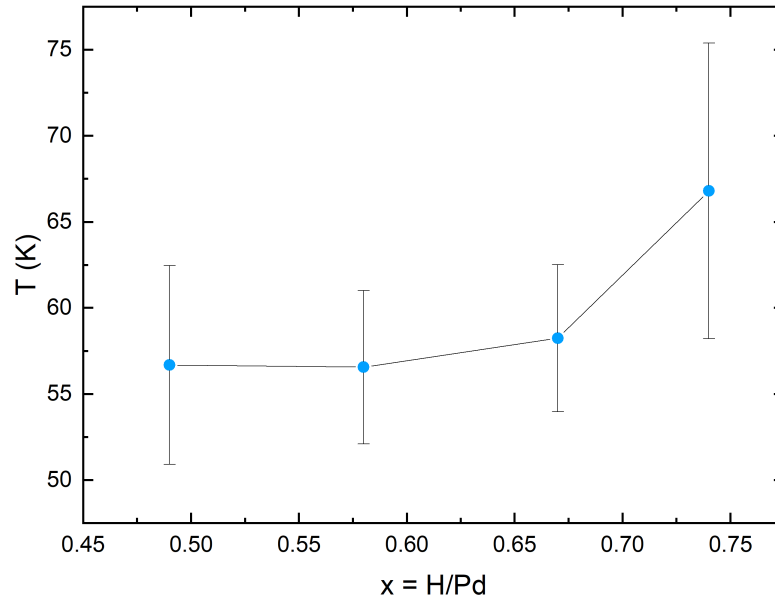


Figure 4.1.12: Onset temperature of the anomaly in function of the $x = \text{H/Pd}$ concentration, extrapolated from [72].

Applying the same approach to our curves, made under different gating conditions and at unknown hydrogen concentration, we can observe in Figure 4.1.13 that the first derivatives of all the samples, except the pristine, present an evident minimum (black arrows in Figure 4.1.13) that is found in the ranges between 60 and 70 K.

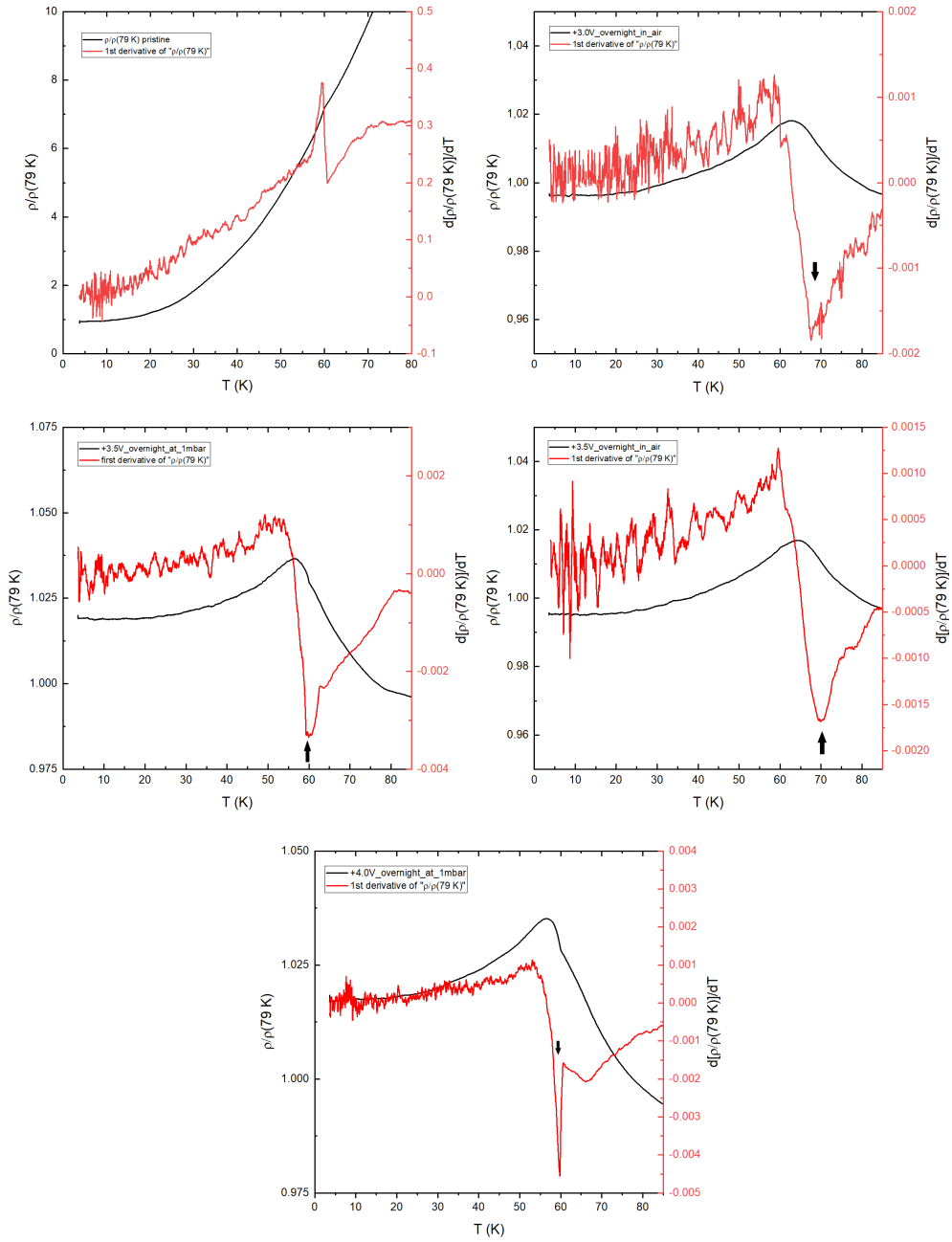


Figure 4.1.13: Solid red line indicates the first derivative of the resistivity normalized at 79 K (solid black line) in temperature for the different gating conditions.

Therefore, our results allow us to identify a range of onset temperatures of the anomalies, similar to the one we extracted from the literature [72]. These onset temperatures are collected in Figure 4.1.14 and shown in function of the gating conditions. Referring to Figure 4.1.12, the values obtained are compatible with a H/Pd ratio of around 0.74. This value is a hint of the concentrations induced by our technique. We would require mass spectroscopic analysis techniques to obtain exact quantitative information on the intercalated hydrogen concentration in our samples.

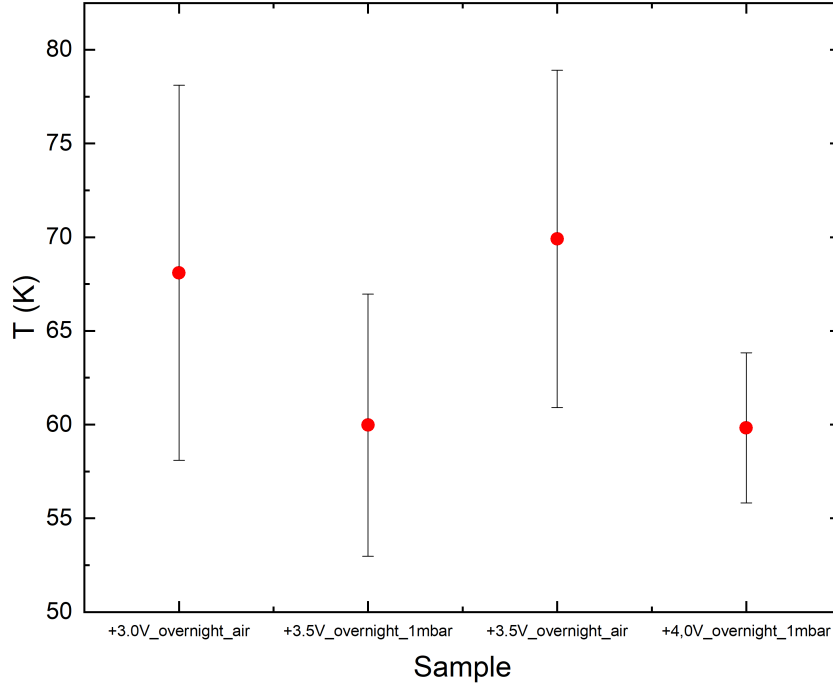


Figure 4.1.14: Onset temperature of the anomaly in function of the $x = \text{H/Pd}$ concentration in our *in situ* samples.

In conclusion, we can deduce that the hydrogen concentrations obtained in our samples are still low to induce an $\alpha \rightarrow \beta$ phase transition for the Pd-H system (Figure 4.1.2). Consequently, no superconducting phase transition phenomena could be observed, according to what was reported by [79]. He found that superconductive transition manifested for H/Pd ratios above 0.81 with a narrow transition region ($T_c=4.6$ K). For H/Pd=0.87 ($T_c=2.5$ K), the material presented a broad superconducting transition. Furthermore, it would be desirable to repeat the intercalation process and measure the transport properties using other gating conditions.

4.2 General description of Palladium-Copper Alloy

As seen in the previous paragraphs, the binary compound PdH presents superconductive transition at T_c approximately equal to 8-9 K and at ambient pressure. Here, superconductivity can be associated with the spin fluctuations suppression of the Pd by the H intercalation with a H/Pd ratio of about 0.7, where the system becomes diamagnetic. We can observe this diamagnetic behaviour also in Pd-alloys with metals, which share their electrons to the Pd [12, 91].

An alloy is a mixture of two or more metals or metallic elements and non-metallic elements. The simplest type of alloy is the solid solution, i.e. a solid consisting of two or more elements atomically dispersed in a single-phase structure. There are two types of solid solutions: substitutional and interstitial [89]. In particular:

- Substitutional solid solution: a solid solution in which the solute atoms of one element can replace the solvent atoms of another element;
- Interstitial solid solution: a solid solution in which solute atoms can enter the interstices or voids of the solvent atomic lattice.

Several studies have examined the effect of alloying with selected elements onto the electronic structure and the phonon spectrum of Pd to explore the effects on T_C in particular. Pd-alloys can be both interstitial and substitutional [9, 12].

Table 4.4 reports the effects on T_C of alloying Pd with nearby and more distant elements after using hydrogen implantation at low temperatures to achieve non-equilibrium H concentrations and find the concentration of an alloying element at which T_C is the maximum for that element.

Alloying element	Effect on T_c	Maximum T_c (K)
Al	Increases up to about 5 at.% Al	9.6
Ti	Decreases	8.8
Ni	Decreases <10 at.% Ni	10.2
Cu	Increases up to about 45 at.% Cu	17.0
Rh	Decreases	2.6
Ag	Increases up to about 30 at.% Ag	15.6
Pt	Almost constant up to about 25 at.% Pt, and then decreases	9.0
Au	Increases up to about 16 at.% Au	13.5

Table 4.4: Effect of substitutional alloying of Pd on superconducting transition temperatures. Adapted from [9].

Alloying Pd with the first neighbour elements in the periodic table (nickel, rhodium, silver (Ag) and platinum (Pt)) considerably decreases the solubility of hydrogen. Moreover, in the case of Pt, the maximum T_C remains almost constant up to about 25% Pt and then decreases. This trend suggests that the acoustic phonon spectrum of these hydrides has a strong effect on T_C . Indeed, Pd-noble metal alloys become diamagnetic at noble metal-concentration higher than 60 at.%.

In 1974 Stritzker *et. al* [12] analyzed ternary hydrides Pd-M-H where M represents noble metals, like Ag, gold (Au) and copper (Cu). The substitution with low concentrations of these metals results in unexpected superconductivity behaviour with a consistent increase of maximum T_C . They made their samples using arc-melting in ultrapure Argon and then precharged them with gaseous H_2 . The second step was the implantation with H-atoms at He-temperatures.

For what concern the PdCuH system, they precharged the PdCu alloy at the fixed composition ($Pd_{0.55}Cu_{0.45}$) with an H concentration equal to 0.04. In principle, this ternary system is not superconducting. Hence, they decided to perform further H implantation to trigger the superconductive transition. The effect caused on T_c by a variation in the concentration of H is reported in panel a of Figure 4.2.1. Here, we observe an increasing of T_c up to a H concentration value of around 15×10^{17} H-atoms/cm². For this latter concentration they reach maximum transition temperature equal to 17.1 K. Beyond this maximum, a slow decrease in the critical temperature occurs.

In addition, the trend of the transition temperature as a function of the Cu concentration in the PdCu system is reported in panel b of Figure 4.2.1. We can observe that concentrations up to 45 at.% of Cu in the Pd lattice cause the increase of T_C from around 9 K (comparable to the one of the Pd-H system) to around 16.6 K [9, 12]. The authors estimated that the H/Metal ratio at $T_c=16.6$ K is approximately 0.7. After the maximum reached at 0.45% at of Cu, the T_c trend tends to slowly decrease.

In order to maintain this optimal H/metal ratio, which allows us to get the maximum T_c , the sum of H and Cu concentrations should remain almost constant according to the assumption that the main requirement for the superconductivity is the suppression of the spin fluctuations. Indeed, the additional H-atoms and the substitutional Cu-atoms reduce the strong paramagnetism of the Pd in the same way. However, this single mechanism cannot justify the induction of the superconducting phase. Therefore, another mechanism linked to the concentration of hydrogen alone must exist. This could be related to a strong electron-phonon interaction determined by the weak phonon modes, which sometimes leads to phase transitions in Pd-Cu-H alloys with high T_c -values. [12]. Furthermore, the enormous difference in pressure between these ternary systems and the high- T_c hydrides (e.g. SH_3 , LaH_{10} , C-S-H with T_c higher than 200 K and pressure around 200 GPa) suggests a different role for hydrogen, which is not able to metallize at pressures below 400 GPa [8, 91].

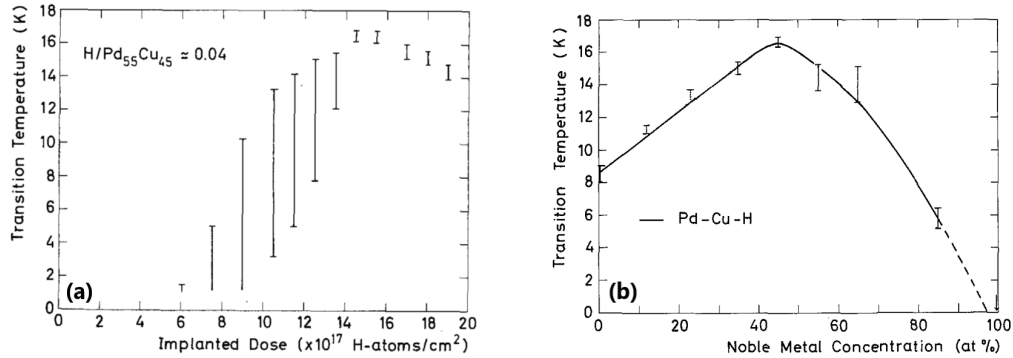


Figure 4.2.1: (a) Transition Temperature (T_c) versus implanted H-dose of a H/Pd_{0.55}Cu_{0.45} \sim 0.04 alloy. (b) Maximum T_c -value vs Cu concentration in the ternary hydride PdCuH_x. Adapted from [12]

To corroborate the experimental results described in the previous paragraphs, Vocaturo and coworkers [91] recently carried out a theoretical study to explore the structural, electronic, dynamical, and superconducting properties of the PdCuH_x ($x=1,2$) at ambient pressure via first-principles, density functional theory (DFT) to understand the microscopic origin of the H-induced superconducting phase. They also calculated the most stable sites for interstitial hydrogen, defined as O1, O2 (octahedral sites) and T (tetrahedral), as shown in Figure 4.2.2.

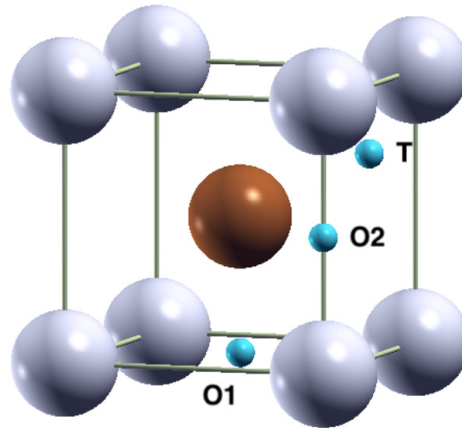


Figure 4.2.2: Unit cell of the PdCu in the B2-phase. Gray (brown) spheres represent Pd (Cu) atoms. In the unit cell, the high symmetry intercalation sites of H are indicated with blue points. From [91]

Similarly to Stritzker's samples, they first considered the PdCu alloy at equal concentrations of Pd and Cu. As reported in the phase diagram in Figure 4.2.3, the system is in the *mixed*-phase at this stoichiometry.

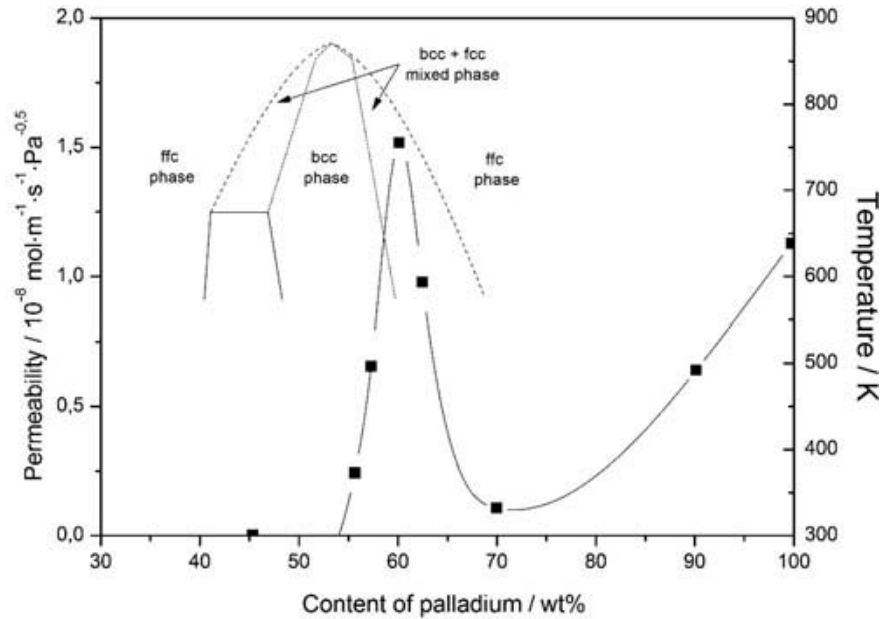


Figure 4.2.3: Hydrogen permeability as a function of palladium wt% at 623 K and phase diagram of Pd-Cu alloys. From [92]

Namely, it crystallizes in a disordered FCC-structure mixed with an ordered BCC-structure, also known as the CsCl phase or B2-phase. Previous literature cited by Vocaturo *at al.* suggests that the superconductivity origin is related to the ordering of the crystal. They discarded FCC because of its spontaneous disorder and focused on the ordered B2 phase to search for superconductivity. In the same article, they also compared the band structure of pure palladium with that of the PdCu and found that Cu atoms expand the Fermi surface, acting as electron dopants in the system. H also acts as an electron dopant shifting the Fermi levels to higher energies, according to what happens in PdH in which hydrogen reduces the density of state at the Fermi level.

They identified the low-hydrogen content phase as the PdCuH ($x=1$) hydride, predicting the octahedral “O1” site (Fig. 1) as the low-energy intercalation site for hydrogen, in good agreement with available experimental data. However, the low electron-phonon coupling parameter excludes this structure as responsible for the observed T_C in Pd-M-H mentioned above. Indeed, the DFT calculation showed a T_C lower than 1K, configuring this system as a sub-kelvin superconductor. They used Allen and Dynes equation to calculate the transition temperature T_C :

$$T_C = \frac{\omega_{log}}{1.2} \exp - \frac{1.04(1 + \lambda)}{\lambda - \mu^*(1 + 0.62\lambda)} \quad (4.4)$$

where λ represents the electron-phonon coupling constant, ω_{log} is the logarithmic average of the phonon frequency. These two values are obtained from the electron-phonon coupling function ($\alpha^2F(\omega)$). μ^* indicates the Coulomb repulsion

between electrons, and it was fixed to 0.1 since it results in good agreement with the behaviour of a large class of materials [91].

On the other hand, considering that the optimal H /M ratio found by Stritzker was approximately 0.7 [12], we need to consider stoichiometry around PdCuH_{~1.4}. For this reason, Vocaturo and collaborators [91] decided to investigate the PdCuH₂, i.e., the highly hydrogenated structure. In this latter case, the hydrogen occupies both the O1 and O2 sites, differently from the case with x=1. This phase has interesting superconducting properties, with an estimated T_c of 34 K, according to Eq. 4.4. This value appears to be almost twice the one found experimentally by Stritzker [12]. This difference can be associated with the anharmonic effects, which, strengthening (i.e. hardening) the phonon frequencies, reduce the critical temperature predicted within the harmonic approximation. They also analyzed the metastable phase in which hydrogen resides in the T sites.

In our work, we decided to analyse the Pd_{0.6}Cu_{0.4} alloy in order to verify if we are able to insert via our technique the right H concentration to reach a similar maximum T_c [92].

Recalling the Figure 4.2.3 and the considerations made by Vocaturo [91] reported in the previous paragraphs, we can observe that at a composition of 60wt.% of Pd and 40 wt.% of Cu the BCC phase has the highest hydrogen permeability of the Pd-Cu alloy system. These high permeability values depend on the higher mobility of hydrogen atoms within the BCC crystal structure of the Pd-Cu alloy compared to the FCC continuous solid solution [93]. It is worth noting that the hydrogen diffusion in the BCC phase is two orders of magnitude higher than the FCC one, while solubility in BCC is lower than the previous one. However, the hydrogen permeability is higher in BCC-PdCu. That depends on the lower compactness of the BCC structure compared to the FCC one. Indeed, as shown in Figure 4.2.4, in the BCC lattice structure, atoms are very close to each other along the diagonal directions. This structure presents a higher number of interstitial sites compared to the FCC crystal structure, namely 18 octahedral interstitial sites (along the corners and in the face centres) and 24 tetrahedral interstitial sites [89].

Moreover, dissolved hydrogen shifts the stability range of the BCC and mixed BCC-FCC phase regions to slightly higher palladium concentrations. In any case, the maximum stability temperature for any BCC phase is about 873 K, as reported in [93].

Considering the importance of the crystalline structure in inducing the superconductivity, we also performed X-ray diffraction and magnetic susceptibility analysis in order to verify if the theoretical prediction fit with the experimental results.

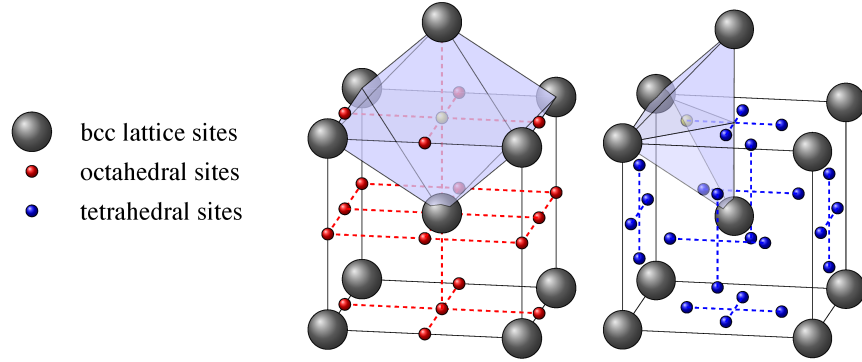


Figure 4.2.4: Elementary bcc lattice cell showing octahedral (red spheres) and tetrahedral (blue spheres) interstitial sites.

4.2.1 Results and discussion

4.2.1.1 Electric-Field-Driven Ion Intercalation

Palladium-Copper Alloy samples (typical size approx. $2 \text{ mm} \times 0.75 \text{ mm} \times 25 \text{ }\mu\text{m}$) with a stoichiometry composition $\text{Pd}_{0.6}\text{Cu}_{0.4}$ foil were obtained by cutting a commercial $\text{Pd}_{0.6}\text{Cu}_{0.4}$ foil (Merck). As discussed for the Pd samples in the previous paragraphs 4.1.1.1, we employed an ionic gating setup to intercalate hydrogen ions into $\text{Pd}_{0.6}\text{Cu}_{0.4}$ -Alloy samples and induce electron doping.

Figure 4.2.5 and Figure 4.2.6 show the resistivity ρ of two representative $\text{Pd}_{0.6}\text{Cu}_{0.4}$ -Alloy samples during the gating process at room temperature. In particular, in Figure 4.2.5 are shown the measurements executed by applying a V_G up to 3 V, while Figure 4.2.6 shows a gating ramp up to 3.5V. Comparing the two resistivity graphs, it is possible to notice a different trend, probably related to the nature of the ILs employed. In particular, the measurements were performed *in situ* using the standard four-wire method. We applied a constant current I_{DS} ranging between 1 and 10 mA, flowing between the D and S contacts. As usual, using the longitudinal voltage drop V_{xx} between the inner voltage contacts acquired by a multimeter, the resistivity was then deduced from Eq. (3.1), where in these cases the channel length l_c were approximately 0.5 mm.

As displayed in Figure 4.2.5, at $V_G = 0$ (region 1), a finite ρ of around $90 \text{ }\mu\Omega \text{ cm}$ is measured. Probably, that is due to the intrinsic impurities of the metal, as will be confirmed by the temperature-dependent resistivity measurements discussed in the next Section. Increasing V_G (region 2) instantaneously from 0 to 2.5 V, at first ρ increases up to $92 \text{ }\mu\Omega \text{ cm}$ and then decreases quite rapidly to the initial value. Then, we proceeded by performing a gate ramp up to 3 V. Here (initial part of region 3), we can observe an additional increase of the resistivity up to $91 \text{ }\mu\Omega \text{ cm}$. After this latter gating ramp, we kept fixed V_G at 3 V overnight, and we observed that the resistivity showed a decreasing behaviour reaching $89 \text{ }\mu\Omega \text{ cm}$. The difference between the value reached at the end of the measurement

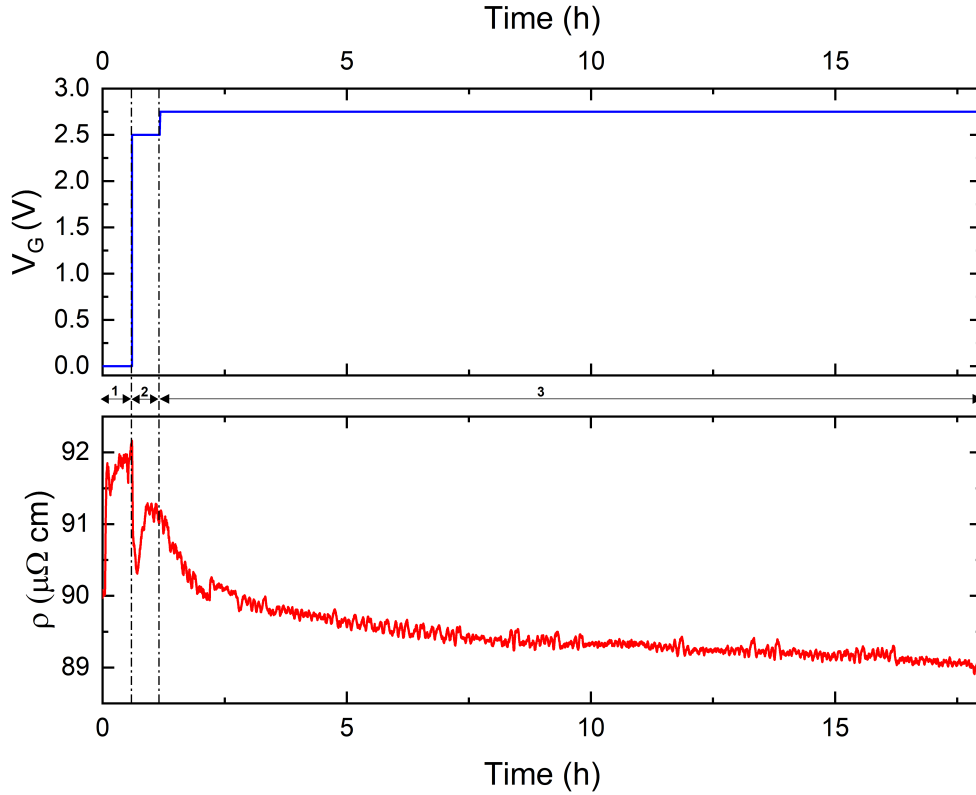


Figure 4.2.5: Gate voltage (upper panel - solid blue line) and resistivity (lower panel - solid red line) measured *in situ* as a function of time during a gating process. In this case the electric-field-driven ion intercalation was performed using the EMIM-BF₄ ionic liquid.

($\rho \sim 89 \mu\Omega \text{ cm}$) and the one at the beginning of region 2 ($\sim 92 \mu\Omega \text{ cm}$) is about $3 \mu\Omega \text{ cm}$. In a relative sense, this is a decrease of about 4%. This variation is quite negligible. However, the overall trend of the curve suggests that saturation is reached in these measurement conditions, and it is not possible to implant more ions into the material's lattice. To perform these measurements we used several times the EMIM-BF₄ IL. Probably, exploiting only the water traces dissolved in EMIM-BF₄ IL provides a limited reservoir of H⁺ ions.

For these reasons, we decided to perform a second batch of measurement using the GT90 eutectic mixture, which acts itself as a source of H⁺ ions due to the breaking of the glycerol molecules during the gating process which produces a release of H⁺ ions. One of these representative analyses is shown in (Figure 4.2.6). As before, at $V_G = 0$ (region 1), a finite ρ of $30 \mu\Omega \text{ cm}$ is measured. Then, we proceeded to increase V_G from 0 up to 3.5 V. Here (region 2) ρ remains substantially unchanged as long as $V_G < 1.7 \text{ V}$. In the V_G range between 1.7 and 3.5 V, it is possible to observe first a slightly decrease and then an additional increase reaching the initial value. After the gating ramp (region 3), we kept fixed overnight V_G at 3.5 V. In

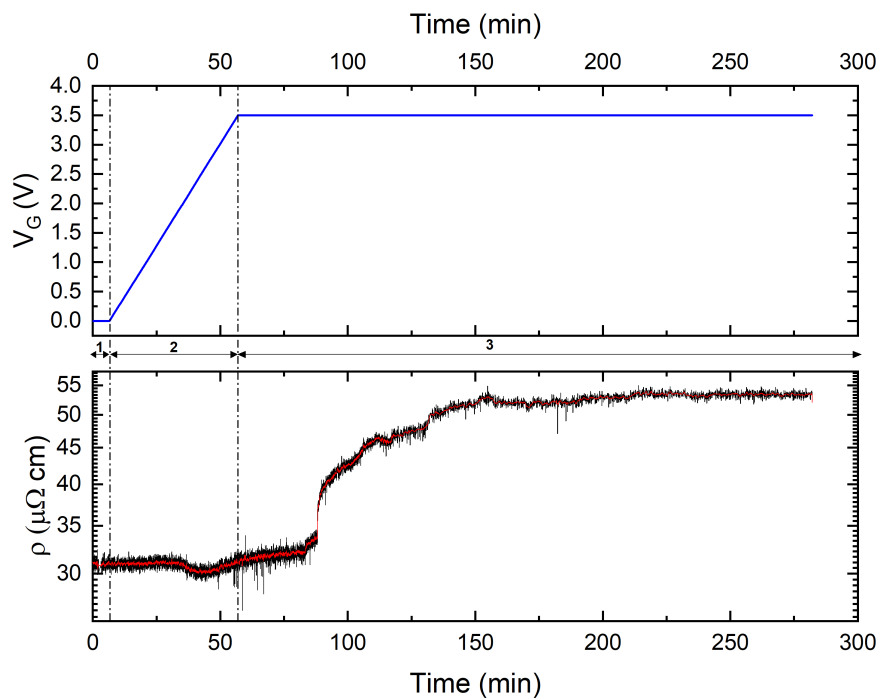


Figure 4.2.6: Gate voltage (upper panel - solid blue line) and resistivity (lower panel - solid red line) measured *in situ* as a function of time during a gating process. In this case the electric-field-driven ion intercalation was performed using the GT90 eutectic mixture.

this region, we observed that the resistivity shows an increasing behaviour. In particular, after about 30 minutes we observe a rapid growth from 35 to $45 \mu\Omega \text{ cm}$. Afterwards, for a further 60 minutes the resistivity continues to increase reaching the value of $55 \mu\Omega \text{ cm}$, and then it saturates at this value. The difference between the value reached at the end of the measurement ($\rho \sim 55 \mu\Omega \text{ cm}$) and the one at the beginning of region 2 ($\sim 30 \mu\Omega \text{ cm}$) is about $25 \mu\Omega \text{ cm}$. In a relative sense, this is an increase of about 83%. The behaviour in GT90 eutectic mixture is different from all those analysed in the case of EMIM-BF₄ ionic liquid, both *in situ* and *ex situ*. Indeed, the overall resistivity tends to increase, suggesting that the H⁺ bulk intercalation was successful. That is confirmed by the temperature resistivity measurements, as described in the following section.

4.2.1.2 Resistivity measurements

In this section we report the results of the resistivity measurements in temperature for the protonated Pd_{0.6}Cu_{0.4}H_{*x*} samples. The general description of the dependence of resistivity on temperature for metal and metal alloys has been reported in 4.1.1.2.

Figure 4.2.7 shows the normalized resistivity as function of the temperature for rep-

representative Pd_{0.6}Cu_{0.4} alloy samples in the case of *ex situ* electric-field-driven ion intercalation performed using the EMIM-BF₄ IL. *Ex situ* characterizations were performed after extracting the intercalated Pd_{0.6}Cu_{0.4} samples from the cell and rinsing them thoroughly with acetone and ethanol to remove ionic-liquid residues.

At first glance, the general behaviour for these three samples is substantially metallic, compatible with the trend shown in literature [89]. Starting from the pristine material (solid black line), we can notice that differently from pure Pd, here ρ_r is not negligible. This is quite obvious, considering that in this case we are dealing with an alloy.

Sample 1 (S1) curves have the same behaviour. We performed the electric-field-driven ion intercalation by applying a V_G equal to 3.0 V overnight after an annealing up to 330 K (Figure 4.2.5). S1 shows a ρ_r slightly higher than the pristine one, demonstrating that applied voltages, namely higher electric fields, can implant hydrogen ions. In order to confirm the repeatability of this trend, we heated S1 the first time (solid red line, S1_1); then, we cooled down the sample to 2.9 K and performed a second warm-up to 300 K (solid light green line, S3_1). One can observe that the two curves share the same trend with no significant differences.

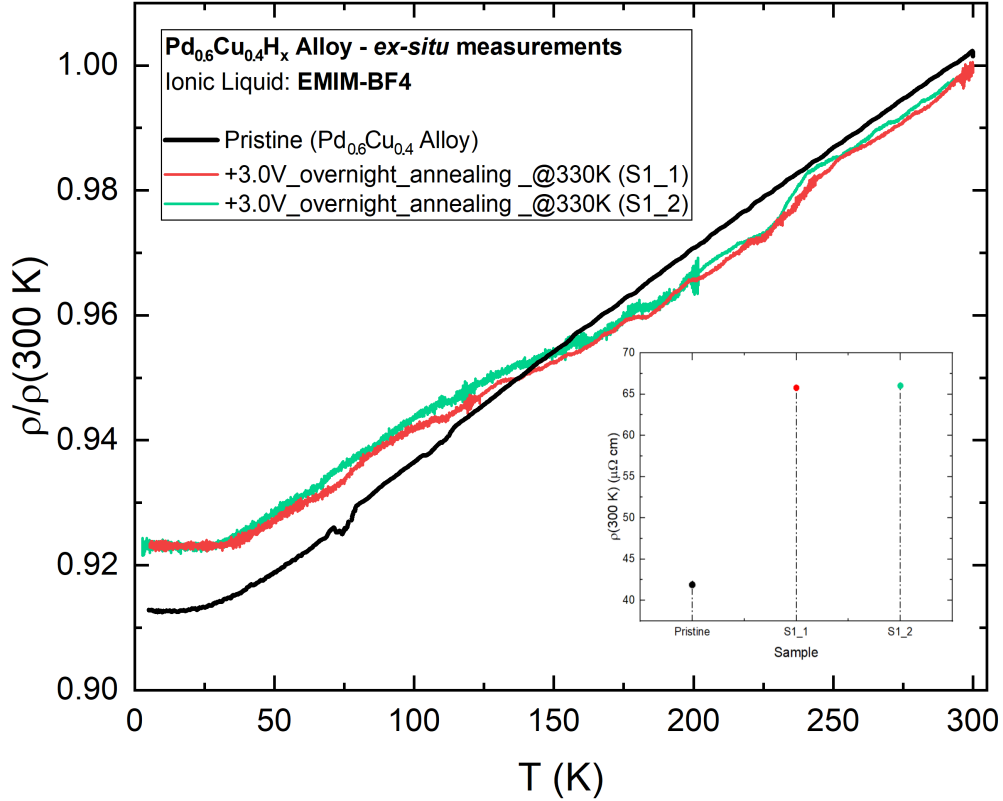


Figure 4.2.7: *Ex situ* resistivity measurements normalized at the value of the respective resistivity at 300 K ($\rho/\rho(300\text{K})$) in function of the temperature (T) for representative samples of the Pd_{0.6}Cu_{0.4} alloy before and after the electric-field-driven ion intercalation using the EMIM-BF₄ IL, in different gating conditions. The inset reports the temperature values of $\rho(300\text{K})$ for each analyzed sample.

The following Figure 4.2.8 refers to temperature resistivity measurements carried out on a batch of representative Pd_{0.6}Cu_{0.4} alloy samples intercalated with GT90 eutectic mixture.

In particular, Figure 4.2.8 shows the results of *ex situ* measurements. We performed the electric-field-driven ion intercalation by applying a V_G equal to 3.5 V overnight (Figure 4.2.6). Sample 1 (S1_1) shows a ρ_r lower than the pristine one. The resistivity difference at low temperatures, i.e. ρ_r , is minimal (approx. 1.5 %). Therefore, we can deduce that the electric fields can implant hydrogen ions but not in quantities large enough to trigger a superconductive behaviour (Figure 4.1.5). We heated S1 the first time (solid red line, S1_1); then, we cooled down the sample to 2.9 K and performed a second warm-up to 300 K (solid blue line, S1_2). One can observe that the two curves share the same trend but with a slight upward shift along at low temperature values. That probably depends on the metal dislocation recombinations due to the cooling and the reheating processes that alter the intrinsic component of the resistivity. Furthermore, we identify a

slight anomaly at 120 K in S1_1 and S1_2.

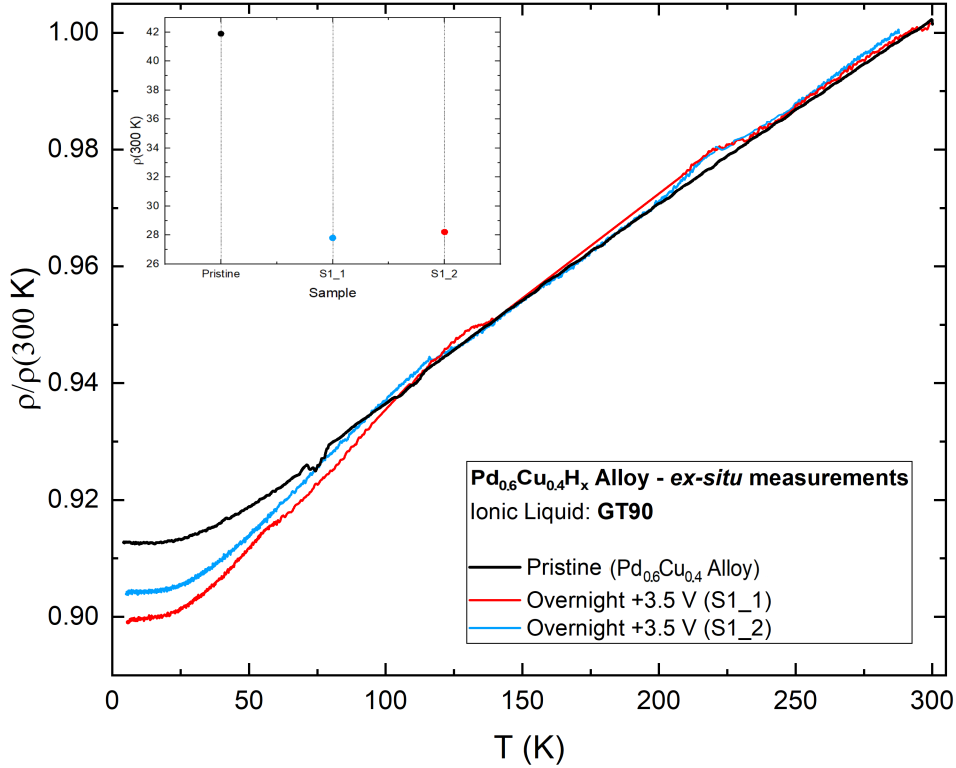


Figure 4.2.8: *Ex situ* resistivity measurements normalized at the value of the respective resistivity at 300 K ($\rho/\rho(300\text{K})$) in function of the temperature (T) for representative samples of $\text{Pd}_{0.6}\text{Cu}_{0.4}$ alloy after the electric-field-driven ion intercalation using the GT90 eutectic mixture, in different gating conditions. The inset reports the temperature values of $\rho(300\text{K})$ for each analyzed sample.

Up to now for $\text{Pd}_{0.6}\text{Cu}_{0.4}$, we can conclude that even if the general metallic behaviour of the curves does not change, the resistivity changes. In particular, in the case of the IL EMIM- BF_4 , at 300 K, ρ goes from a value of about $42\ \mu\Omega\text{cm}$ (pristine sample) to $65\ \mu\Omega\text{cm}$; for eutectic mixture GT90, the resistivity value reached is about $28\ \mu\Omega\text{cm}$. That shows that the intercalation worked, but the doping was insufficient to induce the SC transition. Considering that these results do not agree with our expectations and the literature's predictions of Vocaturo et al. [91], we decided to go deeper and analyse the crystalline structure of our samples to verify if our measurements were performed on the right and possibly superconductive phase.

4.2.1.3 X-ray diffraction

X-Ray diffraction analysis (XRD) is a non-destructive technique widely used to gain detailed information on the crystallographic structure, chemical composition, and physical properties of a solid material [94]. In brief, the crystal X-ray diffraction phenomenon results from a scattering process of the X-rays by the electrons of atoms present in the sample without changing the wavelength [95]. This latter is comparable with the distance between the crystal planes inside lattice [89].

X-rays used for diffraction are electromagnetic waves with wavelengths between 0.05 and 0.5 nm (0.5 and 5 angstrom, *white radiation*). The source of X-rays consists of a vacuum tube in which electrons are emitted from a heated tungsten (W) filament and accelerated by an electric potential (typically around 35 kV) to travel towards the metal target. When the W filament of the cathode is heated, electrons are released by thermionic emission, and then increase their kinetic energy. X-rays are generated when the electrons hit the metal target. Since most of the kinetic energy (about 98%) is converted into heat, the metal target must be cooled by an external cooling system [89, 96]. In general, during the experiments, a single characteristic radiation is selected using a filter or monochromator.

When the X-rays are incident upon a sample, they can either be transmitted, and thus they will continue along their original direction, or they will be scattered by the electron clouds around the atoms [97, 96]. All atoms along the X-ray beam path scatter X-rays. We focus on the peaks that form when constructive interference occurs between the scattered X-rays. This kind of interference develops when two X-ray waves with phases separated by an integer number of wavelengths add up to form a new wave with a larger amplitude. In this case, the path difference between two parallel X-rays from a coherent source that scatters from two adjacent planes must be an integer number of wavelengths, as shown in Equation 4.5.

So, the lattice distance can be calculated using Bragg's law:

$$n\lambda = 2d \sin \theta \quad (4.5)$$

where λ is the wavelength of the x-rays, θ is the angle between the incident rays and the surface of the crystal, d is the spacing among atoms layers, and n is an integer number (1, 2, ...) known as diffraction order, expressing the constructive interference between the rays.

The geometry of the Bragg condition determines that the angle between the transmitted and Bragg diffracted beams is always equal to 2θ , as shown in Figure 4.2.9. The output of the measurement is usually a spectrum where the intensity of the diffraction beam is plotted against the angle 2θ . This latter is readily obtainable in experimental situations thanks to a goniometer inside the equipment.

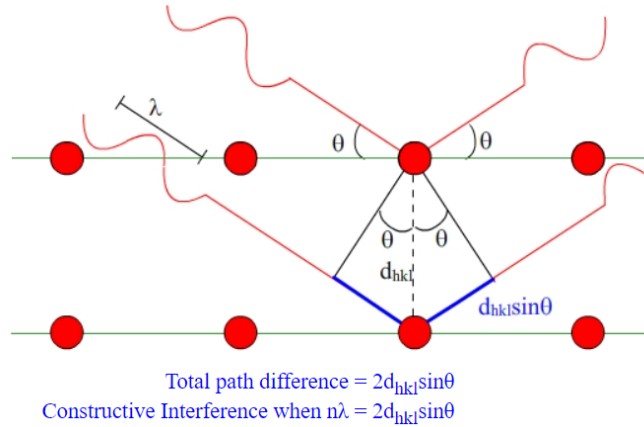


Figure 4.2.9: Reflection of a X-rays beam on the planes (hkl) of a crystal.

To pursue our experiments on the $\text{Pd}_{0.6}\text{Cu}_{0.4}$ alloy samples, we employed the so called versatile nondestructive Powder X-ray diffraction (P-XRD) technique, which is very common for the characterization of nanoscale materials. This bulk analysis provides important insights like phase identification, sample purity, crystallite size, and, in some cases, morphology [98].

A powder is a polycrystalline material, whose grains hold all possible randomic crystal orientations of the crystals, causing similar planes in various crystals to scatter in various directions. Differently from the single crystal X-ray diffraction, adding other crystals with slightly different orientations, imply the emergence of other diffraction spots for different 2θ values [96].

The diffraction pattern is helpful to determine and refine the lattice parameters of a crystal structure. For instance, the powder particle size can be computed via the Scherrer formula, which relates the particle size to the peak width, as follows

$$t = \frac{0.9\lambda}{\sqrt{B_M^2 - B_s^2} \cos \theta} \quad (4.6)$$

where λ is the x-ray wavelength, B_M is the width of the observed peak, B_s is the peak width of a crystalline standard and, as usual, θ indicates the diffraction angle.

To perform this characterization, we use a powder X-ray diffractometer. This set-up consists of an X-ray source, a sample holder, a detector and a tool to vary angle θ , as schematically presented in Figure 4.2.10.

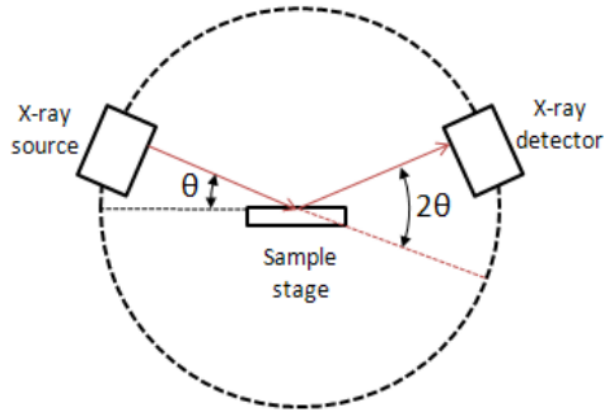


Figure 4.2.10: Schematic setup of the powder X-ray diffractometer. From [99].

At a specific angle, the X-ray is focused on the sample, and the detector measures the intensity of the received X-ray beam at an angular distance of 2θ from the source route. After that, the incident angle gradually increases while the detector angle steadily rises 2θ above the source path [100, 101]. Therefore, each accessible reflection at the 2θ angle specified by Bragg's Law results in rings of equal intensity in 2-dimension, which constitute the powder pattern [96].

4.2.1.4 Results and discussion

As discussed in paragraph 4.2, PdCu alloy can form both FCC and BCC (B2) crystal structures. As theoretically predicted in [91], the transition to the superconducting phase happens only in the B2 phase. Considering that our resistivity trends do not present any difference before and after the protonation process in terms of general metallic behaviour, we decided to characterize the crystalline structure of our samples using the XRD technique. We expected to find the characteristic peaks of the FCC phase, reported in Figure 4.2.11.

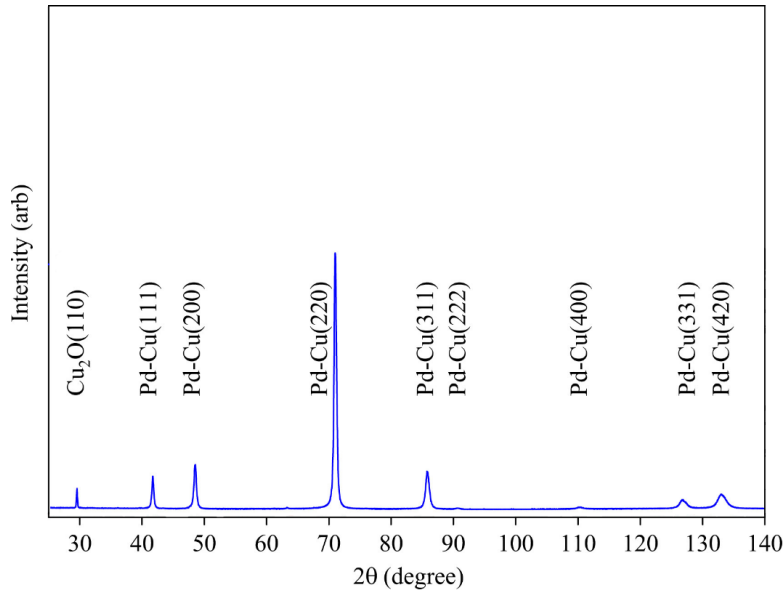


Figure 4.2.11: Representative XRD patterns of the Pd-Cu in the pure state. Adapted from [102].

Actually, performing XRD measurements on our pristine sample (solid black line in Figure 4.2.12) and comparing our results with the literature [102], we observed that our pure samples showed a diffraction spectrum with broad peaks around 40, 70 and 85°, typical of a disordered FCC structure as predicted. A refinement of this spectrum is represented by the dashed green line in Figure 4.2.12. The agreement of the refinement curve with the experimental data (especially the high intensity of peak 220 at around 70°) is only obtained if one admits a partial orientation of the crystallines of the low-thickness sample along that direction, which could be caused by the lamination process required for its production. During this process, counter-rotating rolls apply a force exceeding the material yield stress and thus entering the plastic deformation range. This way, the crystalline grains could be oriented along the rolls' movement direction [89].

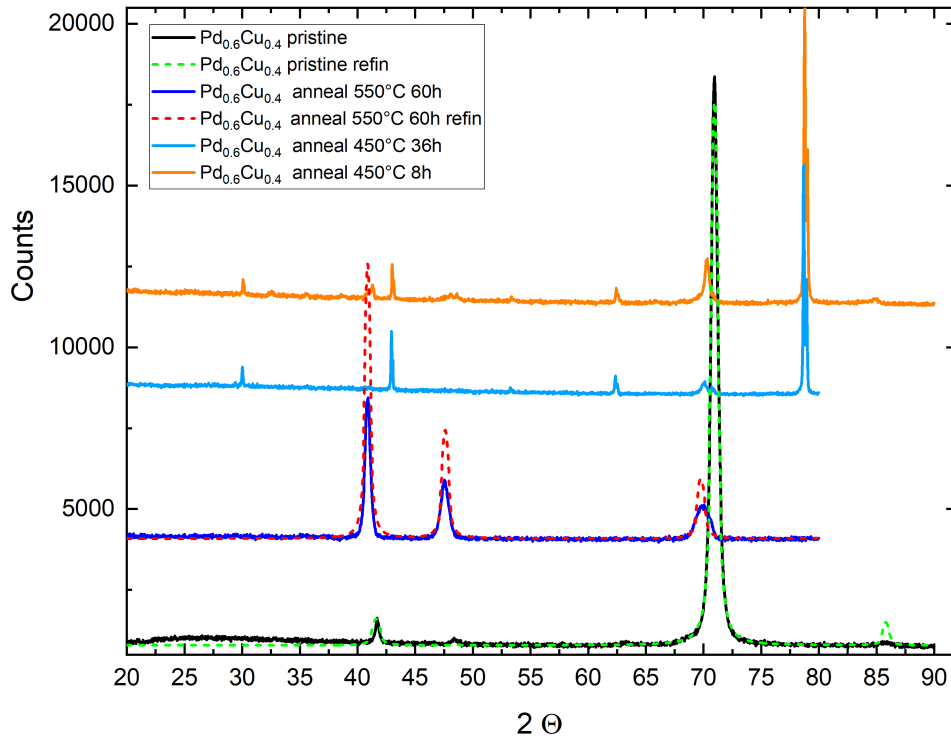


Figure 4.2.12: X-ray diffraction patterns of $\text{Pd}_{0.6}\text{Cu}_{0.4}$ alloys at different annealing conditions.

Theoretically, a complete BCC structure is needed to obtain a superconducting phase. Hence, drawing inspiration from the literature referring to hydrogen permeable membranes [103, 104] and from the phase diagram of the PdCu alloy (Figure 4.2.3), it is possible to switch to the B2 phase through an annealing process, controlling both the annealing temperature and the timing of this process. This is evident in Figure 4.2.13. Thus, we decided to perform several tests.

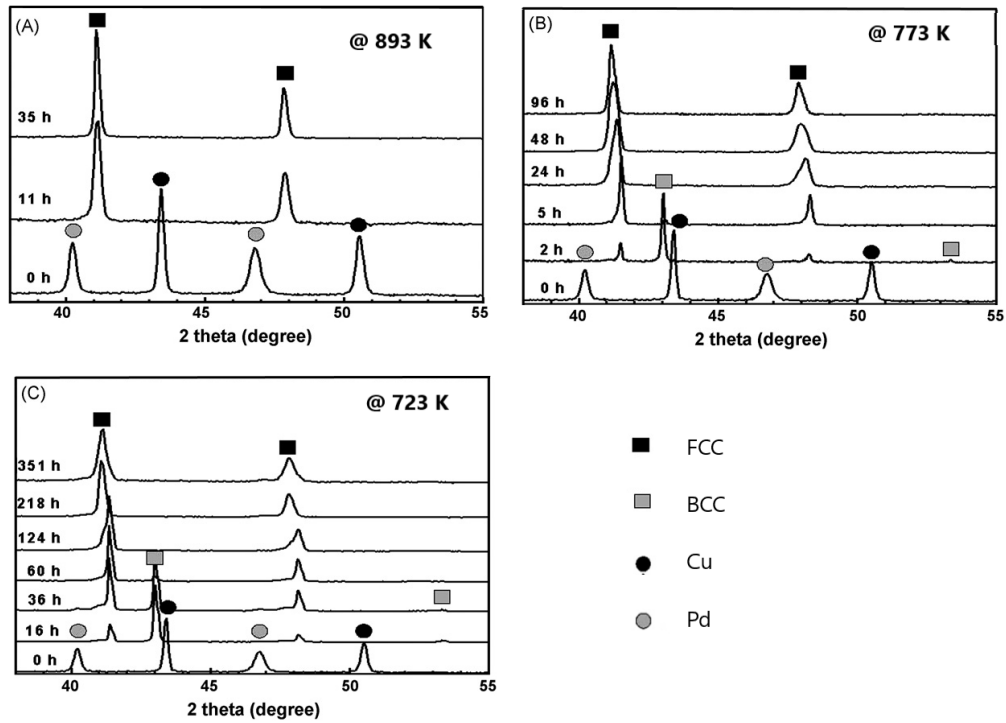


Figure 4.2.13: X-ray diffraction patterns as a function of the annealing time for $\text{Pd}_{0.64}\text{Cu}_{0.36}$ alloys. Adapted from [103].

For this reason, we carried out a first annealing up to 550 °C for 60 hours (solid blue line in Figure 4.2.12). However, as expected (see Figure 4.2.13B) XRD measurements showed an even more ordered FCC phase than the pristine one. The temperature-dependent resistivity measurement on this sample is shown Figure 4.2.14 (solid red line). Since the material has undergone crystalline recombination due to the annealing process, we observe that at low temperatures the ρ_r is lower than the pristine case. Increasing temperature the ρ_T assumes higher values with respect to the blue curve in Figure 4.2.14.

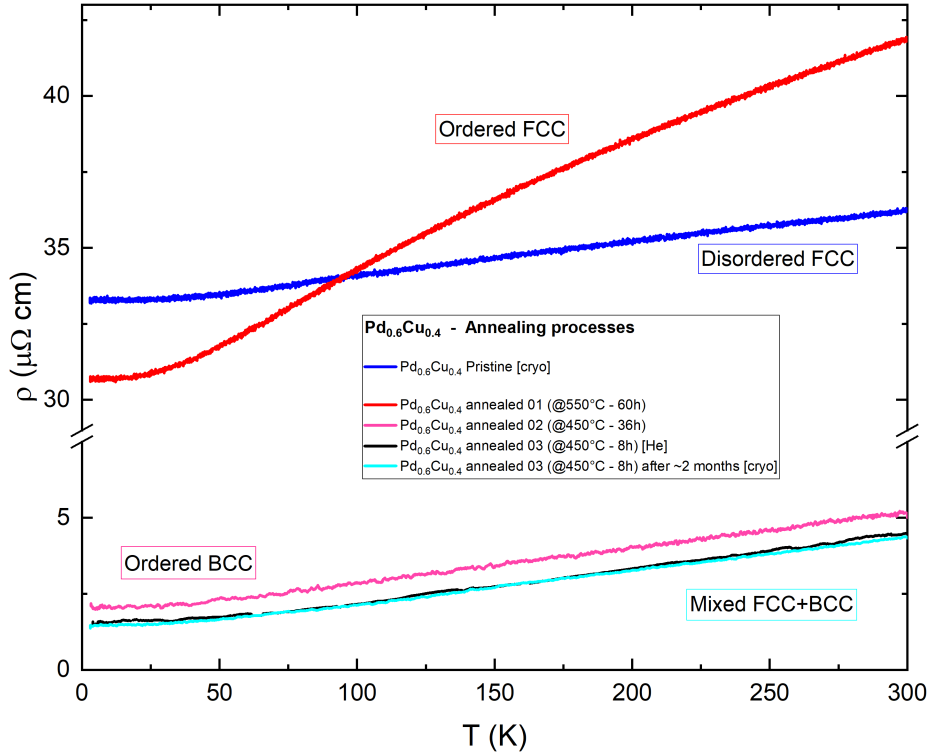


Figure 4.2.14: Resistivity measurements in function of the temperature for representative samples of $\text{Pd}_{0.6}\text{Cu}_{0.4}$ alloy before and after the annealing processes, in different temperature and time conditions. The squared labels indicate the phases obtained via the annealing treatments.

Therefore, we performed a second annealing at 450°C for 36 hours, which should produce a BCC phase (see Figure 4.2.13C) [103, 104]. The X-ray analysis performed after this thermal treatment actually confirmed the formation of the BCC-ordered structure, as shown in the solid light blue line in Figure 4.2.12. Temperature-dependent resistivity measurements reported in solid pink line in Figure 4.2.14 show the same overall trend of the pristine sample but with a downward shift of almost one order of magnitude, coherently to the ordering of the material induced by the annealing process, which reduces the ρ_r of the total resistivity. Moreover, performing the electric-field-driven ion intercalation with the GT90 eutectic mixture at $+3.5\text{ V}$ for 1 hour, we observed an overall metallic behaviour, as shown in Figure 4.2.15 (solid light blue line). Moreover, we highlighted also a hump during the drop in temperature at about 120 - 125 K. This latter features stable for about a couple of hours. This anomaly will be evident also in the mixed phase sample, which we will discuss in the following. These measurements were performed *in situ* to avoid hydrogen leakage. In particular, the ρ_r at low temperatures increased from about 2 to $3.5\ \mu\Omega\text{cm}$ due to the H^+ ions intercalation. Contrary to the theoretical predictions [91], there is no sign of superconducting transition.

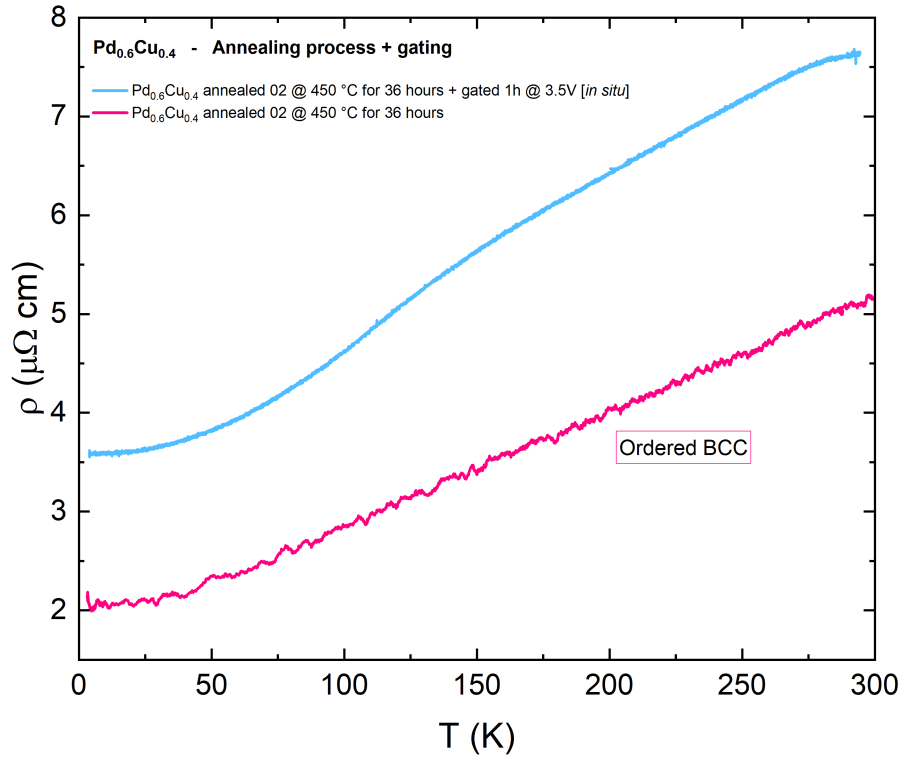


Figure 4.2.15: Resistivity measurements in function of the temperature for the $\text{Pd}_{0.6}\text{Cu}_{0.4}$ alloy after the annealing processes at 450°C for 36 hours (solid pink line) and for the same sample after the *in situ* electric-field-driven ion intercalation at $+3.5\text{ V}$ for 1 hour (solid blue line).

So, following previous works related to membrane technology [103, 104], we tried to realize via annealing a properly mixed phase with a higher concentration of FCC phase (annealing 3). Indeed, hydrogen has high mobility in the BCC phase. On the contrary, it is less mobile in the FCC phase, which could act as a hydrogen reservoir. Thus, it might be more likely to find a superconducting phase or superconducting islands in a mixed phase (FCC+BCC). Therefore, we heated a sample in the pristine state up to 450°C for about 8 hours. Subsequently, we carried out XRD measurements on this sample (solid orange line in Figure 4.2.12), and we noticed that in addition to the peaks of the FCC structure, also peaks typical of the BCC crystal structure appeared, forming a mixed state, coherently to the one reported in literature [105] and shown in Figure 4.2.16.

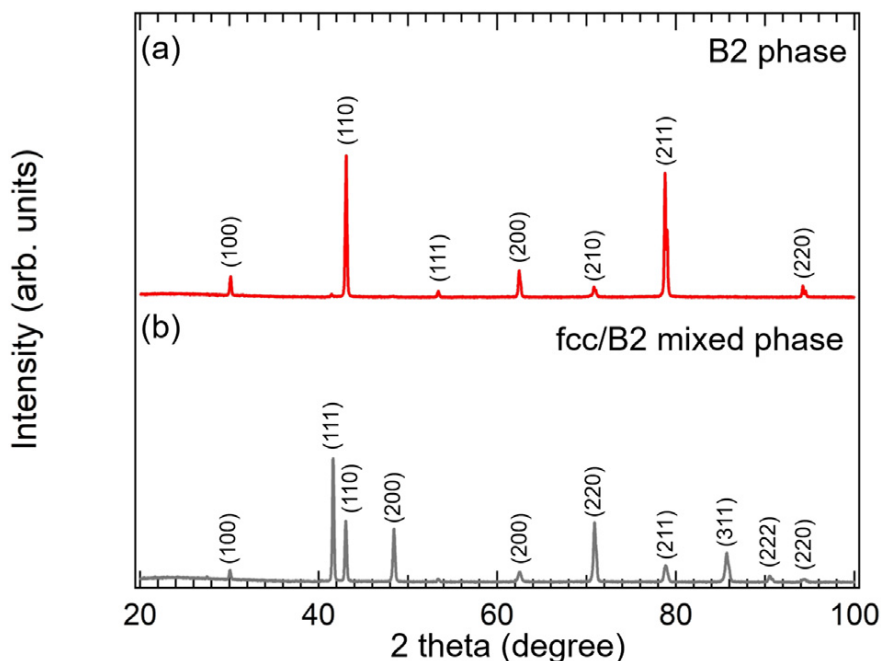


Figure 4.2.16: XRD patterns of (a) B2 and (b) FCC/B2 mixed phased $\text{Pd}_{0.6}\text{Cu}_{0.4}$ alloys in air. From [105].

On this sample, we performed resistivity measurements versus temperature to verify if electrical transport properties were modified by the presence of the mixed phase. The behaviour is the one already described in 4.1.1.2, namely a metallic one. In fact, we observe a decrease of the intrinsic component of the resistivity at low temperature of about 2 orders of magnitude with respect to the pristine curve (solid blue line), as shown in black and light blue curve in Figure 4.2.14. Moreover, black and light blue curves in Figure 4.2.14 present the same trend even if they were obtained via two different cooling technique and two months apart from each other. This demonstrates that the change occurred is structural at a crystalline level.

Then, we executed a suitable overnight protonation at +3V of this sample using the GT90 eutectic mixture in the usual manner described in 3.2.1.1. As observed in the green curve, resistivity measurements performed cooling the sample in liquid-He revealed a resistivity decrease at around 100 K. This behaviour, already seen in the ordered BCC phase (solid light blue line in Figure 4.2.15), could be compatible with the one of a mixed material (normal metal + superconductor). This anomaly results still present after a few days, and for this reason we decided to perform susceptibility measurements, which will be discussed in the following section 4.2.19. However, the measure was repeated after two months with the usual cryocooler technique (solid orange line). We observe a relatively small down-shift of the overall trend and the loss of the hump at ~ 100 K, restoring a pure metallic behaviour analogue to the ones observed in samples without protonation (black and light blue curves), as reported in Figure 4.2.17, as if most of the hydrogen

escaped during the waiting time.

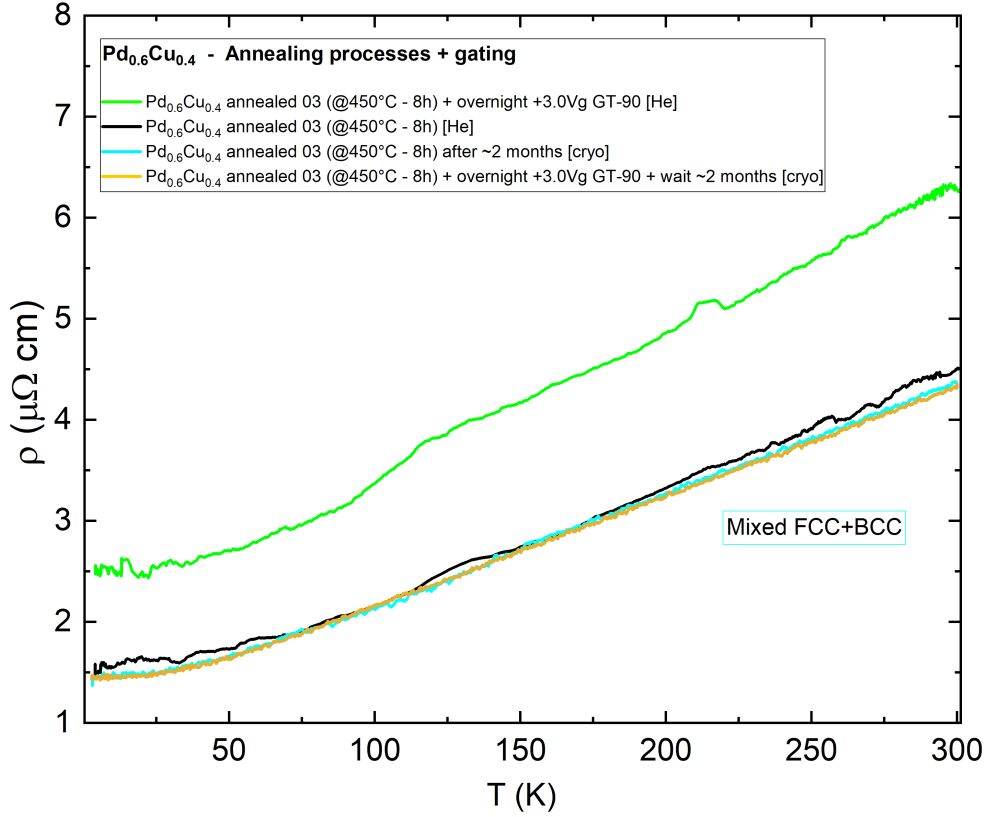


Figure 4.2.17: Resistivity measurements in function of the temperature for the Pd_{0.6}Cu_{0.4} alloy after the annealing processes at 450°C for 8 hours and for the same sample after the electric-field-driven ion intercalation with GT90 eutectic mixture at +3.0 V.

To better observe the anomaly we report Figure 4.2.18 with the normalized curve. We can also observe that for T higher than 200 K, all the curves present the same slope, while at low-temperatures the green curve show a higher residual resistivity ρ_r .

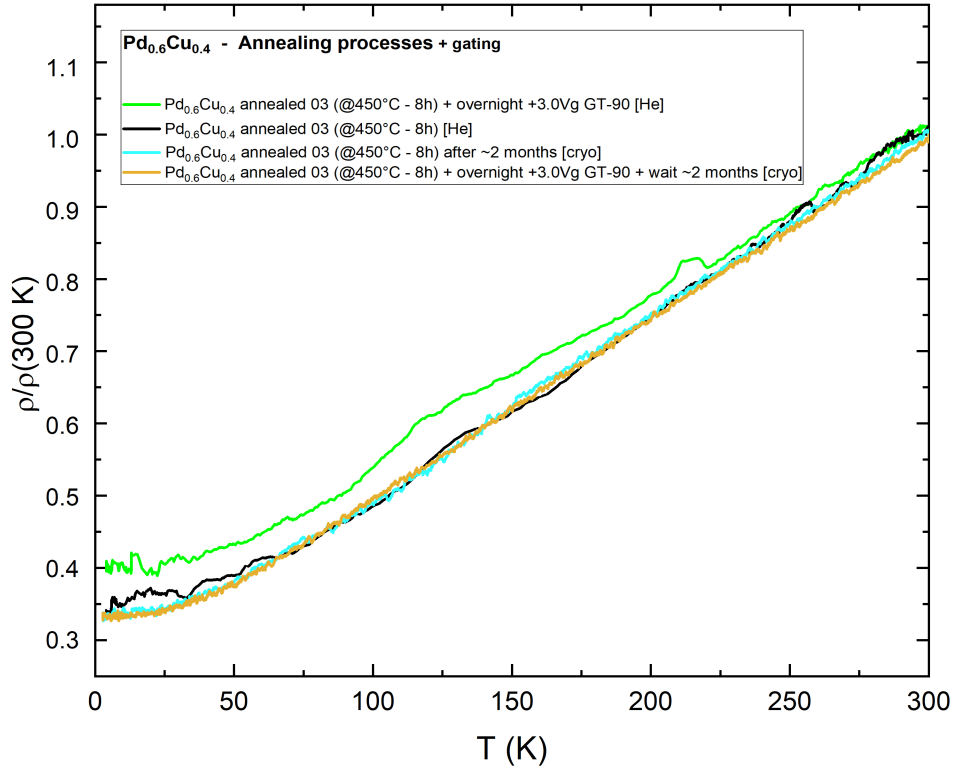


Figure 4.2.18: Resistivity measurements in function of the temperature for the $\text{Pd}_{0.6}\text{Cu}_{0.4}$ alloy normalized at the value of the resistivity at 300K of each sample ($\rho/\rho(300\text{ K})$) after the annealing processes at 450°C for 8 hours and for the same sample after the electric-field-driven ion intercalation with GT90 eutectic mixture at $+3.0\text{ V}$.

Clearly, there exist several mixed phases. Therefore, we proceeded by performing a fourth annealing at a temperature of 450°C for about 16 hours, obtaining X-rays peaks compatible with a new FCC-BCC mixed phase apparently richer in FCC phase, as predicted by the consulted literature relative to membranes technology [103, 104]. The investigation of the electric transport properties of these annealed samples and their response to hydrogen intercalation is currently under way.

4.2.1.5 Magnetic susceptibility

Magnetic susceptibility measurement is used for determining phase boundaries in magnetic systems as a consequence of a distinct change in magnetic properties when they undergo a phase transition [106, 107]. The magnetic susceptibility, or in brief susceptibility (χ), is defined as the ratio between the magnetization M and the magnetic field H , namely

$$\chi = \frac{M}{H} \quad (4.7)$$

So, χ is nothing but the "true" proportionality constant (independent of both H and M) in almost all the materials, except in ferromagnetic materials where it depends on H . Indeed, materials possess different magnetic properties in an applied H , ranging from paramagnetism (alignment with the magnetic field, $\chi > 0$) and diamagnetism (alignment against the field, $\chi < 0$). In the case of ferromagnets, χ is a non-univocal function of H due to the formation of hysteresis loops. In general, χ is related to the magnetic permeability μ_r , of the medium through the equation

$$B = \mu_0(1 + \chi)H \quad (4.8)$$

providing that $\mu_r = 1 + \chi$.

Concerning the origin of magnetization, it depends on microscopic/quantum phenomena. The main contribution to the magnetization of diamagnetic materials is the Larmor precession. According to this phenomenon, the applied field causes electrons' precession on the orbitals, which results in atomic currents originating a small magnetic moment antiparallel to the applied field. That is quite different for paramagnetic materials. Here, atoms already have intrinsic and random small magnetic moments. The application of an external field tends to orient them, generating a macroscopic (but small) magnetic moment. In contrast, in ferromagnetic materials, dipoles tend to align, and the material can exhibit magnetic moments even when no external field is applied. In particular, dipoles tend to form the so-called Bloch domains, each with a specific orientation, minimizing the system energy. Here, the $M(H)$ curve is not linear and also strongly hysteretic. Consequently, the resulting curve does not intercept the origin of the axes. In these cases, it is preferable to define a differential susceptibility as $\chi = dM/dH$ [107].

Up to now, we have considered only static magnetic fields. However, when the magnetic susceptibility is measured in response to an AC magnetic field, i.e. which oscillates in time without changing its direction, this is called AC susceptibility. In this case, the field amplitude can be expressed by $H(t) = H_0 e^{i\omega t}$. Consequently, one expects that the magnetization of a certain material should also oscillate in time with the same frequency as the external field. More in detail, if the frequency is sufficiently small, then the material's response oscillates in phase with the inducing field, so that $M(t) = M_0 e^{i\omega t}$ [107]. Then,

$$\chi_{AC} = \chi = \frac{M_0 e^{i\omega t}}{H_0 e^{i\omega t}} = \frac{M_0}{H_0} \quad (4.9)$$

that is a real number. Interestingly, at the very-low-frequency regime, the AC susceptibility is practically the same as in the DC case, i.e. it measures the slope of the M(H) curve at zero fields. On the contrary, at higher frequencies, there may be a certain delay in the magnetic response of the material, so that the magnetization is no longer in phase with the inducing field, and $H(t) = H_0 e^{i\omega t}$ while $M(t) = M_0 e^{i\omega t + \varphi}$. Then, we get:

$$\chi = \frac{M_0 e^{i\omega t + \varphi}}{H_0 e^{i\omega t}} = \frac{M_0}{H_0} e^{i\varphi} = |\chi| e^{i\varphi} \quad (4.10)$$

Therefore, we can distinguish the real and imaginary parts of the susceptibility. More explicitly

$$\chi = \chi' + i\chi'' \quad (4.11)$$

where

$$\begin{aligned} |\chi| &= \sqrt{\chi'^2 + \chi''^2} \\ \chi' &= |\chi| \cos \phi \\ \chi'' &= |\chi| \sin \phi \\ \varphi &= \arctan \chi'' / \chi' \end{aligned}$$

as sketched in Figure 4.2.19

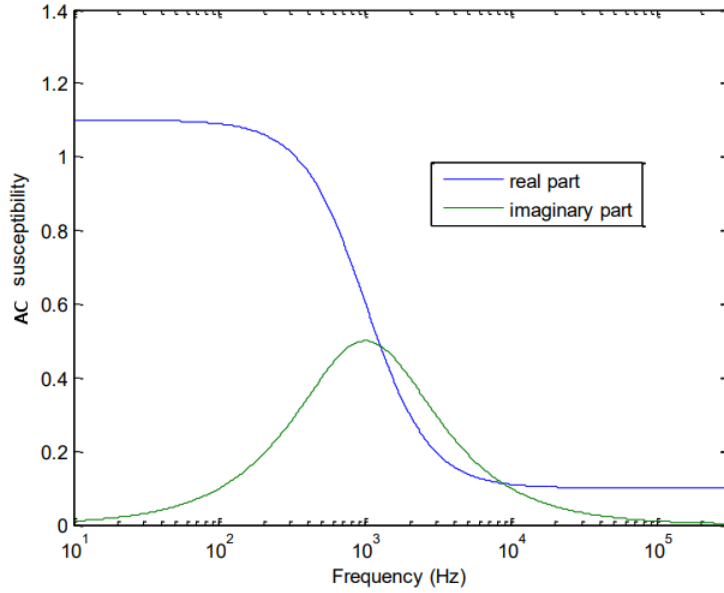


Figure 4.2.19: Real (solid blue line) and Imaginary (solid green line) parts of the AC susceptibility versus frequency. Adapted from [108].

The **real part** measures the type of magnetism of the sample. However, in contrast to the DC case, now the magnetization is not only due to the fictitious currents that account for microscopic phenomena, but also to true electrical currents flowing on the sample surface because of the Faraday law, known as eddy or Foucault's currents. Specifically, these latter are transient currents that naturally appear in the conducting parts of the sample under investigation (a conductor) and tend to oppose to the applied magnetic field variations [109]. This second contribution can be orders of magnitude greater than the first one; therefore, the effect of screening current might mask the intrinsic magnetic characteristics of the material. Of course, this is true in particular in the case of good conductors. The contribution of eddy currents can be minimized by suitable sample geometries or by using finely milled or polycrystalline materials.

The **imaginary part** of the AC susceptibility is referred to the leakage currents, proportional to the area of the hysteresis loop induced by the variable magnetic field. More in detail:

- in conductive samples, the dissipation is due to screening currents flowing on the sample surface and induced by the variation in time of the magnetic flux concatenated with the sample volume, according to the Faraday law. In this case, the value of χ'' depends on the conductivity of the material and on the volume fraction in which the dissipation really occurs, i.e. on the penetration depth λ . In general, χ'' increases with the conductivity and with the penetration depth.

For example, in superconductors a peak in χ'' develops just below the T_C . The sudden decrease of resistivity at T_C first gives rise to a great increase in χ'' . At the same time, the magnetic field starts to be expelled from the sample, according to the so-called Meissner effect. This latter decreases the volume where the dissipation can occur, thus decreasing also χ'' . The result is a peak in the $\chi''(T)$ curve.

- in ferromagnets, the H variation gives rise to a change in the extension of the magnetic domains, so that some expand and others shrink. This process implies a motion of the domain walls (Bloch walls) that originates energy dissipation, determining a non-zero χ'' and the irreversibility of the magnetization curves that, as expressed in the previous paragraphs, present hysteresis phenomena.

To perform the AC susceptibility measurements, we use an AC susceptometer, composed of two sets of coupled coils. The two primary coils (P1 and P2) are connected in series and are fed with an AC current. The AC voltage is measured by a lock-in amplifier connected to the series of the two secondary coils (S1 and S2) that are wound in opposite senses, as displayed in Figure 4.2.20 [107].

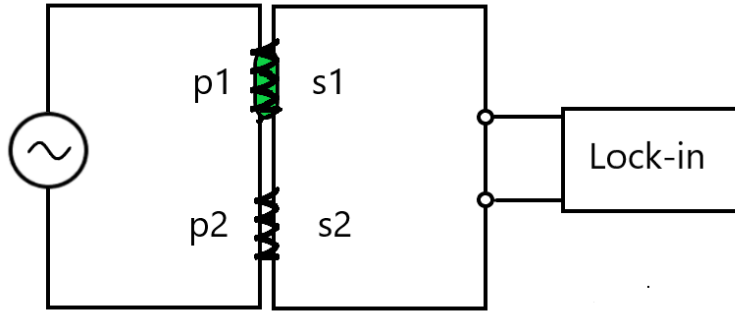


Figure 4.2.20: Schematic drawing of the AC susceptometer. Adapted from [23].

Let us shortly proceed to clarify the role and the basic features of the lock-in device, whose block diagram is reported in Figure 4.2.21.

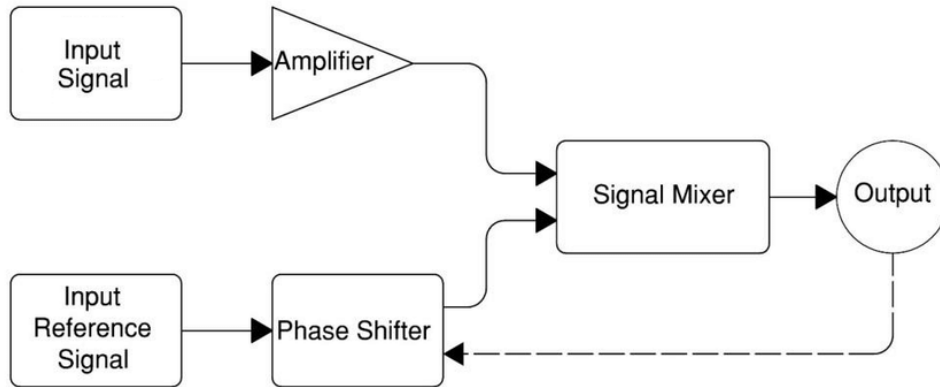


Figure 4.2.21: Lock-in amplifier block diagram. From [110].

It is a selective amplifier coupled to a phase sensitive voltmeter used to detect and measure very small AC signals, down to a few nV, also when the small signal is obscured by noise sources larger than it. To identify the signal component at a specific reference frequency and phase, this amplifier uses a technique known as phase-sensitive detection. This latter is a powerful tool that allows us to get a noise-free signal. To do that, the lock-in performs a Fourier transform of the input signal and rejects all the component that oscillates at frequencies different from the reference one, which can be set by the user or determined by the reference signal [107, 111]. In our experiments, we used a reference signal generated by the current generator. In this way, the lock-in selects the input signal component with the same frequency as the current in the primary coils. Hence, the signal-to-noise ratio can be significantly improved because the lock-in amplifies just the chosen component. Then, always at the reference frequency, the lock-in evaluates the voltage root mean square (rms) value. Generally, this voltage is not in phase with the reference signal. The lock-in measures this phase with respect to the reference

signal, and then decomposes the voltage signal and output in its component in phase (V_0) and out of phase (V_{90}) with the current [107].

Now, we introduce the mathematical description of this measurement, starting from what happens when no sample is inserted in the apparatus. In this case, a background voltage is detected as follows.

$$V = V_0 = V_1^0 + V_2^0 = \frac{d\phi_1^0}{dt} - \frac{d\phi_2^0}{dt} \quad (4.12)$$

where ϕ_1 and ϕ_2 are the flux of the magnetic field generated by P_1 and P_2 , respectively, and concatenated with the correspondent secondary set of coils. More in detail

$$\begin{aligned} \phi_1^0(B) &= BN_1S_1 \\ \phi_2^0(B) &= BN_2S_2 \end{aligned}$$

where B indicates the field generated by only one of the two primary coils, supposed to be identical; N_1 and N_2 are the number of turns in the respective secondary coil, and S_1 and S_2 are the cross-sections of the respective secondary coil. Recalling the expression of $B = \mu_0in_p$, where n_p is the number of turns per unit length in the primary coils, we can rewrite the previous expressions as

$$\begin{aligned} \phi_1^0(B) &= \mu_0in_pN_1S_1 = M_1i \\ \phi_2^0(B) &= \mu_0in_pN_2S_2 = M_2i \end{aligned}$$

where M_1 and M_2 are the mutual inductances of the two sets of coils. So, the V_0 is simply given by

$$V_0 = (M_1 - M_2)i \quad (4.13)$$

If we insert a sample into the first coil, as sketched in Figure 4.2.20, the lock-in measures a voltage equal to

$$V = V_1 + V_2^0 = \frac{d\phi_1}{dt} - \frac{d\phi_2^0}{dt} \quad (4.14)$$

In particular, the voltage at the end of S_1 is given by

$$V_1 = V_1^0 + \mu_0n_pn_1V_{sample}\chi_{ext}\frac{di}{dt} \quad (4.15)$$

where $n_1 = N_1/L$ is the number of turns per unit length in the S_1 . So, the total voltage is

$$V = V_1^0 + V_2^0 + \mu_0n_pn_1V_{sample}\chi_{ext}\frac{di}{dt} \quad (4.16)$$

In order to eliminate the effect of the difference between the two secondary coils, we subtract V_0 , obtaining a net contribution due to the sample equal to

$$\Delta V = V - V_0 = \alpha\mu_0n_1n_pV_{sample}\chi_{ext}\frac{di}{dt} \quad (4.17)$$

where a correction for the finite geometry of the coils is considered into α . Finally, expressing the current in the primary coil in terms of the magnetic field H , and supposing that $H(t) = H_0 e^{i\omega t}$, one gets

$$\Delta V = i\alpha\mu_0 n_1 V_{sample} \chi_{ext} \omega H_0 e^{i\omega t} \quad (4.18)$$

Considering that χ_{ext} is a complex number, we get

$$\begin{aligned} \Delta V &= i\alpha\mu_0 n_1 V_{sample} (\chi'_{ext} + i\chi''_{ext}) \omega H_0 e^{i\omega t} \\ &= -\alpha\mu_0 n_1 V_{sample} \omega \chi''_{ext} H_0 e^{i\omega t} + i\alpha\mu_0 n_1 V_{sample} \omega \chi'_{ext} H_0 e^{i\omega t} \\ &= \nu_0(t) + i\nu_{90}(t) \end{aligned} \quad (4.19)$$

We can deduce that $\nu_0(t)$ oscillates in phase with the current in the primary coils and is directly connected to the imaginary part of the external susceptibility χ''_{ext} . Instead, $\nu_{90}(t)$ oscillates with a phase of $\pi/2$ and is related to χ'_{ext} .

As said before, the lock-in is able to compute the rms values of the $\nu_0(t)$ and $\nu_{90}(t)$, i.e.,

$$\begin{aligned} \nu_0(t) &= \sqrt{2} \nu_0 e^{i\omega t} \\ \nu_{90}(t) &= \sqrt{2} \nu_{90} e^{i\omega t} \end{aligned}$$

respectively. In conclusion, we get

$$\chi''_{ext} = -b \frac{\nu_0}{V_{sample}} \quad (4.20)$$

$$\chi'_{ext} = +b \frac{\nu_{90}}{V_{sample}} \quad (4.21)$$

where the b constant contains all the quantities that do not depend on the sample and can be obtained through a calibration procedure.

4.2.1.6 Results and discussion

We performed susceptibility measurements on the mixed-phase sample, whose result is shown in Figure 4.2.22.

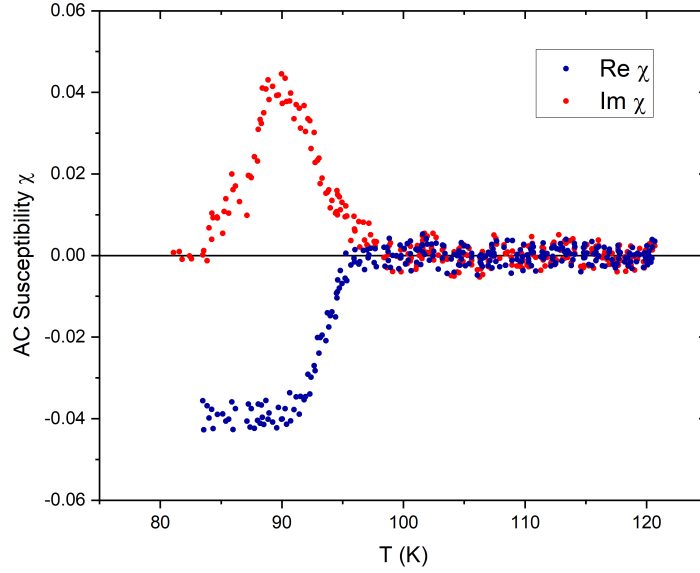


Figure 4.2.22: Real (blue dots) and imaginary (red dots) components of the susceptibility of PdCu alloy protonated with GT90 IL annealed in the mixed (FCC+B2) crystalline phase regime.

Analyzing the trend of the real part χ' associated with the dispersion starting from 120 K to lower temperatures, we observe that χ' assumes a null value down to 96 K. Then, in the temperature range between 96 and 90 K, we observe a sharp decrease of χ' to a negative constant low-intensity signal around -0.04, which is maintained down to 80 K. This result is coherent with the literature [112], where a sharper drop generally occurs closer to the critical temperature, showing a diamagnetic behaviour.

For the absorption component of the susceptibility, i.e., χ'' , we observe a peak at about 90 K. According to the literature [112], it should be close to the centre of the sharp diamagnetic change in χ' because diamagnetic susceptibility obeys the Kramers–Kronig relations. At a quantum level, as reported in [112], Clem (1992) suggested that, in the case of a superconducting material, there are three relevant mechanisms accountable for AC susceptibility losses, namely

1. eddy current or viscous losses, that develop when time-varying currents induce fluxons' movements in absence of pinning centres; In particular, a fluxon is a quantum of electromagnetic flux;
2. hysteresis losses that stop the flux motion from moving towards pinning centres. These losses could also manifest in each point of the material where vortices of opposite senses annihilate each other;
3. pinning losses on the surface caused by a surface barrier to vortex entry and escape.

Another more reasonable explanation could be the hydrogen ordering, i.e., the formation at low temperature of island of stoichiometric PdCuH, similar to that hypothesised in the PdH system by [72].

In conclusion, these experimental results encourage us to say that if PdCu is in a mixed (prevalent FCC + minority BCC) crystalline phase, changes can be induced in both transport and magnetic properties through the intercalation of hydrogen. The causes of the emergence of this signal are unknown up to now. They could be associated with the existence of fluxons and then a superconducting state at very high T_c , as predicted by ab-initio calculations [91], or hydrogen ordering into the lattice. Clearly, other investigations are necessary: for example, we suggest performing specific heat measurements to verify if a filamentary superconductive state is present. Indeed, due to low-intensity of the acquired susceptibility signals, we can suppose that only a small part of the material can exhibit these behaviours.

Chapter 5

Molybdenum Disulphide

5.1 General description of Transition metal dichalcogenides

Two-dimensional (2D) materials are nanoscale crystalline solids with relatively large lateral dimensions compared to their atomic-scale thickness. Thus, they recently became a trending topic thanks to their promising properties [113, 114, 115]. The bulk form of these materials is a stack of layers kept together through inter-layer van der Waals interactions and intra-layer covalent bonds. Their atomic-scale thickness allows modulating their properties via external electric fields. In addition, electronic and optical properties can be modified by controlling the number of layers in mesoscopic structures. One of the most relevant examples is graphite, composed by a stack of single monolayer graphene often obtained through micromechanical cleavage. It is extensively studied for its interesting physical features and high mobility. One of the main drawbacks of pristine graphene is its lack of a bandgap, which is necessary for different fields of applications, like electronics and optoelectronics. While, it is possible to induce and tune the bandgap of graphene this implies an increase of the complexity, a reduction of the mobility or the use of very high voltages (of the order of 100 V) [115]. In nature, several materials present a layered structure that could be mechanically cleaved along the layers, allowing their use as dry lubricants. Some examples of these materials are the previously mentioned graphite or boron nitride and molybdenum disulfide (MoS_2) [116, 117]. The first demonstration of a high-quality device based on a 2D material different from graphene was a field-effect transistor (FET) with a high ON/OFF ratio, based on a single layer of MoS_2 , a semiconducting material from the transition-metal dichalcogenide (TMD) family [116].

TMDs are quasi-two-dimensional layered compounds composed of transition metal elements (M) and chalcogen ones (X). They display different electrical properties, varying from semiconducting to superconducting, depending on their chemical composition (MX_2). Notably, these materials are known to present strongly competing effects of charge-density wave (CDW) formation and superconductivity (SC) [40], often resulting in anomalies in the electric transport properties [118]. A

single layer of TMD actually contains three atomic layers, having the transition metal elements sandwiched between two sheets of chalcogen element [119]. Typically, a single-layered TMD features either an octahedral or a trigonal prismatic coordination phase. The weak van der Waals interactions between the hexagonal layers of octahedral or trigonal prismatic TMD building blocks, which are schematically represented in Figure 5.1.1, allow the formation of many polytypes.

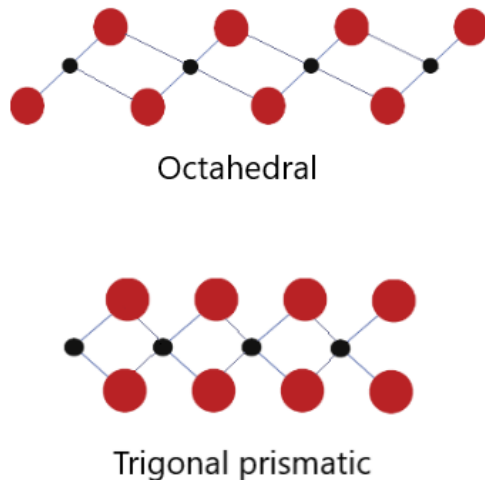


Figure 5.1.1: Representation of the repetition of the two main TMD coordinations. The small black and large red circles respectively represent the transition metal and chalcogen atoms. Adapted from [40].

Since each layer in multi-layered TMDs is capable of having any of the two coordination phases, a wide range of polymorphic configurations is possible. The three most common polymorphs, shown in Figure 5.1.2, are defined as 1T, 2H and 3R, where the digit indicates of the number of layers in the crystallographic unit cell, and the letter specifies the type of symmetry displayed. More in detail, T stands for tetragonal, H for hexagonal, and R for rhombohedral symmetry. The 2H and 3R forms both exhibit semiconducting behavior, in contrast to the 1T form's metallic behavior [120].

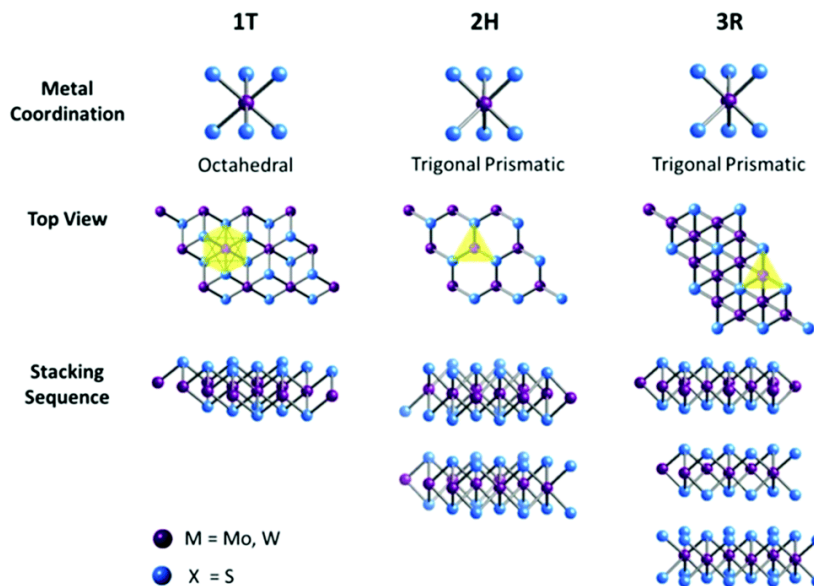


Figure 5.1.2: Metal coordinations and stacking sequences of TMD structural unit cells. Adapted from [120].

In particular, the most common polytypes of TiSe_2 , NbSe_2 and MoS_2 are the 1T, 2H(a) and 2H(b) forms, consisting of identical octahedral layers and two kinds of prismatic trigonal double layers, respectively [40]. Moreover, all this combined with the relatively large interlayer distance (approximately 6.5 \AA), allows alkaline ions to be easily inserted into the abundant space between the layers [121].

It is possible to distinguish around 60 different TMD compounds, with at least 40 of them possessing a layered structure. The periodic table in Figure 5.1.3 highlights the transition metals and the three chalcogen elements that primarily crystallize in those layered structures. Co, Rh, Ir and Ni, on the other hand, can only form layered structures in some dichalcogenides: e.g., NiTe_2 is a layered compound, while NiS_2 has a pyrite structure [40, 122].

MX ₂ M = Transition metal X = Chalcogen																	
H																	He
Li	Be											B	C	N	O	F	Ne
Na	Mg	3	4	5	6	7	8	9	10	11	12	Al	Si	P	S	Cl	Ar
K	Ca	Sc	Ti	V	Cr	Mn	Fe	Co	Ni	Cu	Zn	Ga	Ge	As	Se	Br	Kr
Rb	Sr	Y	Zr	Nb	Mo	Tc	Ru	Rh	Pd	Ag	Cd	In	Sn	Sb	Te	I	Xe
Cs	Ba	La-Lu	Hf	Ta	W	Re	Os	Ir	Pt	Au	Hg	Tl	Pb	Bi	Po	At	Rn
Fr	Ra	Ac-Lr	Rf	Db	Sg	Bh	Hs	Mt	Ds	Rg	Cn	Uut	Fl	Uup	Lv	Uus	Uuo

Figure 5.1.3: Transition metals and chalcogen elements forming TMDs are highlighted in the periodic table. Adapted from [122].

Semiconducting TMDs present an interesting evolution of the bandgap structure in the transition from bulk to single-layer crystal. Indeed, the bandgap is indirect in the bulk and multilayer, while it becomes direct in the single-layer limit, reflecting the progressive quantum confinement deriving from reducing the numbers of layers. The main difference between direct and indirect bandgap is the shape of the valence and conduction bands. In particular, this is evident when studying their dispersion relation (as a function of the wavevector k) and the crystal momentum, described by a Bloch wave function. Focusing on the first Brillouin zone (BZ), as shown in Figure 5.1.4, a direct bandgap occurs when the maximum of the valence band and the minimum of the conduction band are reached at the same value of k . Otherwise, an indirect bandgap occurs [123].

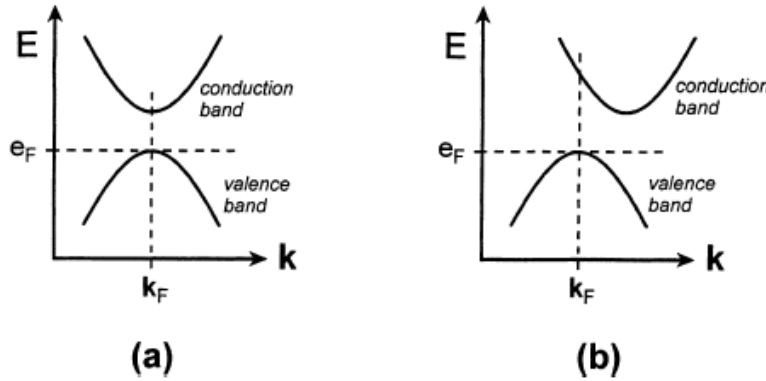


Figure 5.1.4: Schematic representations of electronic band structures near the Fermi level for a solid with a direct bandgap (a) and a solid with an indirect bandgap (b). e_F is the Fermi level having the Fermi wave vector k_F . From [123].

TMDs exhibit a unique combination of atomic-scale thickness, indirect-to-direct bandgap transition in the monolayer, strong spin-orbit coupling and favourable electronic and mechanical properties, which can be tuned via thickness, deformation, pressure, and crystallographic phase transition (for example, 2H-1T-dT, where dT is a more stable phase respect to the other two)[121]. Then, the relatively simple crystal structures combined with the complex electronic structures and correlations originates rich phase diagrams, making them interesting for fundamental studies and applications in high-end electronics, spintronics, optoelectronics, energy harvesting, flexible electronics, DNA sequencing and personalized medicine [118, 119].

Molybdenum Disulphide (MoS_2) is the most studied material in this family. We will examine this material in more detail in the following section.

5.2 General description of Molybdenum Disulphide

The bulk form of the MoS_2 consists of stacked monolayers, composed of one Molybdenum (Mo) atom surrounded by six Sulphur (S) atoms, as pictorially shown in Figure 5.1.2. As previously mentioned in the general description of the TMDs in Section 5.1, the adjacent layers are held together via weak Van der Waals forces. These latter help the layers of MoS_2 slide on each other. Moreover, MoS_2 displays different mechanical characteristics between the in-plane axes (a,b axes) and the out-of-plane axis (c axis). These properties make it efficient, for example, as a solid lubricant. Most relevantly, MoS_2 exhibits several different polymorphs, admitting three different typologies of configurations such as 1T, 2H and 3R (Figure 5.1.2) [124]. The thermodynamically-stable (up to around 1024°C) and naturally-occurring phase is the semiconducting 2H- MoS_2 , in which each Mo atom is coordinated by six S atoms in a trigonal prismatic geometry [125], exhibiting a hexagonal Bravais lattice structure. It behaves like an n-type semiconductor presenting a charge carrier mobility up to $100 \text{ cm}^2/(\text{Vs})$. However, in nature, it is possible also to find the 3R phase in a small percentage, approximately around the 3% of the total amount. On the contrary, intercalating the 2H- MoS_2 with alkali metals, such as Lithium (Li^+), it is possible to obtain the 1T- MoS_2 polytype, which represents a metastable crystalline phase. It possess hexagonal symmetry and exhibits a metallic behaviour.

The 2H- MoS_2 represents one of the most studied semiconducting TMDs due to its chemical stability, ease of exfoliation and indirect-to-direct band gap transition in monolayer, which make it ideally suited to the development of (opto-)electronic applications [118]. In particular, Figure 5.2.1 shows the calculated band structures evolving from bulk MoS_2 (panel a) to monolayer MoS_2 (panel d). Bulk MoS_2 is characterized by an indirect bandgap of 1.2 eV at the Γ point. However, it is possible to highlight the presence of a direct transition occurring at higher energies (K point). Since the first one is characterized by a smaller energy difference, bandgap transitions occur at the indirect bandgap. Reducing the layer thickness, the indirect bandgap becomes larger (panels b and c), while the direct bandgap does not undergo any appreciable change. Monolayer MoS_2 (panel d), becomes a direct-bandgap semiconductor, with a minimum energy difference of 1.8 eV shifted at the K point [115, 126].

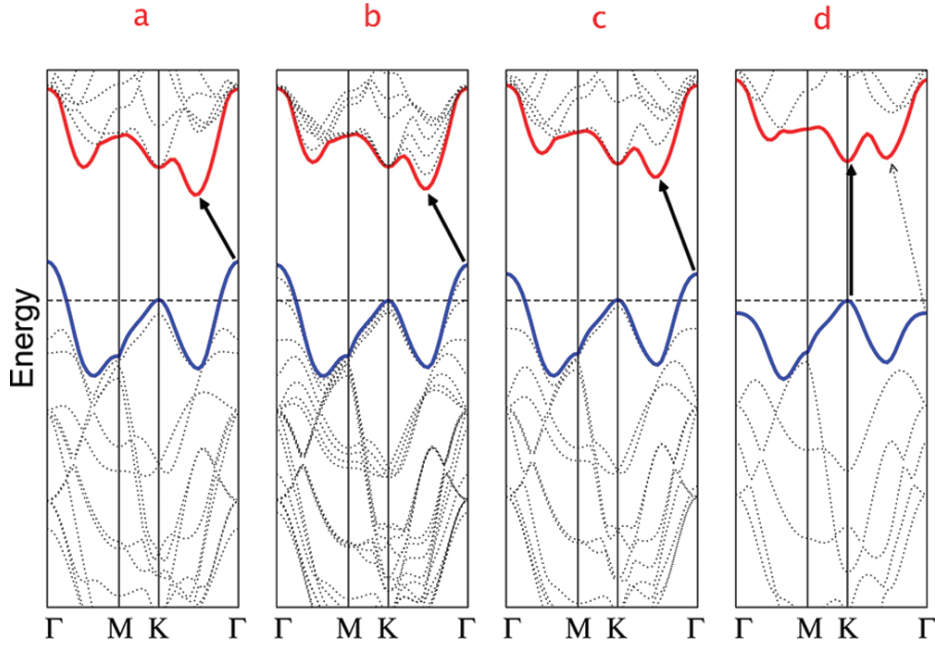


Figure 5.2.1: Calculated band structures of (a) bulk MoS₂, (b) quadrilayer MoS₂, (c) bilayer MoS₂, and (d) monolayer MoS₂. The solid arrows indicate the lowest-energy transitions. From [126].

All TMDs with 2H crystal structure present symmetry points in the band structure. As shown in the inset of Figure 5.2.2, the BZ presents high-symmetry points Γ , M, K and K'. The minima of the conduction band fall at K, K', as well as at Q, Q', approximately halfway along the Γ -K(K') directions. Without the application of an out-of-plane electric field, the relative position of Q and Q' depends on the number of layers and strain. In fact, as previously presented in Figure 5.2.1, the global minimum of the conduction band lays at K/K' in the monolayer MoS₂. Conversely, when the number of layers is greater than 4, the minimum is found at the Q/Q' point. However, applying an electric field that is perpendicular to the MoS₂ plane, the inversion symmetry is broken. Here, the global minimum of the conduction band is shifted to K/K' in any few-layer configuration of the MoS₂. The valleys at K/K' and at Q/Q' are characterized by a different electron-phonon coupling and, when inversion symmetry is broken, by a different spin-orbit coupling [127, 128].

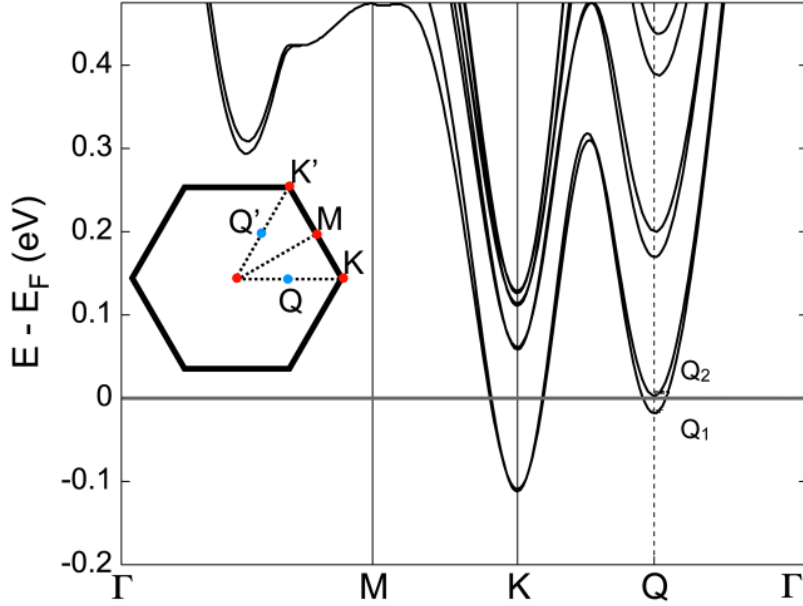


Figure 5.2.2: Electronic band structure of gated 4-layer-MoS₂. The gray line represents the Fermi energy ϵ_F . The inset shows the first BZ of 2H-MoS₂ where the Γ , $K=K'$, and M high symmetry points are highlighted. Adapted from [128].

The ionic-liquid gating technique, described in paragraph 3.2.1.1, has been used to tune the Fermi level, ϵ_F , in TMDs and explore the electric transport at different carrier concentrations [127]. The exploitation of the ultrahigh electric fields attainable at a voltage-polarized electrolyte–electrode interface is used to control the electron and/or hole doping of a material either through simple electrostatic charge induction or more intricate electrochemical effects. Consequently, the Fermi level are modified across the multi-valley electronic band structure of 2H-MoS₂, which exhibits a complicated phase diagram [118].

Electrical transport measurements on MoS₂ FETs in different dielectric configurations show that increasing electron doping, 2H-MoS₂ undergoes an insulator-to-metal transition in monolayer MoS₂ due to strong electron–electron interactions [129]. Moreover, at higher doping levels, a metal-to-superconductor transition happens [130]. As reported in literature [130, 131, 132] and other article there in [118], the superconducting phase can be achieved both through electrostatic carrier accumulation at the surface or electrochemical ion intercalation in the bulk. In the first case, a maximum n-doping density of the order of 10^{14} cm^{-2} was obtained in few-layer-MoS₂. Comparing the experimental results of the previously cited articles, it was found a maximum transition temperature T_c of about 11 K. The highest doping levels also destabilize the 2H-MoS₂ crystal structure, promoting the development of charge density wave (CDW) phases as predicted from

instabilities in the phonon modes and confirmed by direct imaging of the CDW reconstruction in K-doped MoS₂ via low-temperature STM [133]. At the same time, reaching high doping levels could also determine structural transitions to other polytypes [132].

As reported in Chapter 1, it was recently demonstrated that non-volatile charge doping of macroscopic bulk specimens of layered crystals is attainable via gate-driven intercalation of either hydrogen or H-rich organic ions. Whereas, in most of the past literature, the effects of ionic gating vanish when the gate voltage is removed. This new procedure proved its utility to tune the electronic ground state of layered FeSe and enhance its superconducting T_c with respect to that reached through other means of bulk electron doping. In order to investigate the effects of gate-driven organic-ion intercalation in 2H-MoS₂, we decided to follow this road.

5.3 Results and discussion

5.3.1 Electric-Field-Driven Ion Intercalation

2H-MoS₂ crystals (SPI supplies, typical size approx. 2 mm × 1 mm × 50 μm) were obtained through macroscopic cleavage. As mentioned in 3.2.1.1, we employed an ionic gating setup reported in Section Figure 3.1.1 to intercalate hydrogen-rich organic ions into 2H-MoS₂ samples and induce electron doping.

Figure 5.3.1, Figure 5.3.2 and Figure 5.3.3 present the resistivity ρ of three representative MoS₂ samples during the gating process performed at room temperature. These measurements allow us to control the hydrogen or H-rich organic ions loading in our samples. In particular, these figures show gating ramps up to +3.5V but with different release times (0, 4 and 15 minutes, respectively). The release time indicates how long the system remains in the ionic liquid in open circuit (OC) conditions, realized by physically disconnecting the gate electrode from the power source. The study of the resistivity trend in OC conditions allow us to verify if the insertion of H or H-rich organic ions is permanent after the electric-field-driven ion intercalation process. Comparing the three resistivity graphs, it is possible to notice a similar trend which will be described in detail in the following. The measurements were performed *in situ* using the standard four-wire method, as discussed for Pd and PdCu alloy in Chapter 4.

More in detail, in Figure 5.3.1, as V_G is swept from 0 to positive values, ρ remains almost constant ($\sim 0.5 \Omega \text{ cm}$) until V_G reaches the value of +0.4 V (region 1 in Figure 5.3.1). This finite value of resistivity is due to the presence of sulphur vacancies in the MoS₂ crystal. As reported in literature [134], these vacancies originate an intrinsic n-doping by introducing localized states in the bandgap. Then, ρ starts to slowly decrease (region 2 in Figure 5.3.1) up to V_G equal to +3.2 V. Further increasing V_G to +3.5 V we observe a sharp decrease in ρ of about three orders of magnitude, reaching a plateau of 0.16 mΩ cm. This decrease is indicative of the doping process occurring via the electric-field-driven ion intercalation. In

this case, the insertion of H and/or H-rich organic ions brings the sample towards a metallic behaviour, with an increase of the conductivity ($\sigma=1/\rho$).

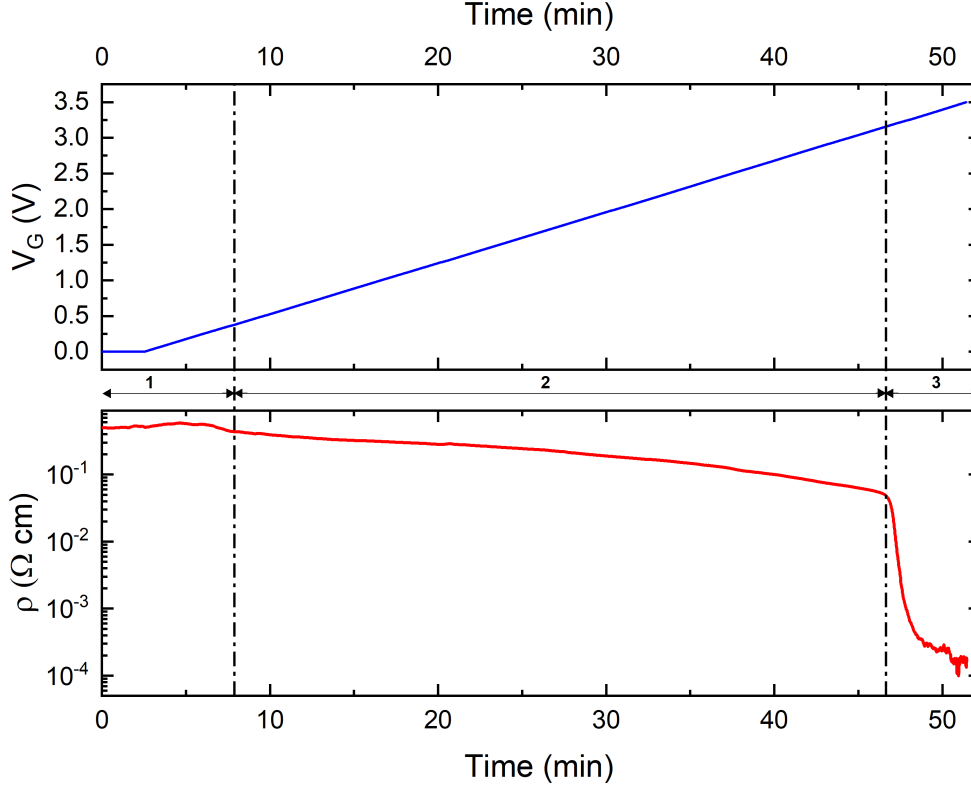


Figure 5.3.1: Gate voltage (upper panel - solid blue line) and resistivity (lower panel - solid red line) measured *in situ* as a function of time during a gating process.

In the following, we report two graphs with increased release time.

Figure 5.3.2, as V_G is swept from 0 to positive values, ρ remains almost constant ($\sim 58 \text{ m}\Omega \text{ cm}$) until V_G reaches the value of +0.1 V (region 1 in Figure 5.3.2). Then, it starts to decrease (region 2 in Figure 5.3.2) reaching a plateau around $35 \text{ m}\Omega \text{ cm}$ in the V_G range around +2.75 V and +3.15 V. Further increasing V_G to +3.5 V we observe a sharp decrease in ρ up to $\sim 5 \text{ m}\Omega \text{ cm}$. Also in this case, we highlight a decrease indicative of the doping process. Here, we kept fixed the V_G at +3.5 V and we observe that the resistivity saturates in around 5 minutes to $\rho \sim 2 \text{ m}\Omega \text{ cm}$. No further change is observed in region 4. Region 5 refers to the OC conditions for 4 minutes and we observe an increase of ρ up to $10.3 \text{ m}\Omega \text{ cm}$. It means that the gate-induced change in ρ previously described is partially volatile.

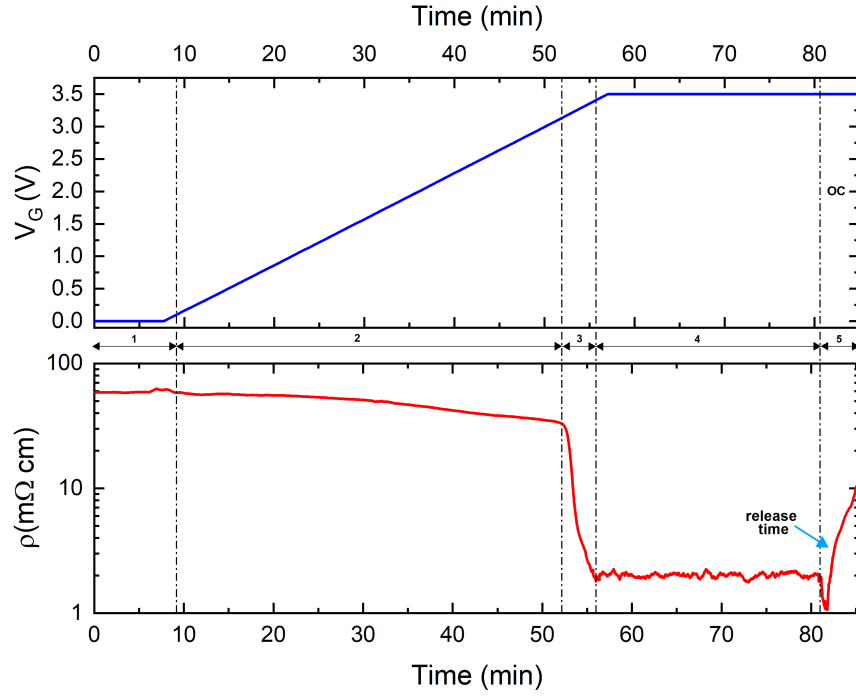


Figure 5.3.2: Gate voltage (upper panel - solid blue line) and resistivity (lower panel - solid red line) measured *in situ* as a function of time during a gating process. Region 5 represents the trend during a release time of 4 minutes.

A further increase of the release time produces the trend shown in Figure 5.3.3. Increasing V_G from 0 to positive values, ρ stays almost constant ($\sim 18 \Omega \text{ cm}$) until V_G reaches the value of +1.5 V (region 1 in Figure 5.3.3). Then, it starts to decrease (region 2 in Figure 5.3.3) reaching a plateau around $5.5 \Omega \text{ cm}$ in the V_G range around +2.75 V and +3.25 V. Further increasing V_G to +3.5 V we observe a sharp decrease in ρ up to $\sim 7 \text{ m}\Omega \text{ cm}$. Again, this is an evidence of the doping process. Then, we kept fixed the V_G at +3.5 V and we observe that the resistivity saturates in less than 10 minutes to $\rho \sim 3 \text{ m}\Omega \text{ cm}$. No further change is observed in region 4. Region 5 refers to the OC conditions, maintained for more than 50 minutes. Here, we observe an increase and a consequent saturation of ρ up to $110 \text{ m}\Omega \text{ cm}$ after 15 minutes.

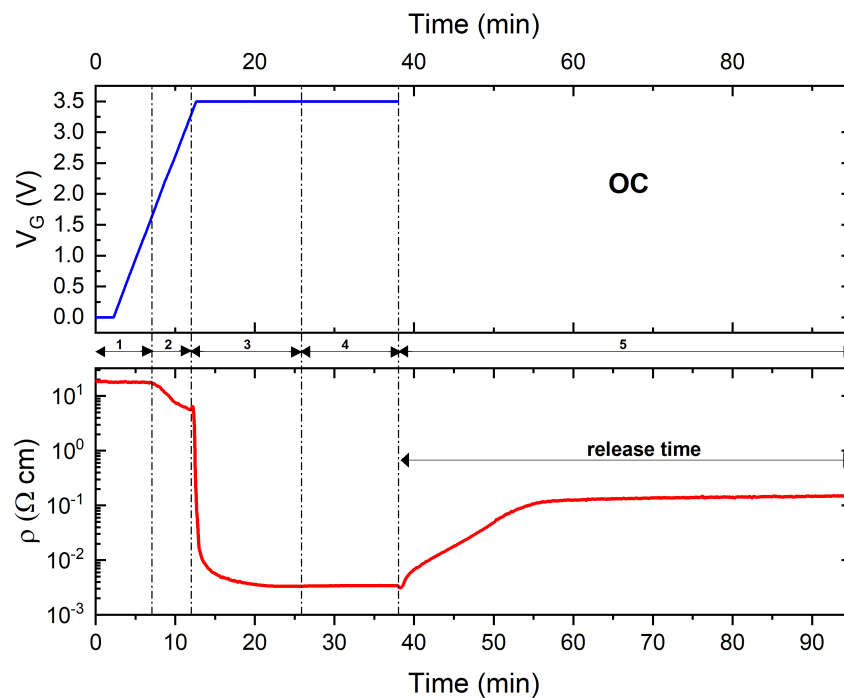


Figure 5.3.3: Gate voltage (upper panel - solid blue line) and resistivity (lower panel - solid red line) measured *in situ* as a function of time during a gating process. Region 5 represents the trend during a release time of 50 minutes.

In conclusion, it is possible to observe that the lowest-resistivity values reached in region 4 (Figure 5.3.2 and Figure 5.3.3) get quite rapidly lost when we switch the system to OC conditions. Nevertheless, extracting the MoS₂ crystal from the cell before complete OC saturation allows us to obtain smaller values of ρ . In Figure 5.3.4 we report the resistivity at room temperature of different representative gated samples of MoS₂ measured *ex situ* as a function of the release time, which shows a monotonically-increasing trend as a function of release time. The stabilisation at intermediate values ranging from ~ 25 m Ω cm to ~ 150 m Ω cm indicates that this technique has brought permanent changes to the crystal.

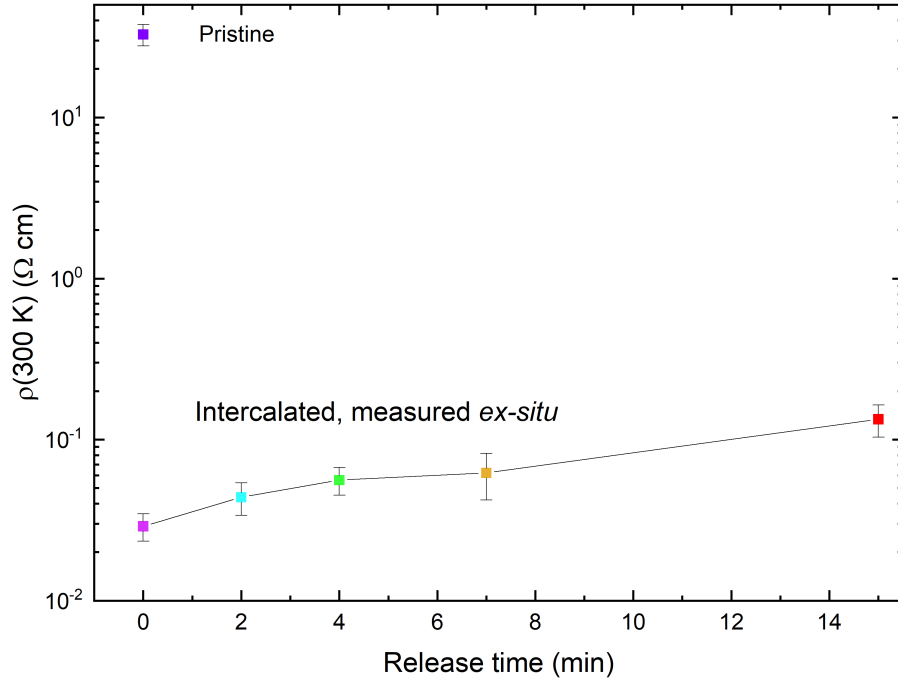


Figure 5.3.4: Resistivity at 300 K measured *ex situ* as a function of the release time.

In the following paragraphs, in order to understand how these changes in resistivity affect the electronic ground state 2H-MoS₂, we report the results of our measurements of electric transport properties as a function of temperature T *ex situ*.

5.3.2 Temperature-dependent resistivity measurements

The resistivity trend as a function of temperature reveals some relevant differences between metals, insulators and semiconductors. Conductivity mainly depends on two factors, namely (1) the availability of free electrons and (2) their capacity of freely moving inside a material.

The typical temperature-dependence of the resistivity of a metallic material was already discussed in Subsection 4.1.1.2.

Regarding the band structure, the electrons inside insulators are not able to escape from the filled valence band (VB) to reach the conduction band (CB), so only a little conduction can be reached (very high resistivity ranging from 10^9 to $10^{20} \Omega \text{ cm}$ [135]).

In semiconductors at absolute zero, the VB is completely full while the CB is

empty. Some free electrons can reach the conduction band due to a small band gap (spanning between ~ 0.5 eV and ~ 2 eV [135]) at higher temperatures. In this case, despite the phonon vibrations still impeding the motion of charge carriers at finite temperatures, more free electrons are available to conduct. In semiconductors, conductivity is mainly affected by this latter factor. Indeed, for a perfect crystal, the resistivity decreases with increasing temperature, contrary to what happens for a metal, as shown in Figure 5.3.5 and expressed by the following proportionality equation

$$\rho \propto T^{-3/2} e^{E_G/k_B T} \quad (5.1)$$

where E_G is the band gap energy and k_B is the Boltzmann constant.

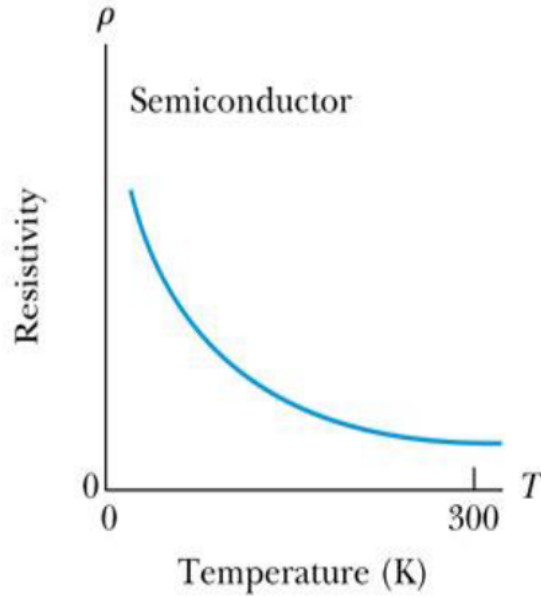


Figure 5.3.5: Temperature dependence of the resistivity in the semiconductor. Adapted from [135].

Doping the material, for example introducing H^+ or H-rich organic ions to pure intrinsic semiconductors, it is possible to activate the transition from intrinsic semiconductor, through extrinsic semiconductor (which exhibit a nonlinear relationship between current and voltage [136]), degenerate semiconductor, and finally metal.

However, if there are defects and sub-gap states, this dependence is not valid because hopping phenomena dominate. In natural MoS_2 (like our samples), hopping dominates in states located at the bottom of the CB. In order to describe the low temperature in disordered systems with localized charge-carrier states we can consider the temperature dependence of resistivity with the Mott variable-range hopping equation which presents the following characteristic temperature dependence for 2D materials [137, 138, 139]:

$$\rho = \rho_0 \exp\left(\frac{T_0}{T}\right)^{1/3} \quad (5.2)$$

In the following paragraphs, we report the results of our measurements of electric transport properties as a function of temperature T on our MoS_2 sample before and after the ion intercalation.

Figure 5.3.6 displays the temperature-dependence of ρ , normalized by its value at $T = 300$ K (already reported in Figure 5.3.4), measured in a cryocooler from room temperature down to 3 K, both for the pristine material and for a succession of intercalated MoS_2 crystals with increasing release times.

Starting the description from the pristine material (solid dark purple line), the trend is exponentially-increasing ρ with decreasing T , as seen for semiconductor materials. According to the literature [134, 140], this behaviour could be also ascribed to the insulator material where conduction occurs via hopping processes in the localized states in the band tails.

The T -dependence of ρ in the intercalated samples is less sharp. We notice that, at low T , the normalized resistivity values are at least three orders of magnitude lower than that of the pure sample. This behaviour is due to a metallization process induced by electron doping. When release time is low we can find a match with the metallic behaviour shown in 4.1.1.2. In fact, we can distinguish a residual and a thermal component of the resistivity. Anyway, the curves with a release time of 0 min (solid purple curve) and 2 min (solid light blue curve) present an anomaly that is not totally in agreement with the T -monotonic dependence of resistivity in metals. Instead, we can observe that for a release time equal to 4 minutes (solid green curve) the graph has a smoother trend that is discussed in the following paragraphs.

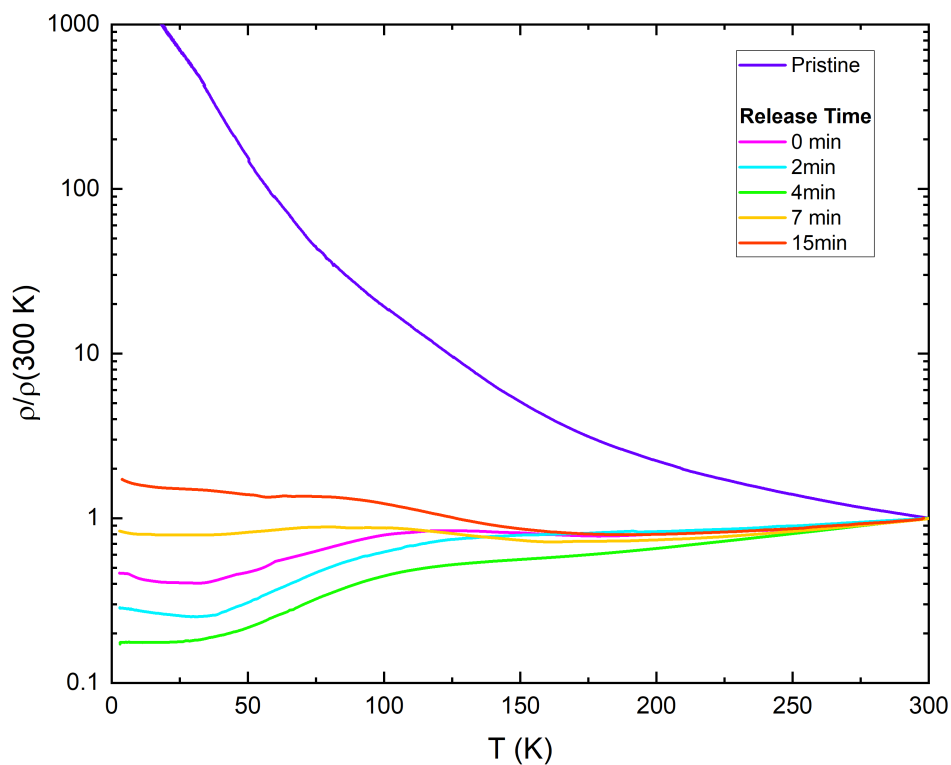


Figure 5.3.6: Temperature dependence of the resistivity ρ divided by its value at 300 K, before and after electric-field-driven ion intercalation, in semi-log scale.

A closer inspection of the curves for the intercalated samples is present in Figure 5.3.7. Focusing on the sample at zero nominal release time (solid pink line), we observe that its ρ decreases by almost a factor of 2 going down in temperature from 300K to 3K. The same behaviour is also present in the remaining curves. Nonetheless, this T-dependence is not monotonic: approximately between 50 and 150 K, an evident anomaly can be observed in the form of a broad hump. This overall trend reveals a complex dependency of ρ on both T and release time.

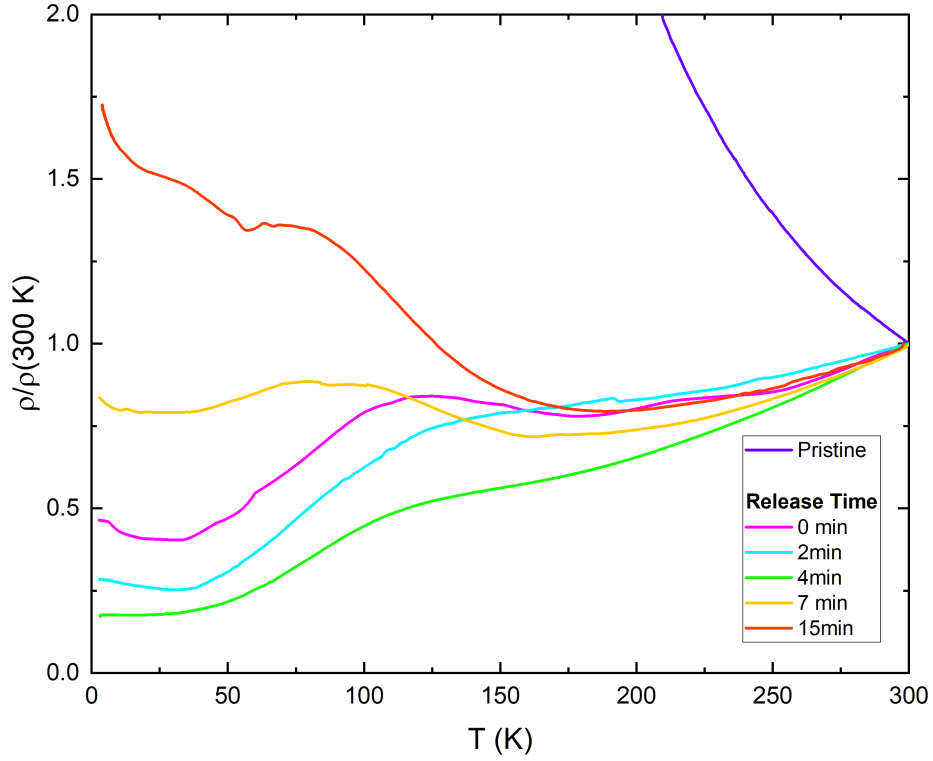


Figure 5.3.7: Temperature dependence of the resistivity ρ divided by its value at 300 K, before and after electric-field-driven ion intercalation, in linear scale.

To better understand this behaviour, we plotted the first derivative of the resistivity with respect to the temperature, i.e. $d\rho/dT$. These curves, displayed in Figure 5.3.8, were obtained by numerical derivation of the curves in Figure 5.3.7, using the derivative tool of Origin. Here, we can notice that this anomaly gives rise to a hump-dip structure in the T-dependence of $d\rho/dT$. More in detail, we can distinguish two peculiar regions: the first with a broad hump at lower T (approximately between 25 and 75 K) and the second one with a sharp dip at higher T. The temperature values associated with this latter are marked with dashed lines and arrows. Moreover, observing the graph at T less than 20 K, we recognize a small resistance upturn. This evidence indicates that at low T, some degree of carrier localization is present in the sample. Real solid-state materials frequently exhibit this phenomenon because of lattice disorder, impurities, and other imperfections such as defects and deep centres. As a result, it significantly affects the materials' electrical and optical properties [141].

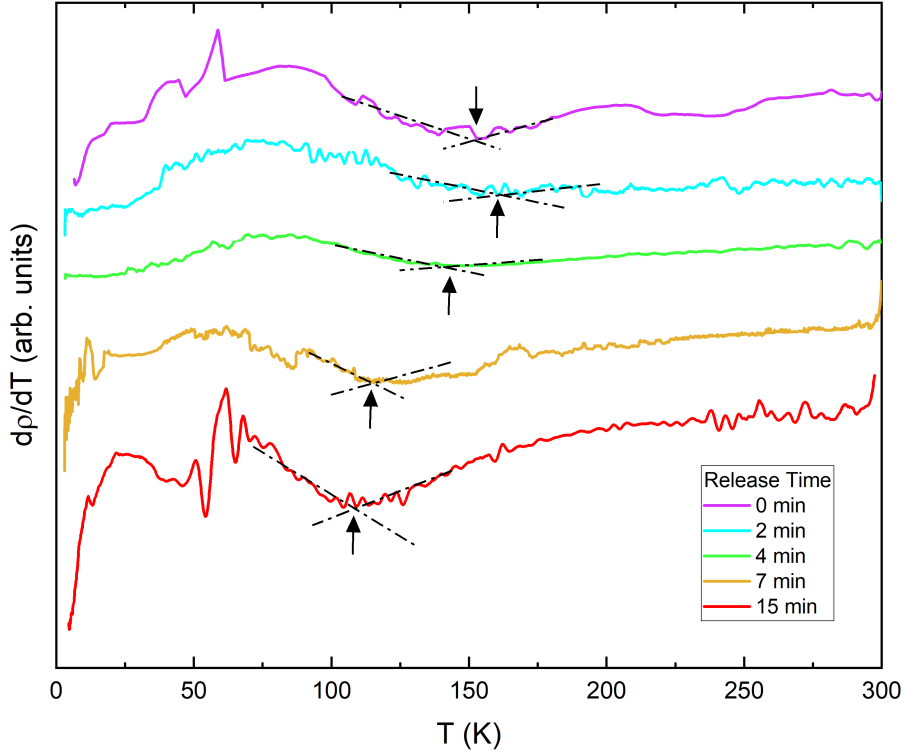


Figure 5.3.8: T dependence of $d\rho/dT$, before and after ion-intercalation, obtained by numerical derivation of the curves in Figure 5.3.7. Arrows highlight the values of T where $d\rho/dT$ shows a dip (T^*). The curves are vertically offset for clarity.

So, the resistivity anomaly and the degree of metallicity are two of the main features of the system under investigation. In order to track their evolution on the increasing release time, we defined two distinct figures of merit: for the resistivity anomaly, the temperature T^* where the dip in $d\rho/dT$ is located; for the metallicity, the residual resistivity ratio RRR, defined as $\rho(300\text{ K})/\rho(3\text{ K})$. This latter parameter allows us to quantify the overall level of impurities in our samples. It can vary rather significantly for a single material depending on the number of impurities and other crystallographic defects. Since resistivity typically rises as defect prevalence increases, a high RRR is linked to a pure sample [142].

Figure 5.3.9 shows these two parameters in function of the release time. Focusing on the left scale, which refers to T^* (blue squares), we observe that upon increasing the release time (i.e., decreasing the electron doping), it decreases with a nearly monotonic trend from about 155 K at release times below ~ 2 min to 115 K at release times of almost 15 min. In contrast, RRR (red diamonds, right scale) behaves in a non-monotonic fashion. Indeed, we can observe an initial increase from 2.7 to 5.7 for release times lower than 4 min, and a subsequent strong decrease down to 0.58 at release times greater than 15 min, i.e., when spontaneous deinter-

tercalation of the intercalated ions stops (Figure 5.3.3). This indicates that the intercalated phase obtained with a release time of 4 min achieves a maximum degree of metallicity, and doping the sample away from it shifts the system towards an insulating behaviour.

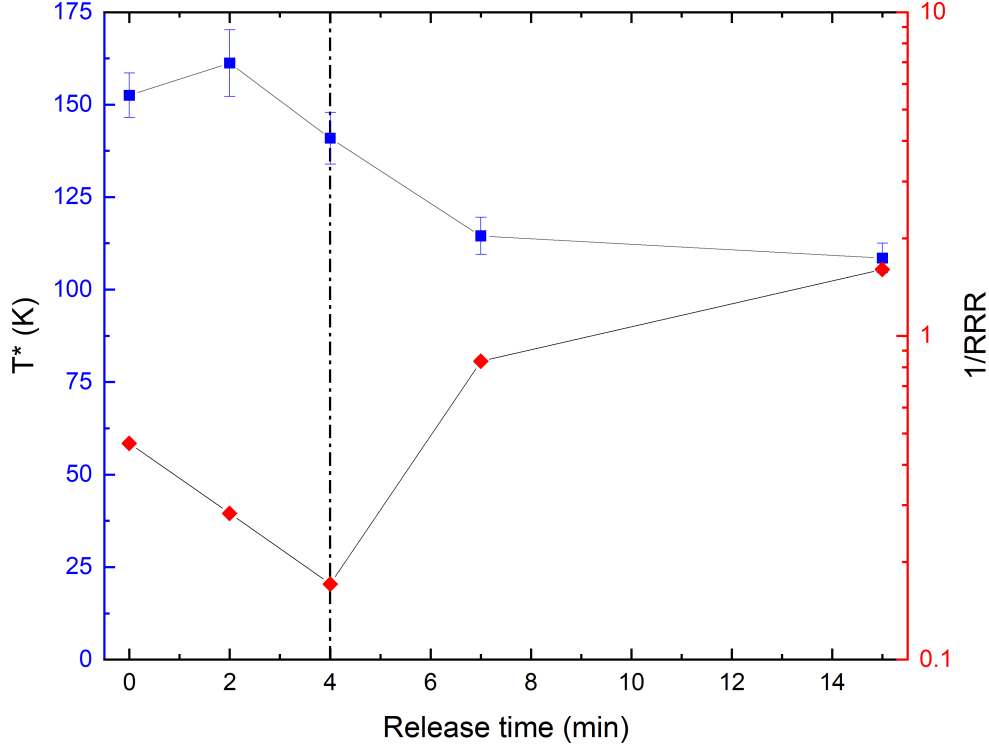


Figure 5.3.9: T^* (blue squares, left scale) and inverse residual resistivity ratio $1/RRR$ (red diamonds, right scale) as a function of the release time.

The main result emerging from the resistivity measurements is that increasing the release time promotes the leakage of the dopant. In this way, the intercalated samples tend to assume again the behaviour of the pristine material, namely the state of a band insulator. On the contrary, the release time reduction causes an increase in the doping level. We would expect that increasing the concentration of dopants improved the material's conductivity since the dopant acts like a source of free electrons to the conduction band. That does not happen in our case, and we observe a trend typical of an insulating state that must have a clearly different cause, which must be due to some localization phenomena.

We identify two main sources of localization phenomena:

The first one could be associated with the random ions intercalation inside the lattice. These ions act as extra scattering centres, increasing the disorder degree of the whole crystalline structure [26, 36, 143, 144, 145, 146]. Several authors

observed this kind of gate-driven re-entrant transition (from a band insulator to a metal and finally to an Anderson insulator) for other ion-gated TMDs [147, 148, 149] and oxides [150].

A second source, already observed in literature to justify resistivity anomalies appearing for TMDs, could be associated with the onset of charge density wave (CDW) phases.

CDWs are collective fundamental states emerging from a periodic modulation of the charge carrier density, which can be commensurate or incommensurate with the lattice spacing and distortion of the underlying crystal structure [112, 149, 151, 152]. CDW is favoured by Fermi surface nesting and/or strong electron-phonon interaction. Briefly, a crystal lattice distortion and the opening of a gap at the Fermi surface accompany the formation of a CDW and stabilize it by lowering the energy. As reported in the literature, the presence of the gap gives the material insulating properties if the entire Fermi surface is gapped; if the Fermi surface is only partially gapped, the material remains metallic albeit with a reduced density of states at the Fermi level. Sufficiently high doping of material can disable the nesting and destabilizes the CDW, thereby converting the material to metal and, in some cases, making it superconducting. That happens in most TMD materials, where the charge carrier doping impacts CDW phases in two ways. Firstly, by increasing the doping, we may observe the CDWs' suppression and promotion of the development of superconducting phases. In certain compounds, however, doping boosts the CDW order. This latter has an opposite effect with respect to SC, but the two phenomena can coexist. Despite both of them being broken-symmetry states that need electron-electron interaction mediated by phonons, and both of them being generated by instabilities of the Fermi surface (nesting, gap), CDW and SC show complementary effects on the electric conductivity of the material. CDWs, induced by a charge redistribution, can cause the emergence of a semiconducting gap and a non-conducting state, while the onset of SC order induces an infinite DC conductivity in the material [112, 151, 152].

Concerning 2H-MoS₂, first-principles calculations in the bulk [153, 154] and in the monolayer [132, 155] form, have shown that doping promotes the CDW order. Previous experimental studies report that the onset of a CDW order in MoS₂ bulk crystals and bulk-like flakes can be promoted by three main factors: Li-doping [127], K-doping [133], and pressure [156].

Consequently, our T* (reported in Figure 5.3.9) would indicate the critical transition temperature for the CDW phase in our intercalated MoS₂, placing it in an intermediate range between those of Li_xMoS₂ (≈ 230 K) and K_xMoS₂ (≈ 85 K).

The instauration of CDW order could justify resistivity anomalies emerging in our intercalated MoS₂ crystals. Moreover, it could provide a further explanation for the incipient high-doping localization. As described before, this determines the opening of a (possibly partial) gap on the Fermi surface, generating insulating properties in the material [154, 133].

However, performing resistivity measurements down to 2.8 K, we have not detected any sign of superconductivity in our intercalated samples. On the contrary, this happens in Li^+ or K^+ doped MoS_2 . As reported in the literature [157, 133], K-intercalated MoS_2 presents a T_{CDW} at a low temperature and shows a bulk superconductivity with a T_c around 7 K, depending on the exact dopant content. In the case of Li_xMoS_2 , the onset of the CDW is at a higher temperature than the in the K-doped compound. In particular, only samples not exhibiting CDW-related resistivity anomalies present superconductivity at $T_c=3.7$ K [36]. In our case, the CDW order is present at any doping content, manifesting at intermediate temperatures. One of the hypotheses that could explain the absence of superconductivity could be the wideness of the range of doping level reached during the ion intercalation, as better described in the following Chapter.

In conclusion, considering the success in inducing a transition from the insulating to the metallic phase in intercalated 2H- MoS_2 , we decided to perform an extended investigation of the electronic and vibrational properties of both the pristine and intercalated compounds to assess whether ionic species that was intercalated into the material, were H^+ or H-rich organic ions originating from the IL, as discussed in Chapter 6.

Chapter 6

Other Techniques

6.1 Vibrational spectroscopy

The main spectroscopies used to detect vibrations in molecules are based on the processes of Raman scattering and infrared (IR) absorption spectroscopy. Raman spectroscopy relies on inelastic scattering of photons, whereas IR spectroscopy is based on the absorption of infrared light that implies the direct transition among vibrational energy levels of molecules. Although the information contained in the vibrational Raman spectrum and that contained in the IR spectrum are equivalent, the two spectra are quite different in terms of specificity due to different selection rules [158]. Specifically, when the dipole moment changes, vibrations become IR active, but the development of Raman bands depends on the change in polarizability [159]. So, these two techniques can be considered complementary and are broadly employed to provide information on chemical structures and physical forms, to identify substances from the typical spectral patterns and to determine quantitatively or semi-quantitatively the amount of a substance in a sample.

6.1.1 Raman spectroscopy

Raman spectroscopy relies on the inelastic Raman scattering of light by a material, which is different from the more noticeable elastic Rayleigh scattering [160]. Indeed, when a sample is exposed to monochromatic radiation of frequency (ν_0), some of the radiation scatters. There are two types of radiation observed in the scattered radiation: elastically scattered radiation, also known as Rayleigh radiation, which has the same frequency ν_0 of the incident radiation, and inelastically scattered radiation, also known as Raman radiation, which instead exhibits a different ν [158].

Referring to Figure 6.1.1, when a photon collides with a molecule through Rayleigh scattering, the electron cloud becomes polarised and is elevated to a state of "virtual" energy. After a very short time ($\sim 10^{-14}$ seconds), the molecule returns to its ground state, emitting a photon. The scatterer and the scattered light

do not exchange any energy throughout this process. As a result, the scattered photon has the same energy before and after scattering, and its corresponding wave has the same frequency, though its direction of propagation may have altered [160, 161]. In contrast, Raman scattering is inelastic. That means that the kinetic energy of an incident photon is increased or reduced during the interaction. Consequently, the frequency of the scattered photon is different compared to the incident photon. More precisely, as shown in the Figure 6.1.1, the scattered photon will have a larger wavelength than the incident photon if the molecule is promoted from a ground state to a virtual one and subsequently drops back down to a (higher energy) vibrational state. That is the so-called Stokes scattering. Otherwise, the scattered photon will have a shorter wavelength if the molecule was initially in a vibrating state and is now in its ground state as a result of scattering, more commonly known as anti-Stokes scattering. Due of its higher intensity, the Stokes half of the spectrum is typically the sole one employed in Raman spectroscopy [160, 158].

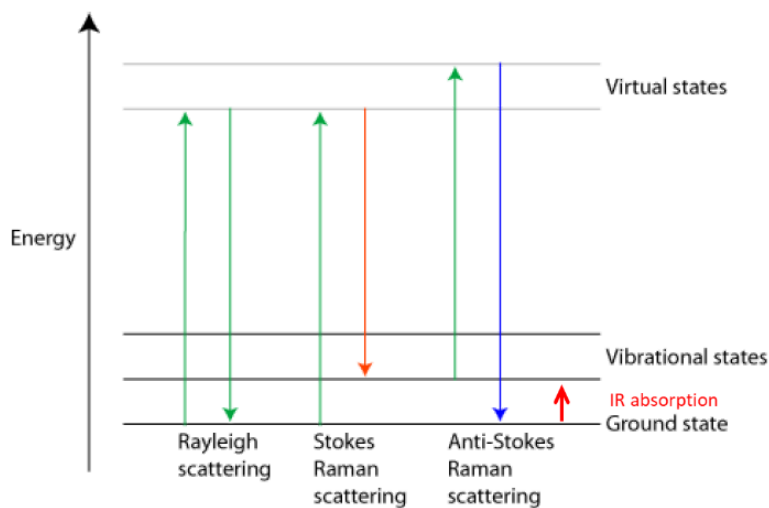


Figure 6.1.1: Energy-level diagram showing the states involved in Raman spectra. Adapted from [160].

So, this inelastic scattering causes shifts in wavelength, which can then be used to deduce information about the material and about the typical vibration spectrum of its atoms. Properties of the material can be determined by analysis of the spectrum or comparing it with a library of known spectra to identify a substance.

A common setup of the Raman spectrometer is shown in Figure 6.1.2.

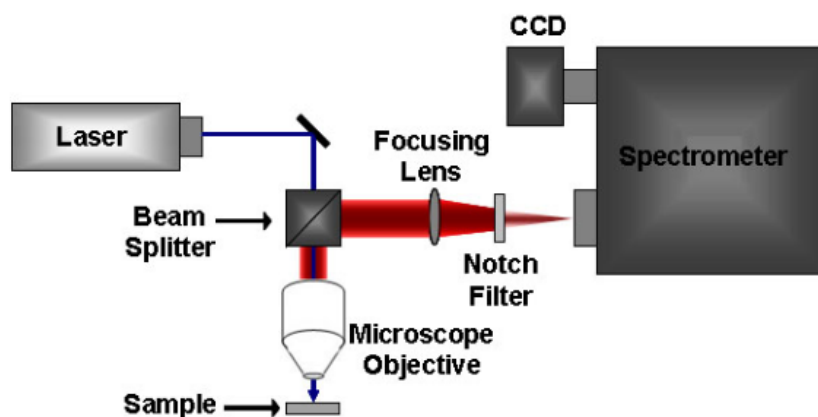


Figure 6.1.2: Schematic of a Raman. From [162].

6.1.2 Infrared Spectroscopy

Most molecules absorb light in the infrared region of the electromagnetic spectrum, turning it into molecular vibrations, which is the basis for infrared (IR) spectroscopy. Using a spectrometer it is possible to measure absorption as a function of wavelength (as wave numbers, typically from $4000 - 600 \text{ cm}^{-1}$). The outcome is an IR spectrum that may be used to distinguish between organic and inorganic materials thanks to its distinctive "molecular fingerprint" [163].

As shown in Figure 6.1.3, traditional infrared spectrometers, also known as dispersive infrared spectrometers, use two beams of radiation: one passes through the sample, the other through a reference cell, using a monochromator to select radiation of only one frequency at a time.

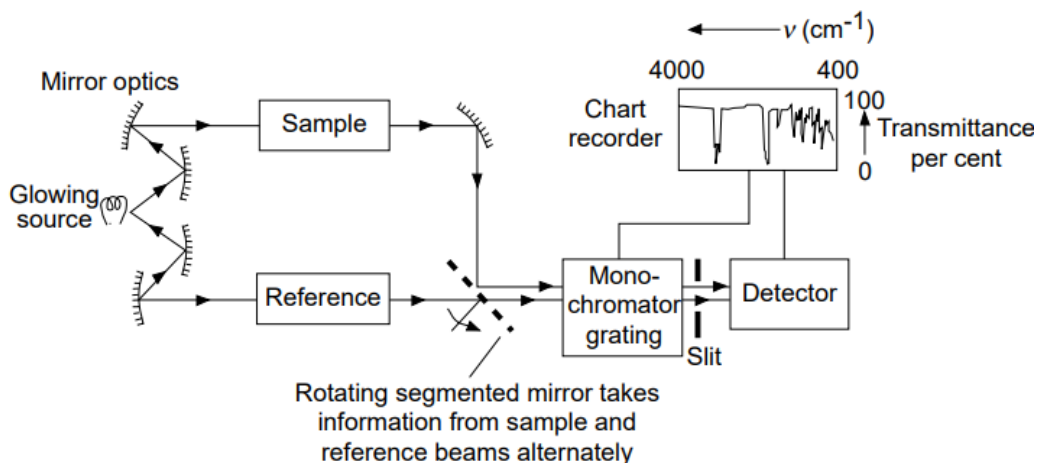


Figure 6.1.3: Schematic diagram showing the working principle of an dispersive IR spectrocomer. From [164].

Another method is called Fourier-transform infrared (FT-IR), and it uses just

one beam, allowing all necessary frequencies to travel through the device simultaneously. So, via this technique it is possible to collect the spectral data of all wavelengths in a single pass. As sketched in Figure 6.1.4, a continuous source generates IR light over a wide range of infrared wavelengths.

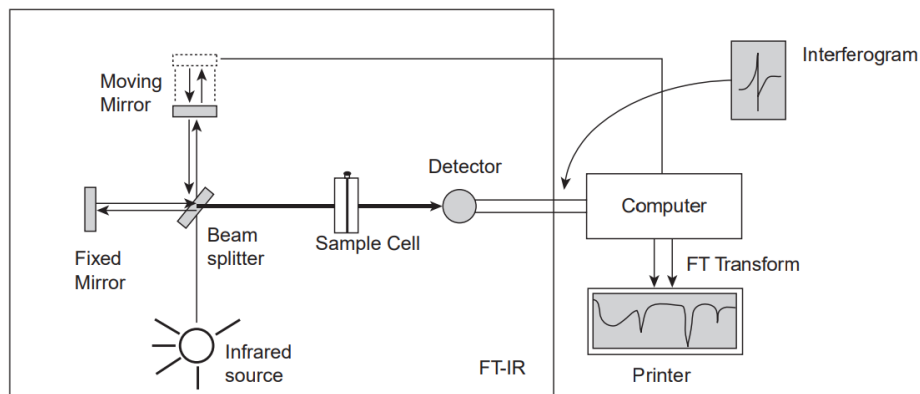


Figure 6.1.4: Schematic block diagram showing the working principle of an FT-IR spectrometer. From [165].

The infrared light then passes through an interferometer and is then directed at the sample. Differently from the dispersive measurements, we first acquire an interferogram. This latter is a raw signal, representing the light intensity as a function of the position of a mirror inside the interferometer. Then, it is necessary to translate it into an IR spectrum, where the intensity is plotted against the wave number via the Fourier transform. FT-IR presents several advantages compared to the conventional infrared. First of all, the acquisition of FT-IR spectra is much faster (few seconds). Moreover, the sensitivity of the technique is greater because the ‘background noise’ is at a much lower level [163, 164].

6.1.3 Material and methods

Both Raman and Fourier-Transform Infrared (FT-IR) spectroscopy were performed on the MoS₂ samples before and after ion intercalation. We performed FT-IR also on the ionic liquid to compare peaks. A micro-Raman spectrometer (InViaH43662 - Renishaw) was used to collect Raman spectra (see Figure 6.1.5). An excitation wavelength of 514 nm, a laser power of less than 1 mW focused through a 100X objective, an exposure time of 20 s, and 50 accumulations were used to acquire all spectra.

It is relevant to point out the main function of the parameters we have imposed, namely [166]:

- *Laser Power* is the percentage of maximum laser power that will be used for the scan. A better signal-to noise ratio can be obtained using higher power, which can damage some samples, depending on the laser used;

-
- The *objective* denotes the magnification of the chosen objective. Higher magnification objectives typically produce a better signal-to-noise ratio because they produce a higher power density at the sample;
 - The term *exposure time* refers to the length of time the detector is exposed to the Raman signal. Better spectral signal-to-noise ratios are obtained with longer exposure periods; however, excessive exposure time can result in sample overheating and/or detector saturation;
 - The quantity of scan repetitions is known as *accumulations*. Automatic co-adding of the accumulations results in spectra with improved signal-to-noise ratios. Additionally, performing numerous accumulations of a short scan may be more advantageous than doing a single long scan.

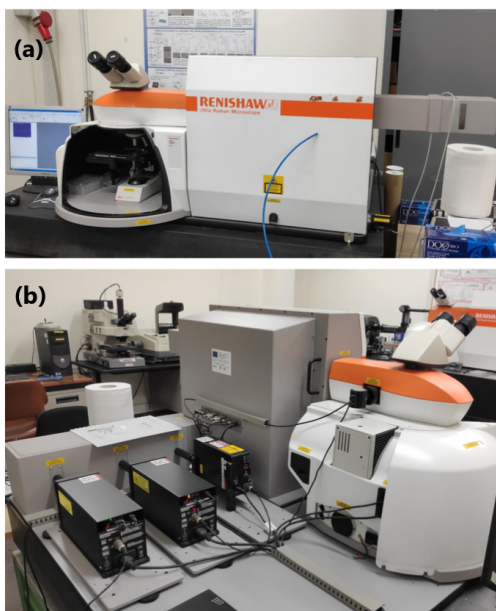


Figure 6.1.5: Micro-Raman spectrometer was used to collect Raman spectra

A Nicolet 5700 spectrometer (ThermoScientific - Figure 6.1.6) was used to measure FT-IR spectra in the range of 900 to 3500 cm^{-1} in attenuated total reflectance (ATR) mode. ATR sampling technique introduces light onto a sample to obtain structural and compositional information. In this method, the measurement path-length is not affected by the sample thickness. ATR is an internal reflection-based method, and the sample pathlength is influenced by the depth of penetration of the infrared energy into the sample [167].



Figure 6.1.6: Nicolet 5700 spectrometer used to measure FT-IR spectra

6.2 Scanning microscopy techniques

Scanning microscopy techniques allow us to detect defects, structures, elemental and chemical composition and morphology of thin (two dimensional, 2D) samples or surfaces, comprising internal or fracture sections of 3D samples, at the nanometric level [168]. The main microscopy techniques of this category include, scanning electron microscopy and scanning probe microscopies (SPM).

More specifically, SPM is a group of techniques used in the characterization of nanostructures with atomic or subatomic spatial resolution, including atomic force microscopy (AFM). SPM analyses the interaction between the sample and a small tip acting as a probe, by placing this probe tip close to the sample and collecting data pixel by pixel during a raster scan over the sample's surface. The resulting image can be presented into a two-dimensional (2D) or a three-dimensional (3D) display. The surface of materials can be directly characterized using SPM techniques with high spatial resolution without a laborious sample preparation procedure. They make it possible to observe things at the nanoscale, making them ideal for characterizing the structure of nanomaterials [169].

6.2.1 Atomic Force Microscopy

Atomic force microscopy (AFM) is a popular nanoscale imaging technique which provides high spatial resolution topographic maps of the surface of a sample.

AFM is made of a sharp tip with a minimum diameter (at the apex of the tip) approximately of 10 to 20 nm attached to a stiff cantilever. These two components are usually micro-fabricated from Si or Si_3N_4 . The movement of the tip depends on the tip-surface interactions, and it is measured by focusing a laser beam on the reflecting region in the back of the cantilever and collecting the reflected light by a photodiode. When the tip is brought close to the sample, a number of forces may operate. These latter combine in an resultant interaction as shown in the force-distance curve represented in Figure 6.2.1 [170, 171].

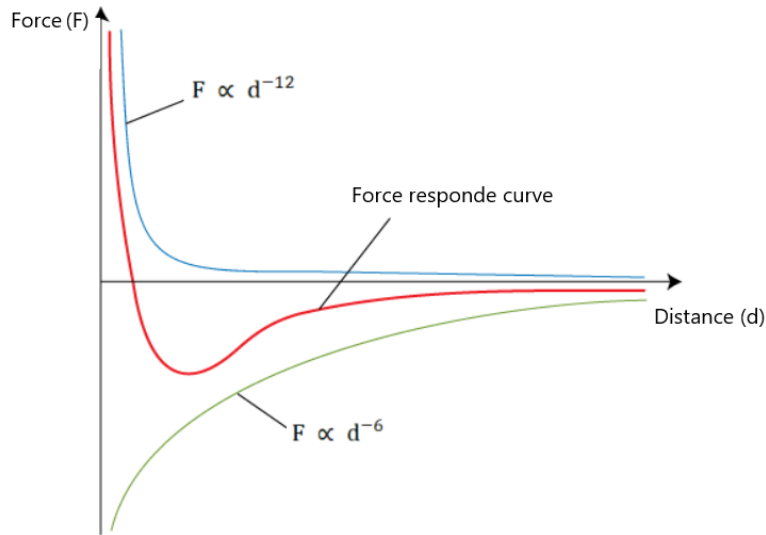


Figure 6.2.1: Plot of forces as function of distance. From [170].

AFM operates in three basic different modes, namely contact mode, tapping mode and non-contact mode. These three are briefly described and compared in the following Table 6.1.

	Working Principles	Advantages	Disadvantages
Contact Mode	AFM tip is in continuous contact with the surface. It is used for force-curve measurements.	<ul style="list-style-type: none"> • High scan speeds • High resolution • Rough samples with extreme changes in vertical topography can sometimes be scanned more easily 	<ul style="list-style-type: none"> • Lateral (shear) forces may distort features in the image • Combination of lateral and strong normal forces reduce resolution and mean that the tip may damage the sample, or vice versa
Tapping Mode	AFM cantilever is vibrated above the sample surface such that the tip is only in intermittent and short contact with the surface. Cantilever oscillates at or slightly below its resonant frequency. The amplitude of oscillation typically ranges from 20 nm to 100 nm.	<ul style="list-style-type: none"> • Lateral forces almost eliminated • Higher lateral resolution on most samples • Lower forces so less damage to soft samples or tips 	<ul style="list-style-type: none"> • Slower scan speed than in contact mode
Non-contact Mode	In non-contact mode the cantilever oscillates near the surface of the sample but does not contact it. The oscillation is at slightly above the resonant frequency.	<ul style="list-style-type: none"> • Low resolution • Both normal and lateral forces are minimized, so good for measurement of very soft samples • No damage to sample • Can get atomic resolution in ultra-high vacuum environment. 	<ul style="list-style-type: none"> • Slower scan speed than tapping and contact modes

Table 6.1: Overview of AFM modes operation. Adapted from [170, 171].

6.2.2 Nano-Infrared Microscopy

As discussed in the previous section 6.1.2, the infrared spectral region is notably interesting because of the presence of material-specific absorption lines. Traditional methods, e.g. FT-IR, have high spectral resolution, but are diffraction limited to large spatial resolutions between 3–75 μm , depending on the technique used. Whereas, for what concerns the AFM, spatial resolution on the nanoscale can regularly be attained. However, the radius of the apex of the AFM probe tip represents the only physical restriction on the spatial resolution of AFM. Indeed, commercially available AFM tips typically attain spatial resolution on length scales below 20 nm, and in some circumstances, down to the atomic and molecular level. However, the AFM does not have any inherent capacity to distinguish materials based on their chemical composition [172, 173].

Alternatively, nanoscale IR spectroscopy/imaging allows overcoming these limitations offering a spectral detection with high spatial resolution beyond optical diffraction limit via AFM-based techniques coupled with optical illumination. As shown in Figure 6.2.2, AFM-IR uses the tip of an AFM to locally detect the thermal expansion of a sample resulting from local absorption of IR radiation. So, the AFM tip itself acts as the IR detector.

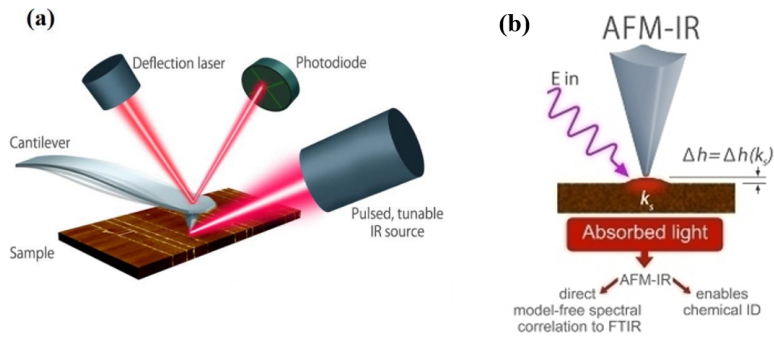


Figure 6.2.2: (a) schematic diagram of classical AFM-IR. A pulse tunable laser source illuminates a sample at an angle above the tip of AFM cantilever; (b) AFM-IR working principle. Adapted from [172, 174]

One of the new developments, known as Tapping AFM-IR, allows acquisition of IR images at a specific absorption band simultaneously with sample topography and nano-mechanical properties, providing a complete set of topographical, chemical and mechanical insights with a below 10 nm spatial resolution [175, 174].

6.2.2.1 Materials and methods

The acquisition of scanning probe microscopy images was executed on freshly-cleaved surfaces on MoS_2 samples before and after ion intercalation in ambient conditions. The instrument used was an Anasys nanoIR3-s atomic force micro-

scope (AFM) by Bruker (see Figure 6.2.3), pictured in Figure 6.2.3, combined with a multichip tunable quantum cascade laser (QCL; MIRcat-QT Daylight Solutions). During the analysis, the AFM was equipped with commercial gold-coated silicon tips (Bruker PREX-TnIR-A). The IR spectral ranges covered were $1900 - 1350 \text{ cm}^{-1}$ and $1150 - 900 \text{ cm}^{-1}$. Tapping mode was used to acquire AFM topography maps. Moreover, using the “Tapping AFM-IR” mode of the built-in Analysis Studio software, it was possible to record the IR absorption maps by heterodyne detection.

Heterodyne technique is a powerful detection method to achieve high resolution information, such as modulation of the phase, frequency or both of electromagnetic radiation in the wavelength band of visible or infrared light. The light signal is compared with a reference one with a fixed offset in frequency (or eventually, phase) emitted by a "local oscillator". In particular, the weak input signal is mixed with some waves generated by the local oscillator. The resulting mixing product is then detected, often after a filtering step of the original signal and the local oscillator frequency. The frequency of this resulting wave is the sum (or the difference) of the frequencies of the input and of the local oscillator [176, 177].

To enable heterodyne detection of the IR signal amplitude, all maps were obtained at a pulse rate of 300 kHz, a duty cycle of 15%, and a laser power of 60% of the average QCL laser (0.5 W). Finally, the absorption spectra was collected by setting a spectral resolution of 2 cm^{-1} and 64 co-averages and normalising them to the QCL emission profile at the same laser power.



Figure 6.2.3: Anasys nanoIR3-s atomic force microscope.

6.2.3 Kelvin-Probe Force Microscopy

Kelvin probe force microscopy (KPFM), also known as surface potential microscopy was introduced as a tool to measure the local contact potential difference (CPD) between a conducting atomic force microscopy (AFM) tip and the sample, thereby mapping the work function or surface potential of the sample with high spatial resolution [178, 179]. More properly, the work function (ϕ) is the minimum energy (or work, usually measured in eV), needed to remove an electron from a solid, to a point immediately outside the solid surface (or energy needed to move an electron from the Fermi level into vacuum). Thus, this is a surface property

and not related to the bulk [179, 180]. So, CPD (V_{CPD}), i.e. the surface potential, between a conducting AFM tip and the sample is given by

$$V_{CPD} = \frac{\phi_{tip} - \phi_{sample}}{-e} \quad (6.1)$$

where ϕ_{tip} and ϕ_{sample} are the work function of the sample and tip, respectively; and e is the electron charge. Due to the differences in their Fermi energies, an electrical force is created between an AFM tip and sample surface when it is brought close to the surface of the sample [178].

To measure the CPD between the surface and the cantilever, an AC voltage is given to the cantilever at a frequency significantly below the resonance frequency. As a result, there is an oscillating electrostatic force between the tip and the sample, which is detected by a second internal lock in amplifier in the controller. Then, to counteract the cantilever oscillation at the AC frequency, an additional DC offset voltage is supplied to the AC voltage. As the tip is moved across the surface, the applied DC offset voltage (applied to keep at zero the oscillation at AC frequency) is recorded, and a representation of the CPD is created [179].

There are two working modes for KPFM: single or dual pass mode. In the first one, the topography and CPD are simultaneously recorded while the cantilever is passing over each line of the surface. In the dual pass setup, also known as Lift Mode surface potential Imaging or Amplitude Modulated KPFM (AM-KPFM, see Figure 6.2.4), the cantilever passes twice over every line in the sample. In the first pass, the surface topography is obtained via standard Tapping Mode AFM, while the surface potential is measured on the second pass with the tip lifted over the surface and the topography measured immediately before retraced in order to remove the effects of the interaction tip-sample topography. Although AM-KPFM requires longer acquisition time than the single pass method, the advantage is less edge and boundary effect and less noisy images. Moreover, by reducing the oscillation of the cantilever during the second step, the lift height can be reduced, improving the KPFM contrast [179, 181].

6.2.3.1 Materials and methods

We collected surface-potential maps using the Innova (Bruker) AFM (Figure 6.2.5a) on the freshly-cleaved MoS₂ sample's surface in ambient conditions. During the characterization, pristine and intercalated samples were fixed simultaneously on the same metallic sample holder, using a specific electrically-conducting adhesive tape (Figure 6.2.5b). This AFM is equipped with specific tools for surface potential imaging through standard platinum-iridium-covered silicon tips (Bruker SCM-PIT-V2) (Figure 6.2.5c). We acquired AFM topography maps in tapping mode during the forward scans, whereas we performed Kelvin-probe force microscopy (KPFM) measurements in lift mode during the backward scan by grounding the sample and biasing the KPFM tip. The images acquired, shown in Chapter 6,

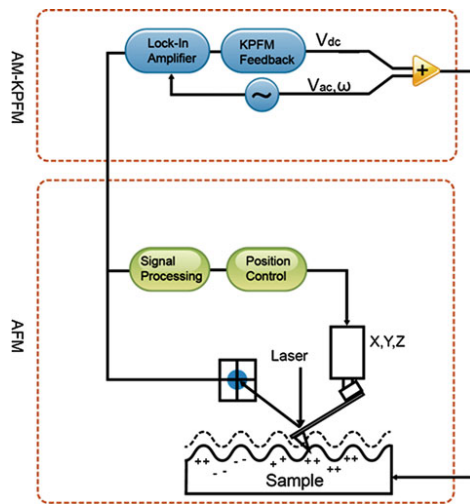


Figure 6.2.4: Schematic diagram of AM-KPFM. From [182].

were obtained using a scan rate of 0.3 Hz, a lift height of 50 nm and a tip AC bias voltage of 3V.

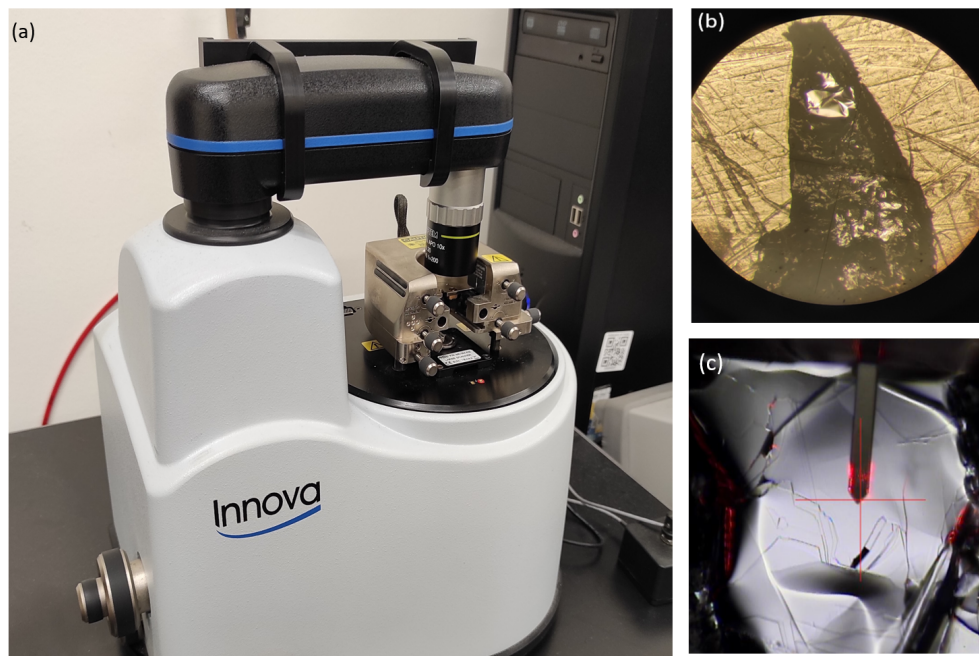


Figure 6.2.5: (a) Innova AFM; (b) a magnification of the metallic sample holder, containing samples attached using a specific electrically-conducting adhesive tape; (c) standard platinum-iridium-covered silicon tip approaching to the sample.

6.3 Results and discussion

All the following characterizations have been performed on samples either pristine or intercalated at zero (nominal) release time.

6.3.1 Raman spectroscopy

The trigonal prismatic phase of MoS₂ (2H-MoS₂) is known to undergo structural phase transitions [155]. These can occur as a result of intercalation by different ionic species. For example, it was proven that Li-ion intercalation in 2H-MoS₂ leads to the formation of the metallic 1T phase and the charge-density-wave transition due to the Peierls instability in Li-intercalated 2H-phase [154, 183]. This can also be achieved by increasing the electron-doping level. MoS₂ actually undergoes a succession of semiconducting, metallic, superconducting, and charge density wave regimes [132]. Therefore, based on this peculiarity of the MoS₂, we assessed the structural phase of both the pristine and the intercalated crystals via Raman spectroscopy. Indeed, as can be deduced from the previous section 6.1.1, Raman spectroscopy turns out to be a powerful approach for investigating morphology variation and crystallographic phase transition behaviour in 2D materials due to its sensitivity to lattice symmetry [121].

Employing the instruments and parameters discussed in the section 6.1.3, we acquired the Raman spectra of a MoS₂ crystal before and after undergoing the ion intercalation process. Figure 6.3.1 reports a comparison between these two spectra.

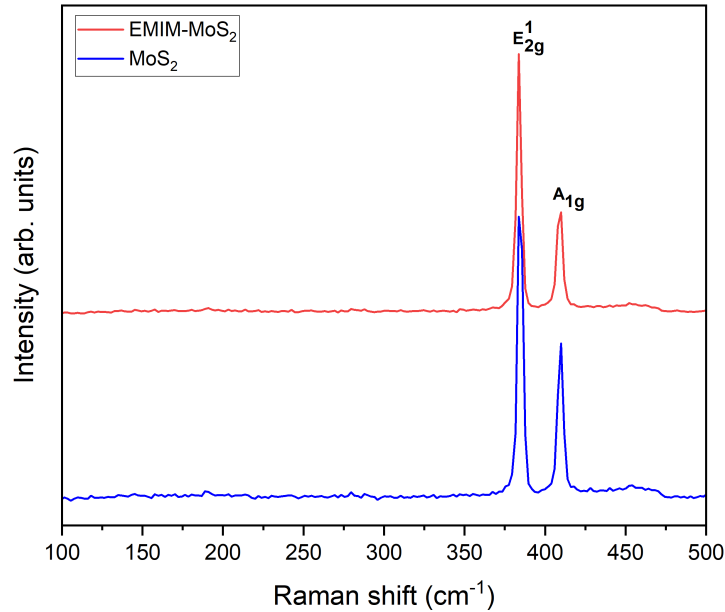


Figure 6.3.1: Raman spectra of MoS₂ (solid blue line) and intercalated-MoS₂ (solid red line) crystals.

By referring to the Figure 6.3.1 obtained and comparing it with the spectra found in the literature [183, 121, 125], one can see that the spectrum of the MoS₂ pristine crystal (solid blue line) presents two Raman peaks typical of the 2H-MoS₂ crystal structure. These originate from the active modes E_{2g}¹ and A_{1g}, at ~384 cm⁻¹ and ~409cm⁻¹, which correspond to in-plane and out-of-plane vibrations of Mo and S atoms, respectively [184, 127].

Analysing the Raman spectrum of MoS₂ (solid red line) after performing the electric-field-driven ion intercalation, one can notice that the same two peaks of the pristine sample are still present. This means that our intercalated-MoS₂ sample retains its original crystal structure, i.e. the 2H polytype. Differently from intercalation with Li⁺, no transition to the 1T/T' metal phase occurs. Indeed, no localised peaks arise around 158, 218 and 334 cm⁻¹ [183, 125].

It is worth noting that the E_{2g}¹ mode remains essentially inert in the two samples. At the same time, Raman shifts close to 409 cm⁻¹ (A_{1g} modes) for pristine and intercalated MoS₂ were obtained after fitting with the Lorentzian function, a standard tool used during the Raman analysis [125, 185], as shown in Figure 6.3.2. Here, it is possible to notice that the A_{1g} mode of the intercalated-MoS₂ sample undergoes a slight redshift, namely a light shift toward a larger wavelength, with a corresponding decrease in frequency, approximately of the order of 0.3 cm⁻¹.

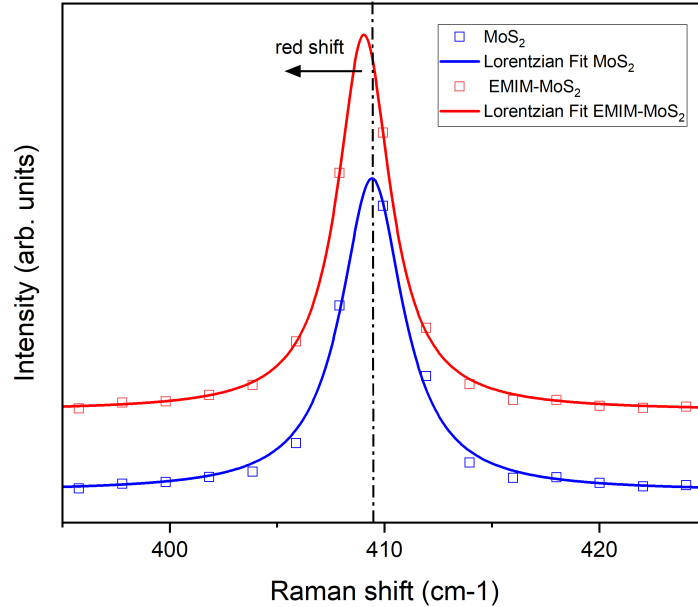


Figure 6.3.2: Lorentzian fit of the A_{1g} mode for both pristine and intercalated MoS₂ crystal.

These behaviours are coherent to gate-induced electron doping as it emerges

from the comparison with the literature [185, 186, 187]. Nevertheless, a quantitative comparison is not allowed because of the different thicknesses of the samples.

6.3.2 Fourier-transform infrared (FT-IR) spectroscopy

To study the detail of ions intercalation in the MoS_2 , we proceeded to perform FT-IR measurements on the EMIM- BF_4 ionic liquid and the MoS_2 sample before and after the intercalation.

Figure 6.3.3 contains a comparison between the IR spectra acquired in the mid-IR frequency ranges during the measurements. As one can see, the spectrum of the pristine MoS_2 crystal (solid blue line) appears essentially featureless. This is coherent with what is reported in literature [188]: indeed, the sharp infrared peaks typical of the 2H phase emerge at wavenumbers around 384 cm^{-1} .

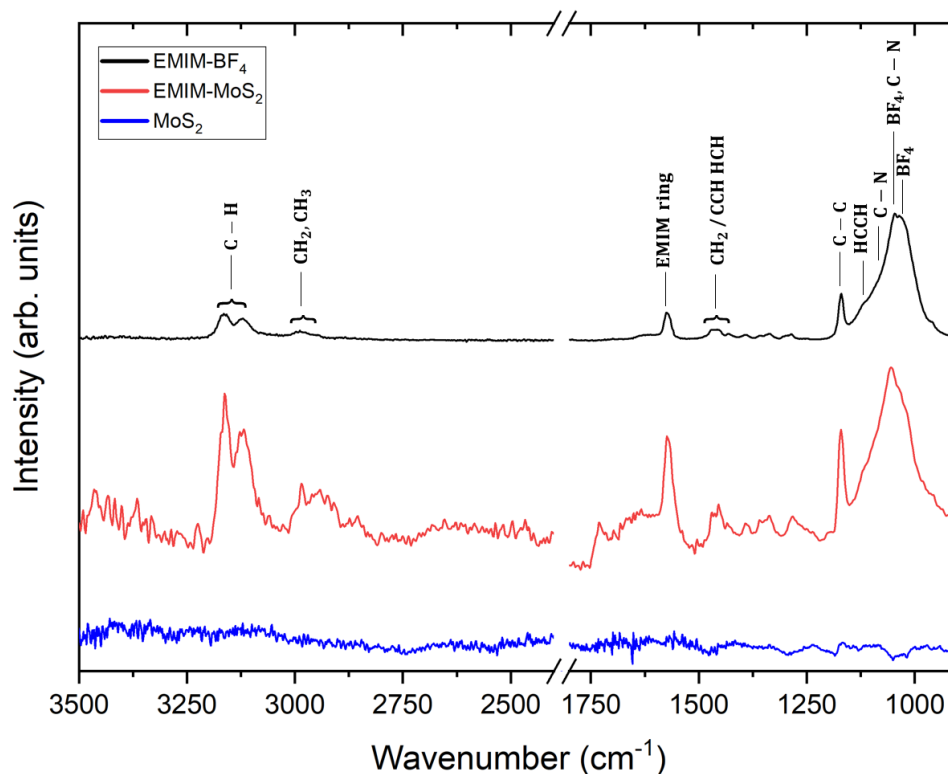


Figure 6.3.3: FT-IR absorption spectra acquired in ATR mode between 3500 and 900 cm^{-1} . The peaks of the EMIM- BF_4 spectrum are labelled.

In an IR spectrum, one can recognize two different regions: one ranging from 4000 cm^{-1} to approximately 1500 cm^{-1} and the other from around 1500 to 600 cm^{-1} . The first allows us to detect the presence of functional groups, while the latter is known as the "fingerprint" region. In particular, the fingerprint peaks are signals proper, typical and characteristic of a specific molecule. So, the fingerprint

region of a given compound is unique and, therefore, can be used to distinguish between compounds. On the contrary, the characteristic peaks of functional groups fall at the same frequencies, regardless of the structure of the molecule in which the group itself is present [189].

By observing the spectrum of the intercalated-MoS₂ sample (solid red line), different bands can be distinguished. These are typical of organic compounds. As reported in Figure 6.3.3, they fall in the single bond region, more precisely in the C–H stretching region (between 3200 and 2800 cm⁻¹) and in the fingerprint region (between 1800 and 900 cm⁻¹, in this case). As clearly visible, the spectrum of the EMIM-BF₄ ionic liquid (solid black line) also presents the same bands. This was measured by mixing the ionic liquid with potassium bromide, which is widely used as a carrier for the sample in the IR spectrum and is optically transparent within the frame of the mid-IR region.

So, according to the literature [190, 191, 192], in the functional groups region, we identify the following structures:

- between 3200 and 3050 cm⁻¹ to the C–H stretching modes. The presence of absorption in this region confirms the existence of unsaturated C atoms in the EMIM ring;
- the narrow band between 3000 and 2850 cm⁻¹ shows the presence of aliphatic compounds. According to the structural formula of the ionic liquid, we are referring to the CH₃ group bonded to the EMIM ring, the CH₃ terminal group of the ethyl chain and the CH₂ group;

In the fingerprint region, we assign:

- the peak around 1572 cm⁻¹ to the EMIM-ring breathing, i.e. all bands stretch and contract in phase;
- the band around 1450 cm⁻¹ to the (CH₂)/CCH HCH bending modes;
- the peak around 1170 cm⁻¹ to the C–C aliphatic stretching modes.

In contrast, the wide range on the rightmost (between 1150 and 900 cm⁻¹), contains at least four peaks resulting both from the cation and the BF₄ anion. We attribute these peaks to the following structures:

- the peak around 1116 cm⁻¹ to ring HCCH symmetric bending;
- the peak around 1085 cm⁻¹ to C–N stretching;
- the peak around 1050 cm⁻¹ to a combination of BF₄ asymmetric stretching and C–N symmetric stretching;
- the peak around 1021 cm⁻¹ to BF₄ asymmetric stretching, which represents the only peak that can be exclusively associated with the presence of the BF₄ anion.

In conclusion, comparing the spectra, we observe that all the primary absorption bands of the EMIM-BF₄ ionic liquid can also be seen in the infrared spectra of the intercalated MoS₂ sample. Consequently, both the EMIM cation and the BF₄ anion are effectively intercalated in the MoS₂ lattice. Although, according to the acquired data, the relative intensity of the EMIM related bands with respect to that of the BF₄-related ones is significantly higher in the intercalated MoS₂ sample than in the ionic liquid. We therefore computed the peak-area of BF₄-stretching mode (1021 cm⁻¹) and the peak-area of the EMIM-breathing mode (1572 cm⁻¹) using the Origin software, both in the EMIM-BF₄ ionic liquid and in the intercalated MoS₂ sample. Then, the peak-area ratio A_{BF_4}/A_{EMIM} was evaluated in both cases, obtaining an about 10-times larger result for the EMIM-BF₄ ionic liquid. The ionic liquid has a one-to-one stoichiometry in terms of anions and cations. Thus, in the case of intercalated MoS₂, we estimate that there is one anion of BF₄ is intercalated for every 10 cations of intercalated EMIM. Finally, since we have a larger quantity of cations, it is possible to confirm that our sample has undergone net electron doping.

6.3.3 Nano-Infrared Microscopy

To investigate the spatial distribution of the intercalants we employed the infrared nanospectroscopy technique.

In Figure 6.3.4a we report a $20 \times 20 \mu\text{m}^2$ AFM topography map of a representative freshly-cleaved surface of an intercalated MoS_2 crystal. It presents a corrugate surface with root mean square roughness $S_q \approx 15 \text{ nm}$, computed from 2^{nd} central moment of data values via Gwyddion, suggesting the presence of a non-flat surface [193]. However, atomically-flat terraces, typical of the pristine crystal, are still visible.

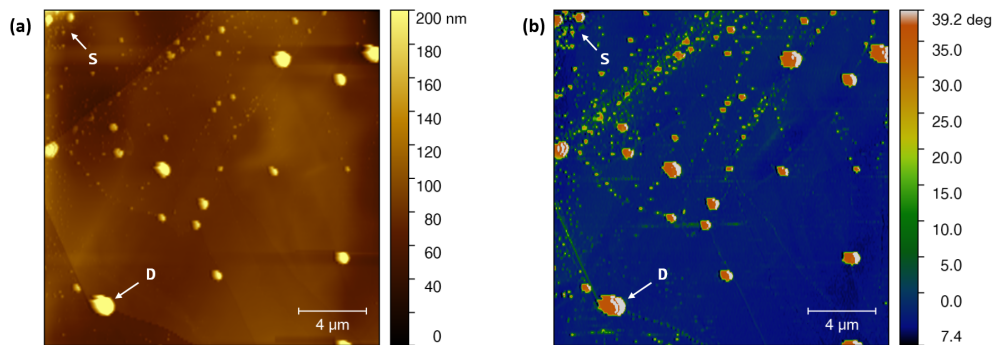


Figure 6.3.4: Infrared nanospectroscopy of intercalated MoS_2 . (a) AFM topography map. (b) Phase image of the same area of panel (a). Adapted from [118].

Moreover, we can observe much taller ellipsoidal yellow "droplets" in Figure 6.3.4a of around 200 nm in diameter randomly scattered on top of the surface. These exhibit a strong contrast in the tapping phase image, shown in Figure 6.3.4b, indicating a net difference in terms of mechanical properties from those of the MoS_2 background.

Hence, as displayed in Figure 6.3.5, we collected IR absorption spectra in the spectral range between 950 to 1800 cm^{-1} both on one of these "droplets" (point D) and on the exposed surface (point S).

In accordance with the FT-IR absorption spectra described in paragraph 6.3.2, we recognized that both spectra highlight the peaks, specific of the EMIM cation, at about 1572 cm^{-1} , 1450 cm^{-1} and 1170 cm^{-1} , as well as the broad band between 1150 and 900 cm^{-1} , also including the BF_4 -related peak at 1021 cm^{-1} . Focusing the spectrum acquired on the exposed MoS_2 surface (solid red line, point S), the BF_4 -related band is significantly less intense with respect to the EMIM-related peaks. Moreover, comparing the BF_4 -related band with that shown in Figure 6.3.3, we can observe that the spectral weight of the BF_4 -stretching peak at 1021 cm^{-1} is strongly suppressed. On the contrary, in the spectrum acquired on the droplet (solid blue line, point D) this latter band is much more pronounced

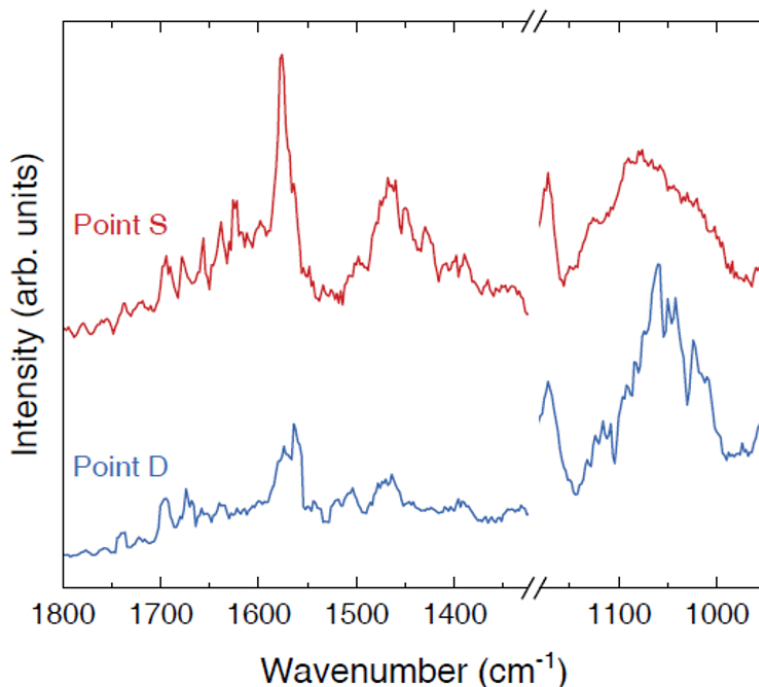


Figure 6.3.5: Infrared nanospectroscopy of intercalated MoS_2 . Nano-IR absorption spectra acquired in correspondence of a droplet (solid blue line, point D) and of the MoS_2 exposed surface (solid red line, point S). Adapted from [118].

than the EMIM-related peaks, in accordance with the pure IL FT-IR spectrum shown in Figure 6.3.3 (solid black line). Together with the phase contrast, these findings imply that the IL residues built in the MoS_2 layers and exposed to the surface after cleaving are the primary source of the BF_4 anions seen in the FT-IR and are responsible for the presence of the observed droplets.

In order to study the spatial distribution of the intercalated EMIM cations, as shown in Figure 6.3.6, an IR absorption map corresponding to the EMIM-breathing mode at 1572 cm^{-1} was acquired. The entire surface exhibits a finite IR absorption at this wavenumber, as depicted in Figure 6.3.6. More in detail, in the regions where IL residues are present (dark red shade "droplets"), the IR absorption decreases significantly.

Nonetheless, a long-range modulation in the IR absorption can be identified over a length scale of $10\mu\text{m}$, indicating that EMIM intercalation in the MoS_2 lattice is inhomogeneous and creates local minima and maxima over a corresponding length scale.

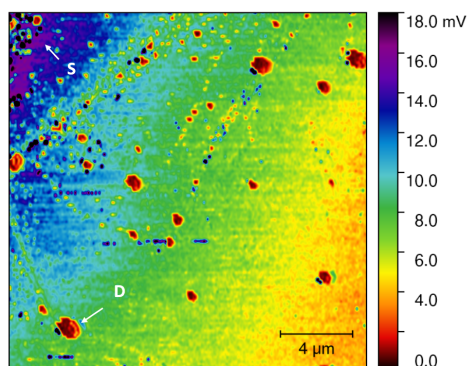


Figure 6.3.6: IR absorption map of the same area acquired in correspondence of the EMIM-breathing mode at $\sim 1572 \text{ cm}^{-1}$. Adapted from [118].

6.3.4 Kelvin-Probe Force Microscopy

At this level, we can certainly talk of EMIM intercalation. So, in order to get more information about its effect on the electronic structure of MoS_2 , we performed Kelvin-probe force microscopy both on a pristine MoS_2 crystal and on the same intercalated crystal analyzed by means of nano-IR.

Starting from the AFM topography map of the pristine MoS_2 in Figure 6.3.7A, we can observe a flat topography with $S_q \approx 1.5 \text{ nm}$, typical of the cleaved surface of a layered material [193]. Moreover, atomic steps and terraces can be distinguished. The correspondent the surface potential distribution is instead featureless and practically homogeneous across the whole area, as shown in Figure 6.3.7b.

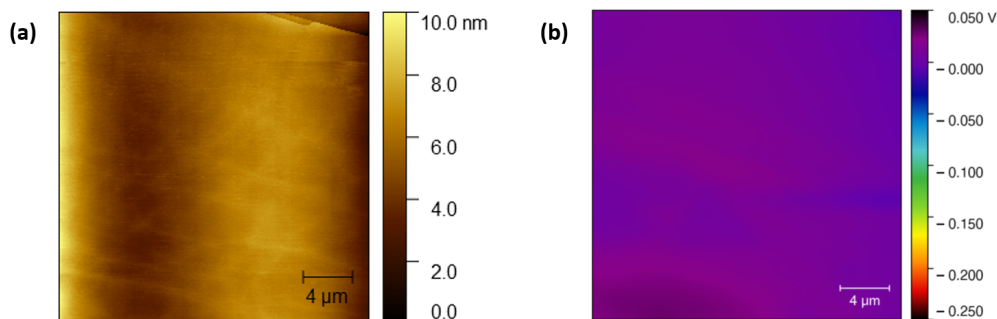


Figure 6.3.7: Kelvin-probe force microscopy of pristine MoS_2 sample. (a) AFM topography map and (b) Surface potential map of pristine MoS_2 . Adapted from [118].

On the contrary, as presented in Figure 6.3.8, the topography map of intercalated MoS_2 again presents a much larger background corrugation, again with $S_q \approx 15 \text{ nm}$, and the localized features associated with IL contaminants. However, in

this instance, the surface potential of intercalated MoS₂ (panel b) is not homogeneous and features fluctuations over the same length scale of approximately 10 μm that typifies the modulations detected through nanoIR in the EMIM content.

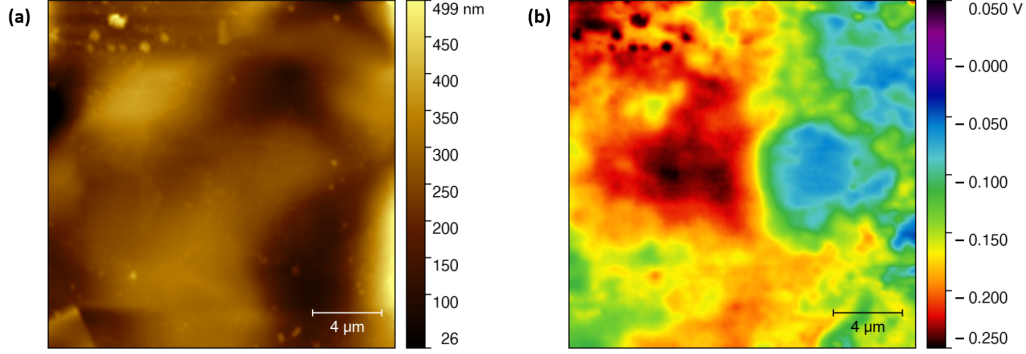


Figure 6.3.8: Kelvin-probe force microscopy of EMIM-MoS₂ sample. (a) AFM topography map and (b) Surface potential map of intercalated MoS₂. Adapted from [118].

The direct comparison of the histograms of the two pictures given in Figure 6.3.9 clearly shows that the surface potential of intercalated MoS₂ is moved to lower values in contrast to that of pure MoS₂ across the whole area.

This surface potential reduction is ascribed as a direct proof of electron doping due to the insertion of the EMIM cations in the MoS₂ crystal lattice, meaning that in the intercalated MoS₂, the Fermi level has been shifted upwards in energy and closer to the vacuum level.

The Fermi energy shift ΔE_F between the pristine and the EMIM-intercalated MoS₂ is analytically given by the difference of the average values of surface potentials ($\langle S.P. \rangle$) multiplied by the elementary charge (e), i.e.

$$\Delta E_F = -e(\langle S.P. \rangle_{intercalated} - \langle S.P. \rangle_{pristine}) \quad (6.2)$$

Using the value extracted from the surface potential histogram in Figure 6.3.9, we know that $\langle S.P. \rangle_{pristine} = +12$ mV and $\langle S.P. \rangle_{intercalated} = -163$ mV. Then, we get $\Delta E_F = +175$ meV. Moreover, as previously discussed in Section 5.2, thanks to the presence of S vacancies in the crystal, the pristine MoS₂ Fermi level is located at the bottom of the CB [134]. Consequently, we can determine the average density of electrons n_e doped into the CB of MoS₂, assuming a parabolic three-dimensional dispersion of the density of states of bulk MoS₂:

$$n_e = \frac{\nu_s \nu_v}{6\pi^2} \left(\frac{2m^*}{\hbar^2} \Delta E_F \right)^{3/2} \quad (6.3)$$

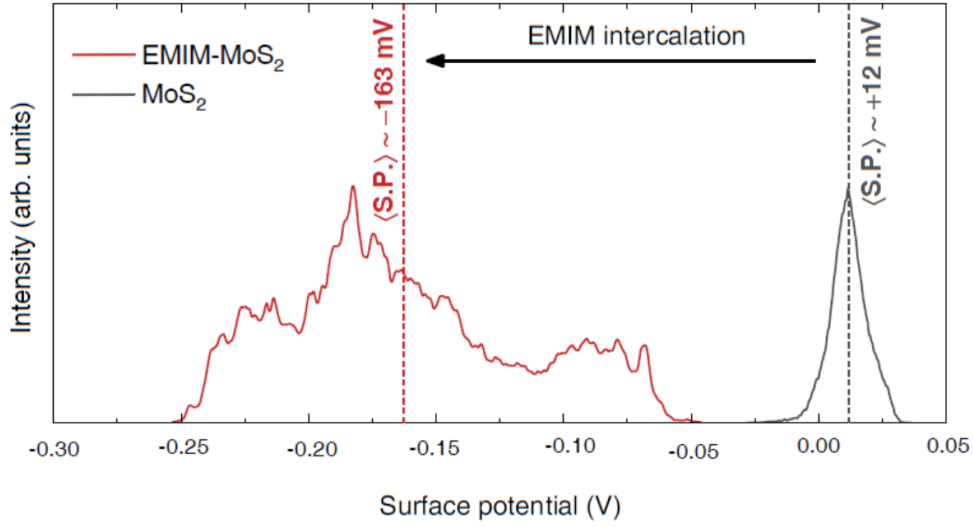


Figure 6.3.9: Kelvin-probe force microscopy of pristine and EMIM-MoS₂ sample. Surface potential histograms highlighting the shift (leftward solid black arrow) in the Fermi energy induced by the intercalation of EMIM ions. Adapted from [118].

where, according to the literature [194, 195] the spin degeneracy is $\nu_s = 2$, the valley degeneracy is $\nu_v = 6$ and the effective mass is $m^* = 0.6m_e$. After the calculations, we obtain $n_e \sim 10^{20} \text{ cm}^{-3}$. A nominal stoichiometry of EMIM_{0.05}MoS₂, which would correspond to about one EMIM cation every 20 MoS₂ formula units, could be obtained if every intercalated EMIM cation donated one electron to the MoS₂ CB.

Considering that our doping distribution is widely inhomogeneous, a broad range of local electron doping levels are present in the EMIM-MoS₂. These can vary from low ones to others that are much higher than the average doping content n_e calculated above. Consequently, if a range of doping wide enough to induce superconductivity were present, at least a volume fraction should fall in that range. Even if this fraction were not sufficient to ensure superconducting percolation, a reduction in the resistivity should be observed. The fact that this does not happen suggests that the superconducting phase either does not develop at all or, if it does, has a lower T_c than those we reached during the experimental phase, i.e. smaller than 2.8 K.

Overall, the information collected in Chapter 5 and Chapter 6 suggests that CDW order competes with superconductivity in MoS₂. Consequently, the superconductive phase appears with higher T_c only when CDW is suppressed or when the onset T of CDW is lower.

The results obtained by doping MoS₂ with Li and K ions highlight the critical

role of the ionic medium in electrochemically gated devices. Therefore, the absence of SC in EMIM-MoS₂ could also be associated with the dimensions of the organic ions. In particular, the large organic ions deriving from the electrolyte could significantly increase the distance between the layers of the material, electronically decoupling them. Such decoupling was already confirmed in the case of SnSe₂, a TMD material intercalated through organic molecules, where the authors registered an increase in the superconducting T_c [118, 196, 197].

In our case, the presence of disorder could have suppressed the SC, or the SC transition might occur at temperatures below 2 K, out of our range of investigation. Therefore, low-temperature structure-sensitive techniques, such as Raman spectroscopy, X-ray diffraction and scanning tunnelling microscopy, would be useful to confirm the presence of CDW ordering in the system, as well as to track its evolution as a function of temperature and doping.

Christof Renner’s group at Geneva University attempted a first cryogenic scanning tunnelling microscope (STM) measurements on our representative EMIM-MoS₂ samples [198].

Up to now, the experiments have not provided encouraging results in the sense that no CDW was detected. In particular, from Raman experiments, they saw the usual MoS₂ peaks at room and low temperature (20-40 K estimated from fitting the spectra). No new peaks were detected, as we can deduce from the spectra in Figure 6.3.10.

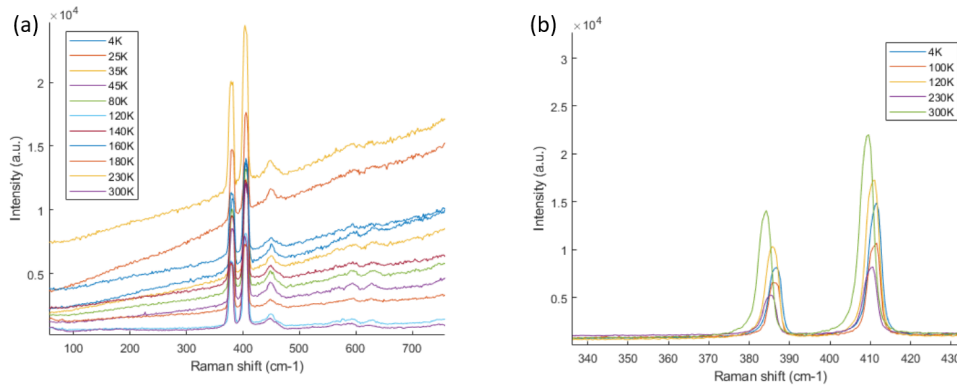


Figure 6.3.10: (a) Raman spectra at room and low temperatures; (b) enlargement of the Raman shift between 340 and 430 cm⁻¹. Adapted from [198].

Regarding the STM measurements, they cleaved the sample in ultra high vacuum and tried five times to approach the sample at 4.8 K, but the tip always crashed due to hanging flakes on the surface, which made its positioning harder. Thus, the tip did not find the setpoint current and kept going forward, digging inside the sample. Most of the places where the tip crashed were well visible on the crystal under an optical microscope, as highlighted by the red circles in Figure 6.3.11.

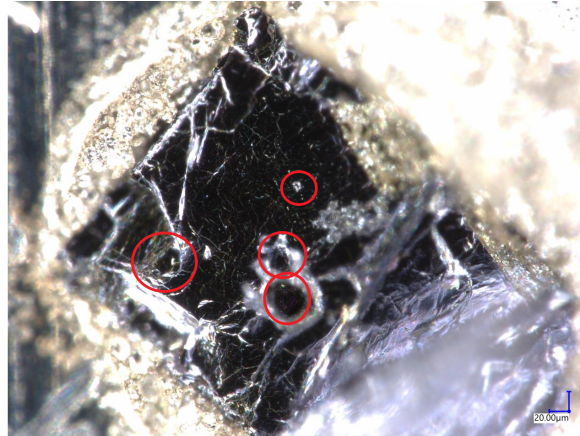


Figure 6.3.11: Red circles indicate the crash points of the tip on the sample surface. Adapted from [198].

When the tip found the setpoint current, it was not in tunnelling conditions. Indeed, the tip was only weakly touching the surface, as we can observe from the nearly linear current- z distance curves, as shown in Figure 6.3.12a.

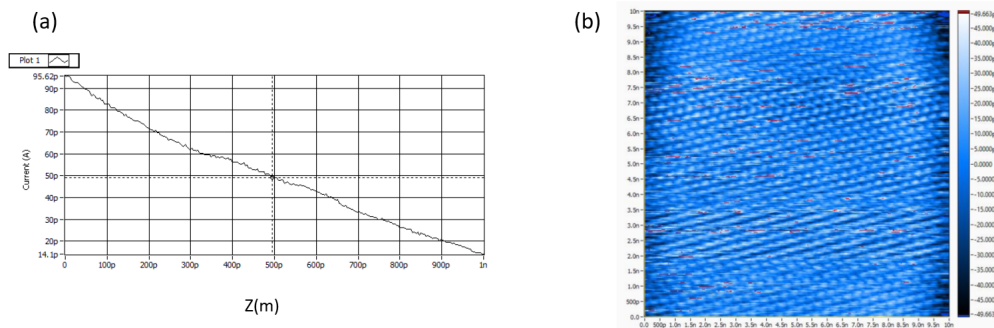


Figure 6.3.12: (a) Current- z distance curve (b) Topography map obtained with a tip gently touching the surface. Adapted from [198].

Even in these conditions, we can obtain images Figure 6.3.12b that show atomic-scale modulations (but, for example, no defects) and signs of dragging at the end/beginning of the scan lines. Most likely, the tip was dragging around the topmost layer. In this condition, we are not able to make any conclusion about the existence of a CDW. Probably, this is due to inhomogeneous doping. Indeed, when the tip approaches regions where the sample is not conductive enough for STM at low temperatures, the measurement does not give any appreciable result. Therefore, further investigations are required.

Chapter 7

Conclusions and Future Perspectives

The original purpose of this thesis project was focused on the search for superconducting states in Pd, Pd_{0.6}Cu_{0.4} alloy and MoS₂ via protonation, i.e. direct hydrogen intercalation, by means the ionic-gating method under optimized gating conditions. Specifically, an ionic gate was exploited to intercalate hydrogen and/or hydrogen-rich organic ions to induce electron doping and/or structure modifications, which are two possible ways to trigger the emergence of superconductivity.

Let us briefly summarise the results obtained for each material and possible further investigations to be performed in the future.

In the case of Pd, resistivity measurements executed after employing the protonation technique with a choline chloride/glycerol eutectic mixture allowed us to confirm the presence of a metallic anomaly around 55 K, as already reported in the literature. However, we can state from our results that the hydrogen concentrations intercalated in our samples are too low to induce an $\alpha \rightarrow \beta$ phase transition for the Pd-H system, probably due to the hydrogen volatility. Consequently, we have not observed any superconducting phase transition down to 2.8 K. Mass spectroscopic analysis techniques will be necessary to obtain accurate quantitative information on the concentration of intercalated hydrogen in our samples. Furthermore, it would be desirable to repeat the intercalation process and measure the transport properties using other gating conditions to verify if the intercalation levels can be increased using higher voltages or another kind of electrolyte. In addition, it is worthwhile to remind that the maximum estimated doping level of H⁺ obtained in our protonation experiments ($x \sim 0.74$) is very close to the level discussed in literature for the onset of a SC transition [72, 79]. This means that our highly protonated Pd samples could be already superconducting, but at a T lower than 2.8 K. Future transport measurements at lower temperatures are thus mandatory in order to check for this possibility. These experiments are now possible in the LaTEST lab at DISAT due to the very recent acquisition of a He-3 cryostat that allows resistivity measurements down to 300 mK.

Pd_{0.6}Cu_{0.4} alloy presents two possible crystalline phases, i.e. a face-centered cubic and a body-centered cubic one. According to recent theoretical predictions, only the body-centered cubic crystalline structure is prone to undergo a superconductive phase transition. So, the selection of the phase is crucial. Referring to the phase diagram of PdCu alloys, it is possible to reach the right crystalline structure via proper annealing. We performed X-ray diffraction analysis to determine the phase of Pd_{0.6}Cu_{0.4} alloy samples after annealing treatments in different temperature and time conditions. We detected both face-centered cubic and body-centered cubic crystalline structures. Preliminary resistivity measurements on both phases resulted unaffected or weakly affected by the hydrogen intercalation deriving from the choline chloride/glycerol eutectic mixture. So, following previous works related to membrane technology, we tried to realize via annealing a properly mixed phase with a higher concentration of face-centered cubic phase, which acts as a hydrogen reservoir for the body-centered cubic phase. In this case, resistivity measurements performed after protonation presented an anomaly in the temperature range between 90 and 120 K. Susceptivity measurements confirmed the presence of this anomaly. Indeed, in this same temperature range, we detected a low-intensity diamagnetic signal. The causes for the emergence of this signal are unknown up to now, but could be associated with the existence of fluxons (and therefore a superconducting state), or with hydrogen ordering into the lattice. Clearly, other investigations are necessary: for example, we suggest performing specific heat measurements to verify if a filamentary superconductive state is present. Also in this case further resistivity measurements at temperatures down to 300 mK will be very interesting in order to check for the presence of a low-T_c superconductivity in protonated Pd_{0.6}Cu_{0.4}.

The first two materials discussed in this experimental work were metals, while the last part of our study focused on MoS₂, a transition-metal dichalcogenide compound with different features and behaviour.

We applied, also in this case, gate-driven ion intercalation using the EMIM-BF₄ ionic liquid. This way, we synthesized organic ion-intercalated MoS₂ crystals. We showed that the lattice retention of dopants is not completely irreversible. Indeed, leaving the material in the electrochemical cell in open-circuit conditions, we have a spontaneous leakage of hydrogen-rich organic ions, tunable in function of the release time, allowing several post-gating measurements. In resistivity measurements, we observed a re-entrant insulator-to-metal transition. This latter develops from the pristine band insulator into an anomalous metallic state and eventually to an incipient second insulating state at the increase of the intercalation level. We showed that the gate-induced metallic state presents evident anomalies in the temperature dependence of the resistivity, manifesting as humps, around 150 K. These could be ascribed to the emergence of charge density wave order, as previously described in the literature for alkali (Li⁺ and K⁺)-intercalated MoS₂. Finally, the combined results of vibrational spectroscopies, Kelvin-probe force microscopy and nano-infrared microscopy allowed us to determine that the doping

occurred thanks to the EMIM ions of the ionic liquid, which act as electron donors and are inhomogeneously distributed across the entire sample volume. However, no sign of superconductivity appeared in our experiments. That could be due to the competition between SC and CDW or the intercalant size. Consequently, other investigations at lower temperatures (Raman spectroscopy, X-ray diffraction and scanning tunnelling microscopy) are required in order to verify if the emergence of anomalies is due to the development of a charge density wave phase. Furthermore due to the established sensitivity of the electric transport properties of MoS₂ to the intercalation with different ionic species, it could be interesting to test the same gating technique employing other electrolyte media to intercalate MoS₂ sample with other organic ions. As in the two materials described above, the possible presence of a low-T_c superconducting phase coexisting with the CDW phase in the metallic state of the EMIM-intercalated MoS₂ could be investigated by resistivity measurements at very low temperatures, now possible in our labs.

Overall, this thesis work illustrated the effects of an alternative and cheap method to intercalate hydrogen or hydrogen-rich ions, a process carried out at room temperature and in ambient atmosphere via the consolidated ionic gating technique. The obtained results, namely the successful intercalation of both hydrogen and hydrogen-rich ions in several different materials, as well as the induction of anomalous metallic phases in all of them, are certainly encouraging, although at a preliminary stage. Further tests are required to demonstrate the repeatability and scalability of the results. We firmly believe this technique can open a wide range of applications, impacting both materials' fundamental research and, hopefully, technological achievements.

Bibliography

- [1] Boeri Lilia et al. “The 2021 room-temperature superconductivity roadmap”. In: *Journal of Physics: Condensed Matter* 34.18 (2022), p. 183002.
- [2] John Bardeen, Leon N Cooper, and John Robert Schrieffer. “Theory of superconductivity”. In: *Physical review* 108.5 (1957), p. 1175.
- [3] Eugene Wigner and HaB Huntington. “On the possibility of a metallic modification of hydrogen”. In: *The Journal of Chemical Physics* 3.12 (1935), pp. 764–770.
- [4] CF Richardson and NW Ashcroft. “High temperature superconductivity in metallic hydrogen: Electron-electron enhancements”. In: *Physical review letters* 78.1 (1997), p. 118.
- [5] TH Lin and KJ Dunn. “High-pressure and low-temperature study of electrical resistance of lithium”. In: *Physical Review B* 33.2 (1986), p. 807.
- [6] Katsuya Shimizu, Hiroto Ishikawa, Daigoroh Takao, Takehiko Yagi, and Kichi Amaya. “Superconductivity in compressed lithium at 20 K”. In: *Nature* 419.6907 (2002), pp. 597–599.
- [7] Jun Nagamatsu, Norimasa Nakagawa, Takahiro Muranaka, Yuji Zenitani, and Jun Akimitsu. “Superconductivity at 39 K in magnesium diboride”. In: *nature* 410.6824 (2001), pp. 63–64.
- [8] NW Ashcroft. “Hydrogen dominant metallic alloys: high temperature superconductors?” In: *Physical Review Letters* 92.18 (2004), p. 187002.
- [9] Hasnain M Syed, CJ Webb, and E MacA Gray. “Hydrogen-modified superconductors: A review”. In: *Progress in Solid State Chemistry* 44.1 (2016), pp. 20–34.
- [10] CB Satterthwaite and IL Toepke. “Superconductivity of hydrides and deuterides of thorium”. In: *Physical Review Letters* 25.11 (1970), p. 741.
- [11] B Stritzker and W Buckel. “Superconductivity in the palladium-hydrogen and the palladium-deuterium systems”. In: *Zeitschrift für Physik A Hadrons and nuclei* 257.1 (1972), pp. 1–8.
- [12] B Stritzker. “High superconducting transition temperatures in the palladium-noble metal-hydrogen system”. In: *Zeitschrift für Physik* 268.2 (1974), pp. 261–264.

-
- [13] AP Drozdov, MI Eremets, IA Troyan, Vadim Ksenofontov, and Sergii I Shylin. “Conventional superconductivity at 203 kelvin at high pressures in the sulfur hydride system”. In: *Nature* 525.7567 (2015), pp. 73–76.
- [14] Maddury Somayazulu, Muhtar Ahart, Ajay K Mishra, Zachary M Geballe, Maria Baldini, Yue Meng, Viktor V Struzhkin, and Russell J Hemley. “Evidence for superconductivity above 260 K in lanthanum superhydride at megabar pressures”. In: *Physical review letters* 122.2 (2019), p. 027001.
- [15] Artur P Durajski and Radosław Szcześniak. “Structural, electronic, vibrational, and superconducting properties of hydrogenated chlorine”. In: *The Journal of chemical physics* 149.7 (2018), p. 074101.
- [16] CM Pépin, G Geneste, A Dewaele, M Mezouar, and P Loubeyre. “Synthesis of FeH₅: A layered structure with atomic hydrogen slabs”. In: *Science* 357.6349 (2017), pp. 382–385.
- [17] Di Zhou et al. “Superconducting praseodymium superhydrides”. In: *Science advances* 6.9 (2020), eaax6849.
- [18] MZ Shi, NZ Wang, B Lei, C Shang, FB Meng, LK Ma, FX Zhang, DZ Kuang, and XH Chen. “Organic-ion-intercalated FeSe-based superconductors”. In: *Physical Review Materials* 2.7 (2018), p. 074801.
- [19] Erik Piatti. “Ionic gating in metallic superconductors: A brief review”. In: *Nano Express* 2.2 (2021), p. 024003.
- [20] I Strzalkowski. *The Physics of Semiconductors with Applications to Optoelectronics Devices*. 1999.
- [21] E Piatti et al. “Control of bulk superconductivity in a BCS superconductor by surface charge doping via electrochemical gating”. In: *Physical Review B* 95.14 (2017), p. 140501.
- [22] Kazunori Ueno, Hidekazu Shimotani, Hongtao Yuan, Jianting Ye, Masashi Kawasaki, and Yoshihiro Iwasa. “Field-induced superconductivity in electric double layer transistors”. In: *Journal of the Physical Society of Japan* 83.3 (2014), p. 032001.
- [23] D Daghero, F Paolucci, A Sola, M Tortello, GA Ummarino, M Agosto, RS Gonnelli, Jijeesh R Nair, and C Gerbaldi. “Large conductance modulation of gold thin films by huge charge injection via electrochemical gating”. In: *Physical review letters* 108.6 (2012), p. 066807.
- [24] W Schmickler. “Electrochemical theory: double layer”. In: (2014).
- [25] K Ueno, S Nakamura, H Shimotani, A Ohtomo, N Kimura, T Nojima, H Aoki, Y Iwasa, and M Kawasaki. “Electric-field-induced superconductivity in an insulator”. In: *Nature materials* 7.11 (2008), pp. 855–858.
- [26] RS Gonnelli et al. “Weak localization in electric-double-layer gated few-layer graphene”. In: *2D Materials* 4.3 (2017), p. 035006.
- [27] Rüdiger Kötz and MJEAC Carlen. “Principles and applications of electrochemical capacitors”. In: *Electrochimica acta* 45.15-16 (2000), pp. 2483–2498.

-
- [28] JT Ye, S Inoue, K Kobayashi, Y Kasahara, HT Yuan, H Shimotani, and Y Iwasa. “Liquid-gated interface superconductivity on an atomically flat film”. In: *Nature materials* 9.2 (2010), pp. 125–128.
- [29] Julia L. Shamshina, Oleksandra Zavgorodnya, and Robin D. Rogers. “Ionic Liquids”. In: *Encyclopedia of Analytical Science (Third Edition)*. Ed. by Paul Worsfold, Colin Poole, Alan Townshend, and Manuel Miró. Third Edition. Oxford: Academic Press, 2019, pp. 218–225.
- [30] Michael Freemantle. *An introduction to ionic liquids*. Royal Society of chemistry, 2010.
- [31] Takuya Fujimoto and Kunio Awaga. “Electric-double-layer field-effect transistors with ionic liquids”. In: *Physical Chemistry Chemical Physics* 15.23 (2013), pp. 8983–9006.
- [32] Chihiro Wakai, Alla Oleinikova, Magnus Ott, and Hermann Weingärtner. “How polar are ionic liquids? Determination of the static dielectric constant of an imidazolium-based ionic liquid by microwave dielectric spectroscopy”. In: *The Journal of Physical Chemistry B* 109.36 (2005), pp. 17028–17030.
- [33] Johannes Hunger, Alexander Stoppa, Simon Schrödle, Glenn Hefter, and Richard Buchner. “Temperature dependence of the dielectric properties and dynamics of ionic liquids”. In: *ChemPhysChem* 10.4 (2009), pp. 723–733.
- [34] K Ueno, S Nakamura, H Shimotani, HT Yuan, N Kimura, T Nojima, H Aoki, Y Iwasa, and M Kawasaki. “Discovery of superconductivity in KTaO₃ by electrostatic carrier doping”. In: *Nature nanotechnology* 6.7 (2011), pp. 408–412.
- [35] Nianpeng Lu et al. “Electric-field control of tri-state phase transformation with a selective dual-ion switch”. In: *Nature* 546.7656 (2017), pp. 124–128.
- [36] Erik Piatti, Qihong Chen, and Jianting Ye. “Strong dopant dependence of electric transport in ion-gated MoS₂”. In: *Applied Physics Letters* 111.1 (2017), p. 013106.
- [37] Zengji Yue. “Ionic gating for ion intercalation”. In: *Nature Reviews Physics* 3.5 (2021), pp. 306–306.
- [38] CH Ahn et al. “Electrostatic modification of novel materials”. In: *Reviews of Modern Physics* 78.4 (2006), p. 1185.
- [39] Yijun Yu et al. “Gate-tunable phase transitions in thin flakes of 1T-TaS₂”. In: *Nature nanotechnology* 10.3 (2015), pp. 270–276.
- [40] Richard A Klemm. “Pristine and intercalated transition metal dichalcogenide superconductors”. In: *Physica C: Superconductivity and its Applications* 514 (2015), pp. 86–94.
- [41] Yi Cui et al. “Ionic-liquid-gating induced protonation and superconductivity in FeSe, FeSe_{0.93}S_{0.07}, ZrNCl, 1T-TaS₂ and Bi₂Se₃”. In: *Chinese Physics Letters* 36.7 (2019), p. 077401.

-
- [42] Mohsin Rafique, Zhongpei Feng, Zefeng Lin, Xinjian Wei, Menghan Liao, Ding Zhang, Kui Jin, and Qi-Kun Xue. “Ionic liquid gating induced protonation of electron-doped cuprate superconductors”. In: *Nano Letters* 19.11 (2019), pp. 7775–7780.
- [43] Yi Cui et al. “Protonation induced high-Tc phases in iron-based superconductors evidenced by NMR and magnetization measurements”. In: *Science Bulletin* 63.1 (2018), pp. 11–16.
- [44] Yan Meng et al. “Protonation-induced discrete superconducting phases in bulk FeSe single crystals”. In: *Physical Review B* 105.13 (2022), p. 134506.
- [45] Yan Meng, Wei Wei, Xiangzhuo Xing, Xiaolei Yi, Nan Zhou, Yufeng Zhang, Wenhui Liu, Yue Sun, and Zhixiang Shi. “Significant enhancement of critical current density in H⁺-intercalated FeSe single crystal”. In: *Superconductor Science and Technology* (2022).
- [46] MZ Shi et al. “FeSe-based superconductors with a superconducting transition temperature of 50 K”. In: *New Journal of Physics* 20.12 (2018), p. 123007.
- [47] Jinhua Wang, Qing Li, Wei Xie, Guanyu Chen, Xiyu Zhu, and Hai-Hu Wen. “Superconductivity at 44.4 K achieved by intercalating EMIM⁺ into FeSe”. In: *Chinese Physics B* 30.10 (2021), p. 107402.
- [48] Haoxiong Zhang et al. “Enhancement of superconductivity in organic-inorganic hybrid topological materials”. In: *Science Bulletin* 65.3 (2020), pp. 188–193.
- [49] Inc. Ted Pella. *SEM Paint, Paste, Aerosol - Conductive Adhesive*. 2022. URL: https://www.tedpella.com/SEMMisc_html/SEMPaint.aspx#16047.
- [50] KEITHLEY. *Making Precision Low Voltage and Low Resistance Measurements*. 2013. URL: https://www.nubicom.co.kr/download/download.jsp?file_name=/keithley/application/AN_Low_Current.pdf.
- [51] INC. TEKTRONIX. *Low Resistance Measurement with a SourceMeter: Do I use Current Reversal, Offset Compensation or Delta Mode measurement methods?* 2022. URL: [https://www.tek.com/en/blog/low-resistance-measurement-source-meter-do-i-use-current-reversal-offset-compensation-or-delta-m#:~:text=What%5C%\\$20is%5C%\\$20the%5C%\\$20Current%5C%\\$20Reversal,shown%5C%\\$20in%5C%\\$20the%5C%\\$20figure%5C%\\$20below.&text=Note%5C%\\$20that%5C%\\$20the%5C%\\$20thermoelectric%5C%\\$20voltage,this%5C%\\$20method%5C%\\$20of%5C%\\$20resistance%5C%\\$20calculation..](https://www.tek.com/en/blog/low-resistance-measurement-source-meter-do-i-use-current-reversal-offset-compensation-or-delta-m#:~:text=What%5C%$20is%5C%$20the%5C%$20Current%5C%$20Reversal,shown%5C%$20in%5C%$20the%5C%$20figure%5C%$20below.&text=Note%5C%$20that%5C%$20the%5C%$20thermoelectric%5C%$20voltage,this%5C%$20method%5C%$20of%5C%$20resistance%5C%$20calculation..)
- [52] Byeong-Sung Yu et al. “Current-reversal operation for a single-parameter electron pump by control of semiconductor-based cryo-switch gate potentials”. In: *AIP Advances* 9.10 (2019), p. 105017.
- [53] I Kuusik, M Berholts, J Kruusma, V Kisand, A Tõnisoo, E Lust, and E Nõmmiste. “Valence electronic structure of [EMIM][BF₄] ionic liquid: photoemission and DFT+D study”. In: *RSC advances* 8.53 (2018), pp. 30298–30304.

-
- [54] Merck KGaA. 2022. URL: <https://www.sigmaaldrich.com/IT/it/product/sial/00768>.
- [55] Benworth B Hansen et al. “Deep eutectic solvents: A review of fundamentals and applications”. In: *Chemical reviews* 121.3 (2020), pp. 1232–1285.
- [56] Electrochemistry group (Department of Pharmacy of the University of Pisa). *DES Glicerolo Colina Cloruro - confidential material*. 2022.
- [57] NATIONAL INSTRUMENTS CORP. 2022. URL: <https://www.ni.com/it-it/shop/labview.html>.
- [58] OriginLab Corporation. *Origin and OriginPro - Introduction*. 2022. URL: <https://www.originlab.com/index.aspx?go=Products/Origin>.
- [59] Inc. The MathWorks. *What Is MATLAB?* 2022. URL: <https://it.mathworks.com/discovery/what-is-matlab.html>.
- [60] Czech Metrology Institute Department of Nanometrology. *Gwyddion – Free SPM (AFM, SNOM/NSOM, STM, MFM, . . .) data analysis software*. 2021. URL: <http://gwyddion.net/>.
- [61] Royal Society of Chemistry. *Palladium*. 2022. URL: <https://www.rsc.org/periodic-table/element/46/palladium>.
- [62] Simon Anthony Steel. *Study of the properties of hydrogen and deuterium in beta phase palladium hydride and deuteride*. University of Salford (United Kingdom), 2018.
- [63] Stephen A Rackley. *Carbon capture and storage*. Butterworth-Heinemann, 2017.
- [64] HL Karlsson, MS Toprak, and B Fadeel. *Handbook on the Toxicology of Metals*. 2015.
- [65] A Elrefaey. “High-temperature brazing in aerospace engineering”. In: *Welding and joining of aerospace materials* (2012), pp. 345–383.
- [66] Thomas Graham. “On the relation of hydrogen to palladium”. In: *Proceedings of the Royal Society of London* 17 (1869), pp. 212–220.
- [67] DA Papaconstantopoulos and BM Klein. “Superconductivity in the palladium-hydrogen system”. In: *Physical Review Letters* 35.2 (1975), p. 110.
- [68] J Theo Klopogge, Concepcion P Ponce, and Tom Loomis. *The Periodic Table: Nature’s Building Blocks: An Introduction to the Naturally Occurring Elements, Their Origins and Their Uses*. Elsevier, 2020.
- [69] FD Manchester, A San-Martin, and JM Pitre. “The H-Pd (hydrogen-palladium) system”. In: *Journal of phase equilibria* 15.1 (1994), pp. 62–83.
- [70] M.V. Goltsova. “Effect of Hydrogen-Phase Cold-Work Hardening on the Palladium-Hydride Dehydrogenation Kinetics”. In: *Metallofiz.* 39.4 (2017), pp. 465–475.
- [71] Donald M Nace and JG Aston. “Palladium Hydride. I. The Thermodynamic Properties of Pd₂H between 273 and 345° K.” In: *Journal of the American Chemical Society* 79.14 (1957), pp. 3619–3623.

-
- [72] T Skośkiewicz and B Baranowski. “Investigation of the Electrical Resistance Anomaly in the Palladium-Hydrogen System”. In: *physica status solidi (b)* 30.1 (1968), K33–K35.
- [73] O Blaschko. “Structural features occurring in PdDx within the 50 K anomaly region”. In: *Journal of the Less Common Metals* 100 (1984), pp. 307–320.
- [74] RE Smallman and AHW Ngan. “Steel transformations”. In: *Modern Physical Metallurgy* (2014), pp. 473–498.
- [75] MH Mueller, J Faber, HE Flotow, and DG Westlake. “Studies on Non-stoichiometric PdHX”. In: *BULLETIN OF THE AMERICAN PHYSICAL SOCIETY*. Vol. 20. 3. AMER INST PHYSICS CIRCULATION FULFILLMENT DIV, 500 SUNNYSIDE BLVD, WOODBURY ... 1975, pp. 421–421.
- [76] HW King and FD Manchester. “A low-temperature X-ray diffraction study of Pd and some Pd-H alloys”. In: *Journal of Physics F: Metal Physics* 8.1 (1978), p. 15.
- [77] Riccarda Caputo and ALI Alavi. “Where do the H atoms reside in PdH x systems?” In: *Molecular Physics* 101.11 (2003), pp. 1781–1787.
- [78] HC Jamieson and FD Manchester. “The magnetic susceptibility of Pd, PdH and PdD between 4 and 300 K”. In: *Journal of Physics F: Metal Physics* 2.2 (1972), p. 323.
- [79] T Skoskiewicz. “Superconductivity in the palladium-hydrogen and palladium-nickel-hydrogen systems”. In: *Volume 11, Number 2 June 16*. De Gruyter, 2022, pp. 825–828.
- [80] KH Bennemann and JW Garland. “Theory for superconductivity in Pd-H and Pd-D systems”. In: *Zeitschrift für Physik A Hadrons and nuclei* 260.5 (1973), pp. 367–374.
- [81] Syed Muhammad Hasnain. “Transient High-Temperature Superconductivity in Palladium Hydride”. PhD thesis. School of Natural Sciences - Griffith University, 2016.
- [82] Leonard Eugene Storm. *The low-temperature specific heat of palladium-hydride and palladium-deuteride*. University of Illinois at Urbana-Champaign, 1980.
- [83] Tatsuya Kawae, Yuji Inagaki, Si Wen, Souhei Hirota, Daiki Itou, and Takashi Kimura. “Superconductivity in Palladium Hydride Systems”. In: *Journal of the Physical Society of Japan* 89.5 (2020), p. 051004. URL: <https://doi.org/10.7566/JPSJ.89.051004>.
- [84] Paolo Tripodi, Daniele Di Gioacchino, Rodolfo Borelli, and Jenny Darja Vinko. “Possibility of high temperature superconducting phases in PdH”. In: *Physica C: Superconductivity* 388 (2003), pp. 571–572.
- [85] Paolo Tripodi, Daniele Di Gioacchino, and Jenny Darja Vinko. “AC electrical resistance measurements of PdHx samples versus composition x”. In: *Journal of alloys and compounds* 486.1-2 (2009), pp. 55–59.

-
- [86] Andrei Lipson, Brent J Heuser, Carlos Castano, George Miley, Boris Lyakhov, and Alexander Mitin. “Transport and magnetic anomalies below 70 K in a hydrogen-cycled Pd foil with a thermally grown oxide”. In: *Physical Review B* 72.21 (2005), p. 212507.
- [87] Andrei G Lipson, Brent J Heuser, Carlos H Castano, and Ayten Celik-Aktas. “Observation of a low-field diamagnetic contribution to the magnetic susceptibility of deformed single crystal PdH_x ($x \approx 4.0 \times 10^{-4}$)”. In: *Physics Letters A* 339.3-5 (2005), pp. 414–423.
- [88] AG Lipson, BJ Heuser, CH Castano, BF Lyakhov, and A Yu Tsivadze. “Magnetic characterization of a hydrogen phase trapped inside deep dislocation cores in a hydrogen-cycled PdH_x ($x \approx 4.5 \times 10^{-4}$) single crystal”. In: *Journal of Experimental and Theoretical Physics* 103.3 (2006), pp. 385–397.
- [89] William F Smith, Javad Hashemi, Alberto Cigada, Silvia Faré, Maria Cristina Tanzi, and Paolo Roncoroni. *Scienza e tecnologia dei materiali*. McGraw-Hill, 2008.
- [90] CERN. *Superconductivity*. 2022. URL: <https://home.cern/science/engineering/superconductivity>.
- [91] R Vocaturo, C Tresca, G Ghiringhelli, and G Profeta. “Prediction of ambient-pressure superconductivity in ternary hydride PdCuH_x”. In: *Journal of Applied Physics* 131.3 (2022), p. 033903.
- [92] Julio J Conde, Marta Maroño, and José María Sánchez-Hervás. “Pd-based membranes for hydrogen separation: review of alloying elements and their influence on membrane properties”. In: *Separation & Purification Reviews* 46.2 (2017), pp. 152–177.
- [93] BH Howard, RP Killmeyer, KS Rothenberger, AV Cugini, BD Morreale, RM Enick, and F Bustamante. “Hydrogen permeance of palladium–copper alloy membranes over a wide range of temperatures and pressures”. In: *Journal of Membrane Science* 241.2 (2004), pp. 207–218.
- [94] Pandian Bothi Raja, Kabilashen Readdyi Munusamy, Veeradasan Perumal, and Mohamad Nasir Mohamad Ibrahim. “Characterization of nanomaterial used in nanobioremediation”. In: *Nano-Bioremediation: Fundamentals and Applications*. Elsevier, 2022, pp. 57–83.
- [95] Thiago Matheus Guimarães Selva, Jéssica Soares Guimarães Selva, and Raphael Bacil Prata. “Sensing Materials: Diamond-Based Materials”. In: (2021).
- [96] University of Cambridge. *Dissemination of IT for the Promotion of Materials Science - X-ray Diffraction Techniques*. 2022. URL: <https://www.doitpoms.ac.uk/tlplib/xray-diffraction/intro.php>.
- [97] Priti P Pednekar, Shilpa C Godiyal, Kisan R Jadhav, and Vilasrao J Kadam. “Mesoporous silica nanoparticles: A promising multifunctional drug delivery system”. In: *Nanostructures for Cancer Therapy*. Elsevier, 2017, pp. 593–621.

-
- [98] KS Nithin, KN Shilpa, Rohini Thimmaiah, BM Jagajeevan Raj, S Sachidananda, and H Siddaramaiah. “Tools and techniques toward characterizing polymer-based smart composites for optical, optoelectronic, and energy-related applications”. In: *Polymer-Based Advanced Functional Composites for Optoelectronic and Energy Applications*. Elsevier, 2021, pp. 91–115.
- [99] xrd.co. *COMPONENT PARTS OF AN X-RAY DIFFRACTOMETER*. 2022. URL: <https://xrd.co/component-parts-x-ray-diffractometer/>.
- [100] Sandra E Dann. *Reactions and characterization of solids*. Vol. 2. Royal Society of Chemistry, 2000.
- [101] Douglas A Skoog, F James Holler, and Stanley R Crouch. *Instrumental analysis*. Vol. 47. Brooks/Cole, Cengage Learning Belmont, 2007.
- [102] NA Al-Mufachi and Robert Steinberger-Wilckens. “X-ray diffraction study on the effects of hydrogen on Pd60Cu40 wt% foil membranes”. In: *Journal of Membrane Science* 545 (2018), pp. 266–274.
- [103] Lixiang Yuan, Andreas Goldbach, and Hengyong Xu. “Real-time monitoring of metal deposition and segregation phenomena during preparation of PdCu membranes”. In: *Journal of Membrane Science* 322.1 (2008), pp. 39–45.
- [104] Andreas Goldbach, Lixiang Yuan, and Hengyong Xu. “Impact of the fcc/bcc phase transition on the homogeneity and behavior of PdCu membranes”. In: *Separation and Purification Technology* 73.1 (2010), pp. 65–70.
- [105] Jiayi Tang, Susumu Yamamoto, Takanori Koitaya, Akitaka Yoshigoe, Takuma Tokunaga, Kozo Mukai, Iwao Matsuda, and Jun Yoshinobu. “Mass transport in the PdCu phase structures during hydrogen adsorption and absorption studied by XPS under hydrogen atmosphere”. In: *Applied Surface Science* 480 (2019), pp. 419–426.
- [106] “Chapter 4 - Experimental Determination of Thermodynamic Quantities and Phase Diagrams”. In: *CALPHAD: Calculation of Phase Diagrams*. Ed. by N. Saunders and A.P. Miodownik. Vol. 1. Pergamon Materials Series. Pergamon, 1998, pp. 61–87.
- [107] D. Daghero. “Notes - Susceptibility and AC susceptibility in metals and superconductors”. In: ()
- [108] RI.SE. *DynoMag manual*. RI.SE, 2017.
- [109] V Gilard, S Trefi, S Balayssac, M-A Delsuc, T Gostan, M Malet-Martino, R Martino, Y Prigent, and Francis Taulelle. “DOSY NMR for drug analysis”. In: *NMR spectroscopy in pharmaceutical analysis*. Elsevier, 2008, pp. 269–289.
- [110] Steven B Chase, Yaw Adu-Gyamfi, and P Fuchs. “Thermoelastic Stress Analysis of Fatigue-Prone Details”. In: (2014).
- [111] SRS STnaford Research Systems. *About Lock-In Amplifiers Application Note*. 2022. URL: https://web.physics.indiana.edu/courses/p451/background_info/SRS_Lock-In_Amplifiers.pdf.

-
- [112] Charles P Poole, Horacio A Farach, and Richard J Creswick. *Superconductivity*. Academic press, 2013.
- [113] Dequan Er and Kamalika Ghatak. “Atomistic modeling by density functional theory of two-dimensional materials”. In: *Synthesis, Modeling, and Characterization of 2D Materials, and Their Heterostructures* (2020), pp. 113–123.
- [114] Chandan Kumar, Santanu Das, and Satyabrata Jit. “Device physics and device integration of two-dimensional heterostructures”. In: *2D Nanoscale Heterostructured Materials*. Elsevier, 2020, pp. 195–214.
- [115] Agnieszka Kuc, Thomas Heine, and Andras Kis. “Electronic properties of transition-metal dichalcogenides”. In: *MRS bulletin* 40.7 (2015), pp. 577–584.
- [116] Eric M Vogel and Joshua A Robinson. “Two-dimensional layered transition-metal dichalcogenides for versatile properties and applications”. In: *MRS Bulletin* 40.7 (2015), pp. 558–563.
- [117] Piatti Erik. “Electrochemical gating for superconductivity engineering in materials towards the 2D limit”. PhD Thesis. Politecnico di Torino, 2017.
- [118] Erik Piatti, Jessica Montagna Bozzone, and Dario Daghero. “Anomalous Metallic Phase in Molybdenum Disulphide Induced via Gate-Driven Organic Ion Intercalation”. In: *Nanomaterials* 12.11 (2022), p. 1842.
- [119] Sajedeh Manzeli, Dmitry Ovchinnikov, Diego Pasquier, Oleg V Yazyev, and Andras Kis. “2D transition metal dichalcogenides”. In: *Nature Reviews Materials* 2.8 (2017), pp. 1–15.
- [120] Rou Jun Toh, Zdeněk Sofer, Jan Luxa, David Sedmidubský, and Martin Pumera. “3R phase of MoS₂ and WS₂ outperforms the corresponding 2H phase for hydrogen evolution”. In: *Chemical Communications* 53.21 (2017), pp. 3054–3057.
- [121] Juan Xia, Jin Wang, Dongliang Chao, Zhen Chen, Zheng Liu, Jer-Lai Kuo, Jiayu Yan, and Ze Xiang Shen. “Phase evolution of lithium intercalation dynamics in 2H-MoS₂”. In: *Nanoscale* 9.22 (2017), pp. 7533–7540.
- [122] Manish Chhowalla, Hyeon Suk Shin, Goki Eda, Lain-Jong Li, Kian Ping Loh, and Hua Zhang. “The chemistry of two-dimensional layered transition metal dichalcogenide nanosheets”. In: *Nature chemistry* 5.4 (2013), pp. 263–275.
- [123] Dong-Kyun Seo and Roald Hoffmann. “Direct and indirect band gap types in one-dimensional conjugated or stacked organic materials”. In: *Theoretical Chemistry Accounts* 102.1 (1999), pp. 23–32.
- [124] Deepika Gupta, Vishnu Chauhan, and Rajesh Kumar. “A comprehensive review on synthesis and applications of molybdenum disulfide (MoS₂) material: Past and recent developments”. In: *Inorganic Chemistry Communications* 121 (2020), p. 108200.

-
- [125] Yinsheng Guo, Dezheng Sun, Bin Ouyang, Archana Raja, Jun Song, Tony F Heinz, and Louis E Brus. “Probing the dynamics of the metallic-to-semiconducting structural phase transformation in MoS₂ crystals”. In: *Nano letters* 15.8 (2015), pp. 5081–5088.
- [126] Andrea Splendiani, Liang Sun, Yuanbo Zhang, Tianshu Li, Jonghwan Kim, Chi-Yung Chim, Giulia Galli, and Feng Wang. “Emerging photoluminescence in monolayer MoS₂”. In: *Nano letters* 10.4 (2010), pp. 1271–1275.
- [127] Erik Piatti, Domenico De Fazio, Dario Daghero, Srinivasa Reddy Tamalam-pudi, Duhee Yoon, Andrea C Ferrari, and Renato S Gonnelli. “Multi-valley superconductivity in ion-gated MoS₂ layers”. In: *Nano letters* 18.8 (2018), pp. 4821–4830.
- [128] Davide Romanin, Thomas Brumme, Dario Daghero, Renato S Gonnelli, and Erik Piatti. “Strong band-filling-dependence of the scattering lifetime in gated MoS₂ nanolayers induced by the opening of intervalley scattering channels”. In: *Journal of Applied Physics* 128.6 (2020), p. 063907.
- [129] Branimir Radisavljevic and Andras Kis. “Mobility engineering and a metal–insulator transition in monolayer MoS₂”. In: *Nature materials* 12.9 (2013), pp. 815–820.
- [130] Johan Biscaras, Zhesheng Chen, Andrea Paradisi, and Abhay Shukla. “Onset of two-dimensional superconductivity in space charge doped few-layer molybdenum disulfide”. In: *Nature communications* 6.1 (2015), pp. 1–8.
- [131] JT Ye, Yj J Zhang, R Akashi, Ms S Bahramy, R Arita, and Y Iwasa. “Superconducting dome in a gate-tuned band insulator”. In: *Science* 338.6111 (2012), pp. 1193–1196.
- [132] M Rösner, S Haas, and TO Wehling. “Phase diagram of electron-doped dichalcogenides”. In: *Physical Review B* 90.24 (2014), p. 245105.
- [133] Mohammed K Bin Subhan, Asif Suleman, Gareth Moore, Peter Phu, Moritz Hoesch, Hidekazu Kurebayashi, Christopher A Howard, and Steven R Schofield. “Charge density waves in electron-doped molybdenum disulfide”. In: *Nano letters* 21.13 (2021), pp. 5516–5521.
- [134] Hao Qiu et al. “Hopping transport through defect-induced localized states in molybdenum disulphide”. In: *Nature communications* 4.1 (2013), pp. 1–6.
- [135] V Singh. “Band gap and resistivity measurements of semiconductor materials for thin films”. In: *Journal of Emerging Technologies and Innovative Research (JETIR)* 4.12 (2017), pp. 1200–1210.
- [136] Lisa M Larrimore. “Low temperature resistivity”. In: *Swarthmore College Computer Society* (2005).
- [137] RM Hill. “Variable-range hopping”. In: *physica status solidi (a)* 34.2 (1976), pp. 601–613.

-
- [138] Subhamoy Ghatak, Atindra Nath Pal, and Arindam Ghosh. “Nature of electronic states in atomically thin MoS₂ field-effect transistors”. In: *ACS nano* 5.10 (2011), pp. 7707–7712.
- [139] Corentin Durand, Xiaoguang Zhang, Jason Fowlkes, Sina Najmaei, Jun Lou, and An-Ping Li. “Defect-mediated transport and electronic irradiation effect in individual domains of CVD-grown monolayer MoS₂”. In: *Journal of Vacuum Science & Technology B, Nanotechnology and Microelectronics: Materials, Processing, Measurement, and Phenomena* 33.2 (2015), 02B110.
- [140] Erik Piatti et al. “Charge transport mechanisms in inkjet-printed thin-film transistors based on two-dimensional materials”. In: *Nature Electronics* 4.12 (2021), pp. 893–905.
- [141] Wei Bao, Zhicheng Su, Changcheng Zheng, Jiqiang Ning, and Shijie Xu. “Carrier localization effects in InGaN/GaN multiple-quantum-wells LED nanowires: luminescence quantum efficiency improvement and “negative” thermal activation energy”. In: *Scientific reports* 6.1 (2016), pp. 1–9.
- [142] Jolene D Splett, Dominic F Vecchia, and Loren F Goodrich. “A comparison of methods for computing the residual resistivity ratio of high-purity niobium”. In: *Journal of research of the National Institute of Standards and Technology* 116.1 (2011), p. 489.
- [143] Patrick Gallagher, Menyong Lee, Trevor A Petach, Sam W Stanwyck, James R Williams, Kenji Watanabe, Takashi Taniguchi, and David Goldhaber-Gordon. “A high-mobility electronic system at an electrolyte-gated oxide surface”. In: *Nature communications* 6.1 (2015), pp. 1–5.
- [144] Yu Saito and Yoshihiro Iwasa. “Ambipolar insulator-to-metal transition in black phosphorus by ionic-liquid gating”. In: *ACS nano* 9.3 (2015), pp. 3192–3198.
- [145] E Piatti, S Galasso, M Tortello, JR Nair, C Gerbaldi, M Bruna, S Borini, D Daghero, and RS Gonnelli. “Carrier mobility and scattering lifetime in electric double-layer gated few-layer graphene”. In: *Applied Surface Science* 395 (2017), pp. 37–41.
- [146] Erik Piatti et al. “Ambipolar suppression of superconductivity by ionic gating in optimally doped BaFe₂(As, P)₂ ultrathin films”. In: *Physical Review Materials* 3.4 (2019), p. 044801.
- [147] Dmitry Ovchinnikov, Fernando Gargiulo, Adrien Allain, Diego José Pasquier, Dumitru Dumcenco, Ching-Hwa Ho, Oleg V Yazyev, and Andras Kis. “Disorder engineering and conductivity dome in ReS₂ with electrolyte gating”. In: *Nature communications* 7.1 (2016), pp. 1–7.
- [148] Jianming Lu, Oleksandr Zheliuk, Qihong Chen, Inge Leermakers, Nigel E Hussey, Uli Zeitler, and Jianting Ye. “Full superconducting dome of strong Ising protection in gated monolayer WS₂”. In: *Proceedings of the National Academy of Sciences* 115.14 (2018), pp. 3551–3556.
- [149] George Grüner. *Density waves in solids*. CRC press, 2018.

-
- [150] Zhongxu Wei et al. “Two superconductor-insulator phase transitions in the spinel oxide $\text{Li}_{1+x}\text{Ti}_2\text{O}_4-\delta$ induced by ionic liquid gating”. In: *Physical Review B* 103.14 (2021), p. L140501.
- [151] George Grüner. “The dynamics of charge-density waves”. In: *Reviews of modern physics* 60.4 (1988), p. 1129.
- [152] AM Gabovich, AI Voitenko, JF Annett, and M Ausloos. “Charge-and spin-density-wave superconductors”. In: *Superconductor Science and Technology* 14.4 (2001), R1.
- [153] Andrey N Enyashin and Gotthard Seifert. “Density-functional study of Li_xMoS_2 intercalates ($0 < x < 1$)”. In: *Computational and Theoretical Chemistry* 999 (2012), pp. 13–20.
- [154] XiaoBo Chen, ZhenLian Chen, and Jun Li. “Critical electronic structures controlling phase transitions induced by lithium ion intercalation in molybdenum disulphide”. In: *Chinese Science Bulletin* 58.14 (2013), pp. 1632–1641.
- [155] Houlong L Zhuang, Michelle D Johannes, Arunima K Singh, and Richard G Hennig. “Doping-controlled phase transitions in single-layer MoS_2 ”. In: *Physical Review B* 96.16 (2017), p. 165305.
- [156] Zi-Yu Cao, Jia-Wei Hu, Alexander F Goncharov, and Xiao-Jia Chen. “Non-trivial metallic state of MoS_2 ”. In: *Physical Review B* 97.21 (2018), p. 214519.
- [157] Renyan Zhang, I-Ling Tsai, James Chapman, Ekaterina Khestanova, John Waters, and Irina V Grigorieva. “Superconductivity in potassium-doped metallic polymorphs of MoS_2 ”. In: *Nano letters* 16.1 (2016), pp. 629–636.
- [158] Andrzej Kudelski. “Analytical applications of Raman spectroscopy”. In: *Talanta* 76.1 (2008), pp. 1–8.
- [159] Konstantin I Hadjiivanov, Dimitar A Panayotov, Mihail Y Mihaylov, Elena Z Ivanova, Kristina K Chakarova, Stanislava M Andonova, and Nikola L Drenchev. “Power of infrared and raman spectroscopies to characterize metal-organic frameworks and investigate their interaction with guest molecules”. In: *Chemical Reviews* 121.3 (2020), pp. 1286–1424.
- [160] University of Cambridge. *Dissemination of IT for the Promotion of Materials Science - Raman Spectroscopy*. 2022. URL: https://www.doitpoms.ac.uk/tlplib/raman/raman_scattering.php.
- [161] Andreas Braeuer. *In situ spectroscopic techniques at high pressure*. Elsevier, 2015.
- [162] Pavan M. V. Raja Andrew R. Barron. *Raman and Surface-Enhanced Raman Spectroscopy*. 2022. URL: https://chem.libretexts.org/Bookshelves/Analytical_Chemistry/Physical_Methods_in_Chemistry_and_Nano_Science_/_Barron_/04/3A_Chemical_Speciation/4.03/3A_Raman_Spectroscopy.

-
- [163] BRUKER. *Guide to Infrared Spectroscopy*. 2022. URL: <https://www.bruker.com/it/products-and-solutions/infrared-and-raman/ft-ir-routine-spectrometer/what-is-ft-ir-spectroscopy.html>.
- [164] Ralph Levinson. *More modern chemical techniques*. Royal Society of Chemistry, 2001.
- [165] Donald L Pavia, Gary M Lampman, George S Kriz, and James A Vyvyan. *Introduction to spectroscopy*. Cengage learning, 2014.
- [166] RENISHAW plc. *Introduction to Raman spectroscopy*. 2016. URL: https://www.ccmr.cornell.edu/wp-content/uploads/sites/2/2016/08/Wire4_Training_Modules_Compilation-Part-2.pdf.
- [167] METTLER TOLEDO. *Attenuated Total Reflectance (ATR)-ATR Sampling Technology for FTIR Applications*. 2022. URL: https://www.mt.com/my/en/home/products/L1_AutochemProducts/ReactIR/attenuated-total-reflectance-atr.html.
- [168] MF Brunella, A Serafini, and MC Tanzi. “Characterization of 2D polymeric biomaterial structures or surfaces”. In: *Characterization of Polymeric Biomaterials*. Elsevier, 2017, pp. 3–19.
- [169] Serap Yesilkir-Baydar, Olga N Oztel, Rabia Cakir-Koc, and Ayse Candayan. “Evaluation techniques”. In: *Nanobiomaterials Science, Development and Evaluation*. Elsevier, 2017, pp. 211–232.
- [170] University of Cambridge. *Dissemination of IT for the Promotion of Materials Science - Atomic Force Microscopy*. 2022. URL: <https://www.doitpoms.ac.uk/tlplib/afm/intro.php>.
- [171] Suprakas Sinha Ray. *4—Techniques for characterizing the structure and properties of polymer nanocomposites*. 2013.
- [172] Alexandre Dazzi and Craig B Prater. “AFM-IR: Technology and applications in nanoscale infrared spectroscopy and chemical imaging”. In: *Chemical reviews* 117.7 (2017), pp. 5146–5173.
- [173] Hang Zhang, Junxiang Huang, Yongwei Wang, Rui Liu, Xiulan Huai, Jingjing Jiang, and Chantelle Anuso. “Atomic force microscopy for two-dimensional materials: A tutorial review”. In: *Optics Communications* 406 (2018), pp. 3–17.
- [174] BRUKER. *NANOSCALE INFRARED SPECTROSCOPY Comparison of AFM-IR and s-SNOM*. 2022. URL: <https://www.bruker.com/en/products-and-solutions/infrared-and-raman/nanoscale-infrared-spectrometers/comparison-of-afm-ir-and-s-snom.html>.
- [175] BRUKER. *NANOSCALE INFRARED SPECTROSCOPY - Tapping AFM-IR - The highest performance nanoscale IR chemical imaging solution*. 2022. URL: <https://www.bruker.com/en/products-and-solutions/infrared-and-raman/nanoscale-infrared-spectrometers/tapping-afm-ir.html>.

-
- [176] Rudiger Paschotta. *Optical Heterodyne Detection*. 2022. URL: https://www.rp-photonics.com/optical_heterodyne_detection.html.
- [177] Mark Chapman. “Heterodyne and homodyne interferometry”. In: *News from Renishaw* (2002).
- [178] Wilhelm Melitz, Jian Shen, Andrew C Kummel, and Sangyeob Lee. “Kelvin probe force microscopy and its application”. In: *Surface science reports* 66.1 (2011), pp. 1–27.
- [179] Nanosurf AG. *Kelvin Probe Force Microscopy (KPFM)*. URL: <https://www.nanosurf.com/images/applications/KPFM/Kelvin-probe-force-microscopy-KPFM.pdf>.
- [180] Li Chunzeng et al. “PeakForce Kelvin Probe Force Microscopy”. In: *Bruker Nano Surfaces www.bruker.com, Application Note* 140 (2013), p. 98.
- [181] Bruker Corporation. *Lift Mode Surface Potential Imaging (AM-KPFM)*. URL: <https://www.nanophys.kth.se/nanolab/afm/icon/bruker-help/Content/Interleave%5C%20Scanning/Interleave%5C%20Scanning.htm>.
- [182] Da Luo, Hao Sun, and Yan Li. “Kelvin probe force microscopy in nanoscience and nanotechnology”. In: *Surface Science Tools for Nanomaterials Characterization*. Springer, 2015, pp. 117–158.
- [183] Damien Voiry, Aditya Mohite, and Manish Chhowalla. “Phase engineering of transition metal dichalcogenides”. In: *Chemical Society Reviews* 44.9 (2015), pp. 2702–2712.
- [184] Changgu Lee, Hugen Yan, Louis E Brus, Tony F Heinz, James Hone, and Sunmin Ryu. “Anomalous lattice vibrations of single-and few-layer MoS₂”. In: *ACS nano* 4.5 (2010), pp. 2695–2700.
- [185] Xin Lu, MIB Utama, Xingzhi Wang, Weigao Xu, Weijie Zhao, Man Hon Samuel Owen, and Qihua Xiong. “Gate-Tunable resonant Raman spectroscopy of bilayer MoS₂”. In: *Small* 13.35 (2017), p. 1701039.
- [186] Biswanath Chakraborty, Achintya Bera, D. V. S. Muthu, Somnath Bhowmick, U. V. Waghmare, and A. K. Sood. “Symmetry-dependent phonon renormalization in monolayer MoS₂ transistor”. In: *Phys. Rev. B* 85 (16 2012), p. 161403.
- [187] Thibault Sohier, Evgeniy Ponomarev, Marco Gibertini, Helmuth Berger, Nicola Marzari, Nicolas Ubrig, and Alberto F Morpurgo. “Enhanced electron-phonon interaction in multivalley materials”. In: *Physical Review X* 9.3 (2019), p. 031019.
- [188] Xin Chen, Nina C Berner, Claudia Backes, Georg S Duesberg, and Aidan R McDonald. “Functionalization of two-dimensional MoS₂: on the reaction between MoS₂ and organic thiols”. In: *Angewandte Chemie* 128.19 (2016), pp. 5897–5902.

-
- [189] Asep Bayu Dani Nandiyanto, Rosi Oktiani, and Risti Ragadhita. “How to read and interpret FTIR spectroscopy of organic material”. In: *Indonesian Journal of Science and Technology* 4.1 (2019), pp. 97–118.
- [190] Norman E Heimer, Rico E Del Sesto, Zhizhong Meng, John S Wilkes, and W Robert Carper. “Vibrational spectra of imidazolium tetrafluoroborate ionic liquids”. In: *Journal of molecular liquids* 124.1-3 (2006), pp. 84–95.
- [191] O Hofft, S Bahr, and V Kemper. “Investigations with infrared spectroscopy on films of the ionic liquid [EMIM] Tf₂N”. In: *Langmuir* 24.20 (2008), pp. 11562–11566.
- [192] Mostefa Boumediene, Boumediene Haddad, Annalisa Paolone, Mokhtar Draï, Didier Villemin, Mustapha Rahmouni, Serge Bresson, and Ouissam Abbas. “Synthesis, thermal stability, vibrational spectra and conformational studies of novel dicationic meta-xylyl linked bis-1-methylimidazolium ionic liquids”. In: *Journal of Molecular Structure* 1186 (2019), pp. 68–79.
- [193] Jorge Quereda, Andres Castellanos-Gomez, Nicolás Agrat, and Gabino Rubio-Bollinger. “Single-layer MoS₂ roughness and sliding friction quenching by interaction with atomically flat substrates”. In: *Applied Physics Letters* 105.5 (2014), p. 053111.
- [194] Zefei Wu et al. “Even–odd layer-dependent magnetotransport of high-mobility Q-valley electrons in transition metal disulfides”. In: *Nature communications* 7.1 (2016), pp. 1–8.
- [195] QH Chen, JM Lu, Lei Liang, Oleksandr Zheliuk, A Ali, Ping Sheng, and JT Ye. “Inducing and Manipulating Heteroelectronic States in a Single MoS₂ Thin Flake”. In: *Physical Review Letters* 119.14 (2017), p. 147002.
- [196] Hanlin Wu, Sheng Li, Michael Susner, Sunah Kwon, Moon Kim, Timothy Haugan, and Bing Lv. “Spacing dependent and cation doping independent superconductivity in intercalated 1T 2D SnSe₂”. In: *2D Materials* 6.4 (2019), p. 045048.
- [197] LK Ma et al. “Quasi-two-dimensional superconductivity in Sn Se₂ via organic ion intercalation”. In: *Physical Review Materials* 4.12 (2020), p. 124803.
- [198] Christoph Renner - University of Geneva Árpád Pásztor Ishita Pushkarna. “Confidential report-Protonated MoS₂ from Torino”. In: (2021).